“ Any fool can know. The point is to understand.”

~

Albert Einstein

University of Alberta

An Improved 3D *In Vitro* Model for High-throughput Electrode Biocompatibility Testing

by

Andrea Faye Jeffery

A thesis submitted to the Faculty of Graduate Studies and Research
in partial fulfillment of the requirements for the degree of

Master of Science
In
Materials Engineering

Department of Chemical and Materials Engineering

Spring 2014
Edmonton, Alberta

Dedication

This thesis is dedicated to my parents, Gary and Sharon Jeffery, for their continued support, motivation and love, which have encouraged me to follow my heart and take on new challenges.

Abstract

Recent technological advancements in the field of neural recording and decoding have changed the landscape of neural prostheses. However, a lack of biocompatible electrodes for long-term neural recording resulting in loss of electrode functionality is currently a major limiting factor for clinical implementation of advancing neural interfacing technology. Chronic activation of microglia and astrocytes as well as increasing cell density at the electrode are considered to be the primary reason for decreasing electrode functionality over time. Glial scarring models to date (primarily *in vivo*) have provided an excellent documentation of the temporal response of microglia and astrocytes upon electrode insertion, but do not satisfactorily address the degree to which various electrode parameters influence glial scarring. Herein a novel 3D glial scarring model based on hyaluronic acid is proposed. This model is shown to support mixed glial cells, mimic the mechanical properties of the central nervous system and model the acute inflammatory response over 21 days.

Acknowledgements

I would like to thank my supervisors, Dr. Anastasia Elias and Dr. Kathryn Todd, for their support, encouragement and guidance throughout my degree. Attempting an interdisciplinary project that extends across campus and takes place in many labs can be a daunting task; your co-supervision not only made my project possible, but made it successful.

I would also like to thank my lab mates Dr. Matthew Churchward, Dr. Kam Dhami, Ben Nearingberg, Anthony Zerberoff, Erika Mikkalson, Sarah Kenaway, Sam Joshua Baskar, Cheng Cheng, Xi Huang, Chan Chan, Preetam Anbukarasu, Sangita Sridar and Theodore Ng who have given me countless pieces of advice, help and training every hour of every day. In addition to my lab mates, numerous other grad students, colleagues, friends and family supported me along my journey. Thank you.

Finally I would like to acknowledge the funding I received from Alberta Innovates Health Solutions, Alberta Innovates Technology Futures and the Queen Elizabeth II Graduate Scholarship, that contributed significantly to the progress of my project and the dissemination of knowledge I acquired at conferences and meetings throughout my degree.

A special acknowledgement is made to Russell Dodd and Matthew Churchward who, in addition to my supervisors, contributed significantly to the editing of this document.

Table of Contents

List of Tables

List of Figures

Abbreviations

2D	two-dimensional
3D	three-dimensional
ANOVA	analysis of variance
APTS	(3-Aminopropyl)triethoxysilane
ATP	adenosine triphosphate
BBB	blood brain barrier
CD	cell density
CNS	central nervous system
CNT	carbon nanotubes
CSPGs	chondroitin sulfate proteoglycans
DAPI	4',6-diamidino-2-phenylindole, dihydrochloride
DBS	deep brain stimulation
ddH2O	distilled water
DMEM	Dulbecco's modified Eagle's medium
dsDNA	double stranded deoxyribonucleic acid
ECM	extracellular matrix
EEG	electroenchephalography
EtOH	ethanol
EY	eosin Y
FBS	fetal bovine serum
GFAP	glial fibrillary acidic protein
HA	hyaluronic acid
HAMA	methacrylated hyaluronic acid
HBSS	Hank's Balanced Saline Solution
LED	light emitting diode
MA	methacrylic anhydride
NHS	normal horse serum
NMR	nuclear magnetic resonance

NVP	1-vinyl-2-pyrrolidinone
PBS	phosphate buffered solution
PDMS	polydimethylsioxane
PEDOT	poly(3,4-ethylenedioxythiophene)
PLL	poly-L-lysine
PNS	peripheral nervous system
PS	penicillin-streptomycin
q	equilibrium swelling ratio
q'	equilibrium swelling percent
SEM	scanning electron microscopy
TEA	triethanolamine
TPM	3-(Trimethoxysily) propyl methacrylate
UEA	Utah electrode array
UV	ultra violet
v	volume
w	weight
wt%	weight percent (w/v)

Chemicals and Reagents

Chemicals and reagents used for the experiments described in this thesis are listed below with their abbreviations and source. Those chemicals and reagents without sources were prepared in house.

	Chemical/Reagent	Source	Product #
NVP	**1-vinyl-2-pyrrolidinone**	Sigma	V3409-5G
TPM	**3-(Trimethoxysily) propyl methacrylate**	Sigma	M6514-25ML
DAPI	**4',6-diamidino-2-phenylindole, dihydrochloride**	Vector Labs	H-1200
	acetone	Fisher	A949
	Alexa Fluor 488 donkey anti-rabbit	Molecular Probes	A21206
	Alexa Fluor 647 donkey anti-mouse	Molecular Probes	A31571
	anti-mouse GFAP	Sigma	G 3893
	anti-rabbit Iba1	Wako	019-19741
	Brain Buffer	-	-
	Cy-2 donkey anti-mouse	Jackson	715-226-151
ddH2O	**double distilled water**	-	-
DMEM	**Dulbecco's modified Eagle's medium**	Hyclone	SH30272
EY	**eosin Y**	Sigma	119830
EtOH	**ethanol**	Commercial Alcohols	E112
FBS	**fetal bovine serum**	Gibco	16000-036
	Fluoromount G	Southern Biotech	0100-01
	Formalin (1o%)	Fisher	SF100
HBSS	**Hank's Balanced Salt Solution**	Thermo Scientific	14170-112
HA	**hyaluronic acid**	Sigma	53737-10G
MA	**methacrylic anhydride**	Sigma	275585-100ML
NHS	**normal horse serum**	Gibco	16050-122
PS	**penicillin-streptomycin**	Gibco	15140-122
PBS	**phosphate buffered solution**	-	-
PLL	**poly-L-lysine**	Sigma	P-6282
PDMS	**polydimethylsiloxane (Sylgard 184 Silicon Elastomer Kit)**	Paisley	-
NaOH	**sodium hydroxide**	Fisher	S318
	Syto13Green Nucleic Acid Stain	Molecular Probes	S7575
	SytoxOrange Nucleic Acid Stain	Molecular Probes	S11368
	TexasRed donkey anti-rabbit	Dylight	711-076-152
TEA	**triethanolamine**	Sigma	90279
	Triton X-100	Fisher	BP 151
	Trypan Blue	Sigma	T-6146
	Trypsin-EDTA	Gibco	25 300-062

Chapter 1.0

INTRODUCTION

1.0 Overview

Neural interfacing is a promising technique to restore function due to lost or malfunctioning signals in the central nervous system (CNS). Over the last few decades, neural interfacing has made many strides and neural prosthetics such as the cochlear implant and deep brain stimulation (DBS) are commonplace. Most recently, many achievements have been made in the field of neural recording and decoding, allowing the operation of robotic limbs for amputees or patients with paralysis. However, these interventions require the long-term implantation of recording and stimulating electrodes into the CNS. Currently, loss in electrode functionality (particularly for recording electrodes) is a major limiting factor. Upon implantation, many researchers report not only an increase in impedance, but also gradual loss in signal all together. Glial scarring, initiated by the native immune cells of the CNS (microglia and astrocytes) is believed to be a major contributing factor to the loss in electrode functionality. Current models (primarily *in vivo*) have provided a well-documented account of the cellular temporal response to the electrode upon insertion, but have failed to address to what degree different electrode parameters influence glial scarring. In order to successfully design an electrode that is compatible with the CNS over many decades, an improved high-throughput model is required. This model must not only support microglia and astrocytes, but also mimic the mechanical properties of the CNS.

1.1 Neural Prosthesis

Movement, sensation, thoughts, speech and memory are controlled by signals travelling through the spinal cord and brain. This biological system is known as the CNS. The CNS not only allows us voluntary control of our limbs, but also controls many vital organs. When the spinal cord is damaged due to trauma or disease, signals can no longer be sent from the brain to the body nor can the brain receive signals from the body inferior of the injury. CNS injury is a huge burden on both the healthcare system and quality of life for patients and caregivers. Spinal cord injury currently affects ~90 000 Canadians with full or partial paralysis and the estimated cost of neurological disorders and injuries in Canada exceeded $8.8 billion from 2000-2001 [1, 2]. Recent developments in the field of neural prosthesis show promising advancements towards replacing lost movement and sensation through neural recordings, stimulation and robotics [3, 4].

Hans Berger jump-started the field of neural prosthesis in 1929 when he recorded brain activity in the form of electroenchephalography (EEG) [5]. These recordings lead to the use of brain signals for robotic control. In 1969, Fetz et al. demonstrated that monkeys were capable of controlling the deflection of a biofeedback arm with neural activity, thus coining the term brain-computer interface [6]. Since then, brain-computer interfaces have been used to replace lost sight, hearing and movement to a limited degree. Cochlear implants (to restore lost function in the ear) and DBS (for the treatment of Parkinson's) are perhaps the most widely used and successful neural prostheses today. Bladder control and pain relief prosthetics are also currently available while visual and motor prosthetics are widely researched. A quadriplegic woman recently became the first human implanted with a cortical recording electrode array that gave her control of a robotic arm. This robotic arm allowed her to feed herself chocolate and drink coffee of her own volition [7]. In addition to upper limb prosthetics, the possibility of implanting microelectrodes into the spinal cord to stimulate lower limb movement below the point of injury (intraspinal microstimulation) is being researched. This technique has successfully stimulated lower limb movement in anesthetized felines [8]. These advancements shine light on the multitude of possibilities in the field of neural prostheses.

In the case of cochlear implants and DBS, electrodes are used to stimulate different regions of the CNS [9]. Visual prostheses also use stimulating electrodes but are currently limited by the need for microelectrode arrays and wireless transmission of large amounts of information. In contrast, current motor prostheses operate by recording signals from the CNS and use these signals to operate either external robotic limbs or stimulate existing neural tracts inferior to the injury. The requirement for signals to be received from the brain in motor prostheses also forms the necessity for consistent, chronic recordings [10]. Although studies have demonstrated recordings in animals (up to 3 years) and in humans (up to 9 months), further improvements must be made before motor prosthesis can be widely used [10-14].

Loss of functional recording electrodes has been attributed to the foreign body response [3, 9-11, 15]. Over time, glial cells in the CNS form a dense cellular sheath surrounding the electrode known as the glial scar, increasing both electrical impedance and pushing neurons further from the electrode [9, 15-17]. Although the glial scar is commonly cited as the reason for lost neural recordings, the exact cause and methods for mitigating the scar are

unclear [11]. Understanding why electrodes fail was identified as key to improving neural interfaces for chronic application at the Institute of Electrical and Electronics Engineers (IEEE) Grand Challenges in Life Sciences Conference, emphasizing the need to determine the causes for glial scarring and how to mitigate them [18]. *In vivo* animal models are the most common method for investigating the effects of different electrode design parameters on glial scarring [11]. This approach does not allow proper analysis of specific cell-cell, cell-ECM and cell-electrode interactions involved in glial scarring. *In vivo* models are also time consuming and expensive with many ethical implications and concerns. As such, an effective *in vitro* model is desirable to perform initial electrode testing and mechanistic studies [11].

1.2 Glial Scarring

Millions of people around the world have successfully received implantable devices that mean the difference between life and death or significantly improve quality of life. Traditionally, these implanted devices have been considered biocompatible when a small fibrous, avascular capsule is formed and the implant site is relatively quiescent [19, 20]. However, these inert materials tend to minimize the reconstructive aspect of the healing response and promote the formation of a fibrous capsule [19]. In light of this, it is perhaps not surprising that though implantable devices are considered to be an overall success, the FDA continues to report cases of failed implantable devices due to the foreign body response (580 reports in 2009) as the most common cause of implant failure [19].

Electrodes used to send and receive signals for neural prostheses also initiate a foreign body response. Due to the immune privileged nature of the CNS, this foreign body response is slightly different from implants in other regions of the body. The reaction to an implanted electrode is a cascade that can be split into five major events: injury due to initial implantation, protein adsorption, acute inflammation, chronic inflammation and glial scarring (Figure 1.1) [17, 19, 20].

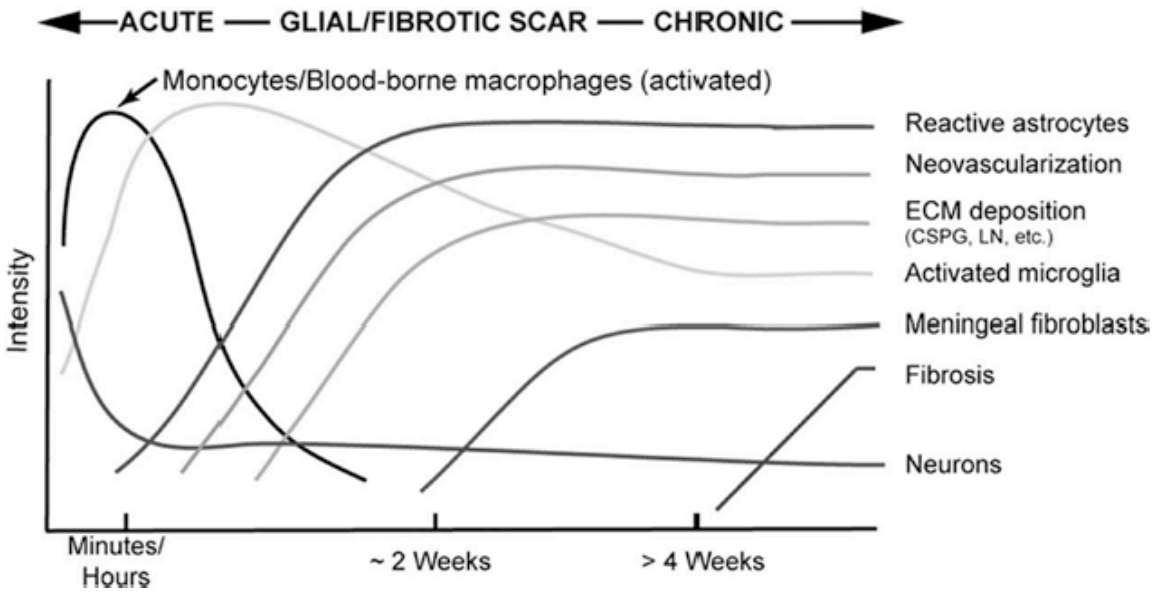

Figure 1.1: Temporal response of cells involved in the wound healing and foreign body response of the CNS to implants. With permission from Taylor and Francis Group LLC [17]

When an electrode is inserted into the brain or spinal cord it is pushed through the meninges, damaging capillaries and compromising the blood-brain barrier (BBB) [15]. Cells and proteins such as macrophages, neutrophils and clotting factors not typically found in the CNS are then able to enter through the compromised BBB [15]. Proteins from the blood (predominantly albumin and immunoglobulin) adsorb onto the electrode or material present [19-21]. Because protein adsorption occurs almost instantly and effects cell adhesion, many researchers hypothesize that cells interact primarily with the adsorbed protein layer and not the material itself [19, 22]. Neutrophils and monocytes entering through the breached BBB initiate the inflammatory cascade and wound healing response. Microglia and astrocytes respond shortly after, appearing activated at the site of electrode implantation and initiate the inflammatory response within the CNS (Figure 1.1) [15]. This stage is known as acute inflammation and is similar to the effects from a stab wound. The two CNS cell types primarily involved in the inflammatory response are microglia and astrocytes while the degree of acute inflammation is highly dependent upon electrode size and geometry, method of insertion and location in the CNS [17].

As the resident macrophages of the CNS, microglia take on the primary role of removing unwanted debris and pathogenic organisms. In their resting or ramified state, microglia have small cell bodies with many processes [23]. Microglia are crucial for neurorepair,

neurodegeneration and neuroinflammation [24]. In the event of injury or infection, microglia transform from a resting or ramified state to an activated state. In an activated state, microglia proliferate, take on a more compact morphology, phagocytose foreign material and release a wide variety of molecules [15]. Some of the molecules microglia release are free radicals, nitric oxide and proinflammatory chemokines and cytokines (IL-1, TNF-alpha and IL-6) [25]. These factors activate other microglia in the area as well as astrocytes [25].

In addition to microglia, astrocytes are one of the important CNS cell types associated with the foreign body response. The name astrocyte stems from the Greek word, "astron", for star. This is due to the numerous cellular extensions of the astrocyte, giving it a star-like morphology. Normal astrocytes take on a variety of roles including the development and function of synapses, the regulation of blood flow, maintenance of homeostasis, and inflammatory response [26]. In response to trauma, injury and stress, astrocytes transform from a normal to reactive state. The transition of astrocytes from normal to reactive is characterized by enhanced migration, proliferation, hypertrophy, changes in number and distribution of organelles and increased matrix production [27]. One of the roles of activated astrocytes is to repair the breached BBB and subsequently limit the inflammatory response initiated by cells outside the CNS. An electrode that is inserted and then removed immediately results in only an acute inflammatory response and the wound healing response of the CNS goes no further (no chronic inflammation is observed). Electrode tracks from wounds cannot be found several months after the insertion if the electrode is removed [15, 17].

If the electrode is left in the CNS, chronic inflammation and glial scarring ensues. Activated astrocytes release chondroitin sulfate proteoglycans (CSPGs) and other inhibitory molecules that create an environment blocking regrowth of neural processes [25]. Reactive microglia also remain at the surface of the electrode, attempting to phagocytose the foreign body [15]. Due to the robust microglial response and inhibitory molecules produced by astrocytes, the wound site is generally void of neurofilaments three days after injury [28]. Reactive astrocytes become more concentrated at the electrode, forming a physical barrier called the glial scar (Figure 1.2).

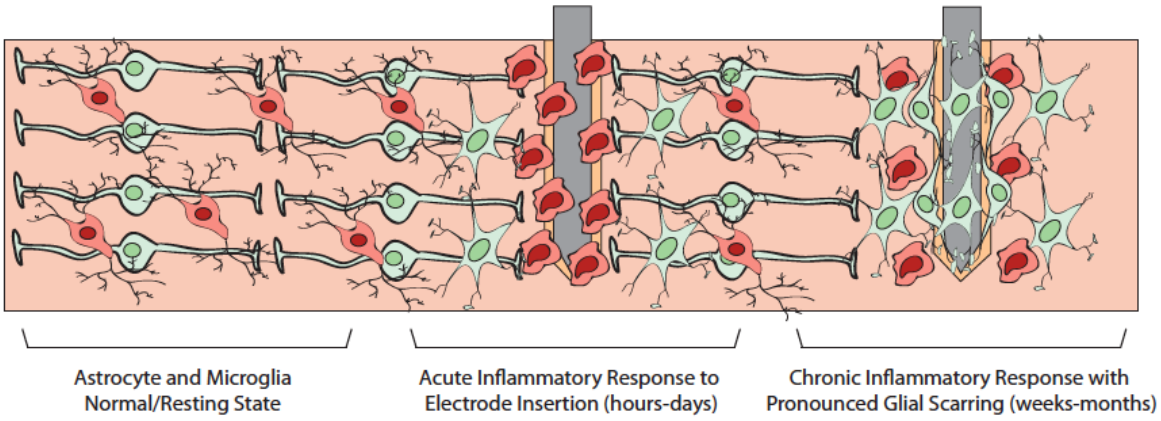

*Figure 1.2: Response of astrocytes (**green**) and microglia (**red**) to the electrode as a foreign body over time. Microglia (**red**) are the first to react, becoming activated and taking on an amoeboid morphology. Astrocytes (**green**) react later becoming hypertrophic and forming a dense glial scar around the electrode.*

It is important to mention that the presence of the glial scar is not in itself inherently bad. The glial scar is necessary to repair the BBB and return the CNS back to homeostasis. The primary issue is that cells in the vicinity of the electrode remain active and the glial scar becomes denser overtime resulting in increased electrical impedance. Increased impedance and lack of neurofilaments make it more difficult to obtain reliable neural recordings [9, 15, 17]. Many factors are reported to affect the extent of tissue reaction including electrode implantation method and design [25]. In order to obtain reliable chronic recordings, electrode design must be optimized to mitigate the wound healing and foreign body reaction.

1.3 Electrode Designs

Neural prosthesis design varies greatly depending on which function is being replaced or the disease being treated (hearing, sight, movement). However, the one common part in all neural prostheses is the electrode. The electrode is essential for communication with the CNS. It acts as a direct relay for signals from the stimulator to neurons in the CNS (stimulating electrodes) and signals from the CNS to a robotic limb or feedback loop (recording electrodes). As a result, functionality of the electrode is essential for the long-term clinical success of any neural prosthesis.

Neural prostheses that are currently implemented in the clinic rely solely on stimulating electrodes. In the case of DBS, electrodes are a few mm in diameter with a lead ~40 cm long

[29]. Electrodes have been inserted into the brain that are functional for over a decade in patients [30]. Stimulating implants, like DBS and cochlear implants, are currently used widely with human patients while implants designed to record from the CNS have experienced much less success [9]. Recording electrodes must be very sensitive in order to record and discern signals from neurons, which is easily disrupted by the glial scar [9]. Chestek et al. reported a 2.4% decrease in amplitude recorded from action potentials each month [13]. Recording arrays inserted into the motor cortex of monkeys failed between 3 months and 1.5 years [14]. Before electrodes may be used to record neural signals for clinical applications they need to reliably record activity for decades [15].

Current recording electrode designs vary between investigators and manufacturers, but may be split into two primary types (microwire and silicon micromachined electrodes). Microwire electrodes consist primarily of a conducting metal covered with an insulating material (Teflon or polyimide) organized into an array of 4-100 electrodes [15]. The metal may be platinum, gold, tungsten, iridium or stainless steel [15]. The silicon (Si) micromachined electrodes allow for more complex designs, but often provide lower quality recordings than microwire arrays [15]. Microwire arrays are also longer and reach deeper brain structures, but due to their flexibility they are reported to bend upon insertion [15]. The Utah electrode array (UEA) and the Michigan probe are two silicon electrode arrays that have become quite prolific (Figure 1.1) [15]. Although the UEA and Michigan probes are a huge success and are used regularly in experiments, they are still unable to provide chronic recordings for the duration required in clinical use.

Many studies have been done to determine which electrode designs optimize neural recordings. Generally designs are focused on the geometric, mechanical or bioactive properties of electrodes. Geometric designs focus on the shape of the electrode and the arrangement of arrays. Thelin et al. demonstrated that smaller (50 μm vs 200 μm diameter) electrodes implanted in rat cortex over 12 weeks had significantly lower glial scarring response [31]. Another study showed that the glial response to an array of electrodes was not significantly greater than a single electrode [32]. Interestingly, electrodes in the center of the array appeared to be 'shielded' with less glial scarring than outer electrodes [32]. The effect of geometry on glial scarring is likely linked to trauma upon electrode insertion. Speed, shape and arrangement can produce varying amounts of vascular and cell damage which

greatly regulate the acute foreign body response [9]. However, other studies have indicated that electrode geometry has no impact on the degree of glial scarring [33]. Many studies have also linked glial scarring to the mechanical properties of the electrode and array setup. Tethered electrodes have been shown to increase glial scarring when compared to floating electrodes due to inability of the microwire to move with CNS tissue during micromotion [34]. Other studies have investigated the mechanical mismatch between electrodes and CNS tissue [9, 17]. Mechanical mismatch could apply harmful stress on CNS tissue resulting in chronic glial cell activation due to micromotions caused by blood flow or movements during daily life [17]. Bioactive coatings are another area of great interest to researchers. This approach involves the delivery of drugs or peptide coatings designed to attenuate inflammation or promote neurite growth [17, 35-37].

The optimal electrode design is likely a combination of geometry, mechanical and bioactivity designed to mitigate the foreign body response and encourage neurite growth. This optimal design would also need to be modified to accommodate different requirements based on where the electrodes are used (surface vs deep, brain vs spinal cord). Due to the multiple testing parameters as well as confounding variables in an *in vivo* model system, it is difficult to determine which factors are significant and to what degree they affect glial scarring. An effective *in vitro* model system could pinpoint contributing factors and enable effective electrode design.

1.4 Current Glial Scarring Models

Glial scarring is believed to be a major contributing factor to the loss of functional recording electrodes over time. The chronic inflammatory response of CNS tissue to the electrode as a foreign body results in a dense sheath of astrocytes encapsulating the electrode (glial scar) and neurites pulling away from the electrode due to inhibitory factors released by cells involved in the foreign body response. The cells of interest, (microglia, astrocytes and neurons), are easily identified by novel proteins they express. Immunofluorescence has therefore become an integral part of assessing the extent of glial scarring. In general, the density of cells near the electrode is evaluated qualitatively or quantitatively. If there is an increase in cell density over time, an increase in glial scarring is reported.

1.4.1 In vivo models

The most common model of glial scarring in the presence of electrodes is *in vivo* testing. In the *in vivo* models, electrodes are inserted into animal tissue (most often rat cortex). The animals are then sacrificed at various time points, the electrode is removed, the tissue is sectioned and then labeled to assess the extent of glial scarring. A summary of studies using an *in vivo* glial scarring model is presented in Table 1.1. As discussed in Section 1.2, these studies have led to the general conclusions that smaller, flexible, untethered electrodes result in decreased glial scarring. However, variation between electrode materials, preparation, coatings, insertion method and duration of the experiment makes it difficult to compare findings across studies. Animal testing also adds an additional layer of complexity to experiments. This complexity makes it difficult to determine which factors are contributing to a loss in electrode functionality. In addition to this, time and cost of *in vivo* experiments limit the number of parallel tests and statistical verification of results.

Table 1.1: Summary of studies comparing region, experiment duration and electrode type for in vivo models.

Animal	Duration	Electrode				Cite #
		Design	Coating	Shank Size (um)	Tethered	
Rat cortex	6 weeks	Pt microwires	PEDOT/CNT	100	N/A	[38]
Mouse cortex	12 hours	Michigan probe (Si)		15 by 100	N/A	[39]
Rat cortex	6 weeks	Si array	Ceramic loaded with poloaxmer	113 to 66.4	Yes	[40]
Rat cortex	4 weeks	Michigan probe (Si)	-	100 by 15	Yes	[41]
Rat cortex	4 weeks	Stainless steel microwires	Polyimide	50	Yes	[42]
Rhesus macaque and Feline	112 weeks	Si array	Parylene-C	100 by 1	N/A	[43]
Rat somatosensory cortex	6 weeks	Tungsten array	Polyimide	50	Yes	[44]
Rat cortex	4 weeks	Tungsten microwires	L1 protein coating	-	No	[45]
Rat cortical tissue	16 weeks	Utah array (Si)	-	123 by 15	Yes	[46]
Rat cortex	6 weeks	Tungsten microwires	Polyimide stiffened with gelatin	300	No	[32]
Monkey motor cortex	128.6 weeks	Si array	-	100 by 1	N/A	[13]
Rat cerebral cortex	8 weeks	Nano composite tungsten microwires	Teflon	100 by 203	Yes	[47]
Rat cortex	6 weeks	Si array	Parylene-C	200 by 100	Yes	[48]
Rat cortex and thalmus	5.2 weeks	Pt electrode tracks on polyimide	Polyimide (stiffened with saccharose)	40	Yes	[49]
Rat brain	12 weeks	Stainless steel microwires	-	50 and 200	Yes	[31]
Rat spinal cord	4.4 weeks	Pt/Ir microwires	Polyimide	30	Yes	[50]
Rat cortex	12 weeks	Si microwires	Parylene-C	(200 to 33) by (15 to 2)	Yes	[51]
Rat brain	16 weeks	Michigan probe (Si)	-	100 by 15	Yes	[52]

Table 1.1 cont.: Summary of studies comparing region, experiment duration and electrode type for in vivo models.

Animal	Duration	Electrode				Cite #
		Design	Coating	Shank Size (um)	Fixed	
Rat thalmus	4 weeks	Cu and Cr tracks on polyimide	Polyimide	16	Yes	[53]
Rat cortex	8 weeks	Tungsten microelectrodes	Teflon coating	114	Yes	[54]
Rat motor cortex	12 weeks	Si microwires	Various	(200 to 33) by (15 to 2)	Yes	[55]
Rat auditory/ somatosensory cortex	14.3 weeks	Au tracks on polyimide	Polyimide	-	Yes	[56]
Rat cortex	4 weeks	Michigan probe (Si)	Peptide coating	30 to 200 by 15	Yes	[36]
Mouse cortex	1 week	Pt etched electrodes	Polyimide	-	N/A	[57]
Rat cortex	4 weeks	Si microwires	DEX coating	100 by 15	Yes	[58]
Rat auditory cortex	4 weeks	Microelectrodes	-	50	Yes	[59]
Rat cortex	4 weeks	Si microwires	-	(200 to 33) by (15 to 2)	Both	[34]
Rhesus macaque cortex	156 weeks	Pt microwires	-	50	Yes	[60]
Rhesus macaque motor cortex	78 weeks	Si arrays	Parylene-C	-	Yes	[14]
Rat cortex	4 weeks	Michigan probe (Si)	-	(200 to 33) by (15 to 2)	Yes	[61]
Rat somatosensory cortex	13 weeks	Pt on ceramic base	Alumina ceramic	-	Yes	[62]
Rat brain	12 weeks	Si microwires	-	~ 200 by ~ 60	Yes	[33]
Feline cortex	16 weeks	Ag-Ag-Cl on Pt	Parylene-C, Pyraline and HR605-P	Discs 1100 diameter by 75	Yes	[63]

1.4.2 2D in vitro models

Due to the restrictions of *in vivo* testing, some researchers have pursued *in vitro* models for glial scarring. *In vitro* cell culture allows scientists to analyze systems in a controlled, reductionist manner. Currently, most *in vitro* studies are done in 2D cell culture environments. 2D cell cultures utilize either immortal cell lines or primary cells removed from tissue that are plated onto hard plastic culture plates. These cell cultures allow more control over experimental variables than *in vivo* systems, making it possible to analyze individual factors such as electrode size and micromotion without extraneous influences. Due to its reductionist approach, *in vitro* testing has led to many discoveries that would not be possible to determine in an *in vivo* system.

2D models for glial scarring generally fall into three categories: cell adhesion, scratch, and wire drop assays. Cell adhesion assays involve cells of interest being seeded onto a wire or a surface coated with the proposed improved biocompatible substrate. Some authors have suggested that reduced cell adhesion will result in an attenuated cellular response and improved biocompatibility because cells must first adhere to a surface before they release proinflammatory factors. Other researchers have proposed that the increased attachment of certain cells will decrease electrode micromotion and improve neural recordings [64]. Scratch assays were designed to model the reaction of cells to mechanical injury. The mechanical injury is modeled when a cell scraper or pipette tip is run along the bottom of a culture plate well. Cells are then monitored to see how quickly they migrate and proliferate to fill the gap [11]. In order to test the reaction of cells to a foreign body in 2D, a wire drop assay is used. The wire drop assay involves one or more electrodes being dropped onto established mixed cultures. The cellular response to the wire is then monitored [11, 65, 66]. This model has been used to compare various electrode coatings, but is unable to model the effects of mechanical motion and 3D environment on glial scarring [11, 67].

Used together or separately, 2D models can be used to answer specific questions about glial scarring in a more cost effective and less time consuming manner than *in vivo* testing. However, 2D culture is by no means a replacement for *in vivo* studies. 2D cultures are incapable of fully modeling the complex environment of the CNS and an *in vivo* study must always be carried out before moving forward with clinical studies. The power of *in vitro* models comes instead from performing initial high throughput analyses and understanding

in depth mechanisms of glial scarring. These studies can then be used to improve electrode design.

1.4.3 3D in vitro models

Although traditional 2D *in vitro* cell culture has obvious advantages, it also has limitations when it comes to realistically modeling CNS tissue. In 2D monolayer cultures, ~50% of the cell surface is exposed to a stiff polystyrene surface and ~50% of the cell surface is exposed to culture media [68]. This affects not only how the cells interact with soluble products in the media (drugs, proteins, etc.), but also how cells interact with each other[69]. In the case of cancer cells, this has been shown to be of particular relevance when determining how these cells respond to drugs and stimuli [68-70]. However, changes in cell characteristics and behavior including cell proliferation, cell differentiation, gene expression and stimuli response have also been observed for other cell types [71]. Changes in cell characteristics and behavior observed between 2D and 3D cultures are attributed to stiffness, adhesion, mechanotransduction and signaling in response to soluble factors (Figure 1.3) [71-73]. 3D culture is a method capable of maintaining the simplicity and control of 2D cultures while modeling an environment more similar to that seen *in vivo.* As a result, 3D culture is quickly becoming a stepping-stone between 2D cultures and animal testing.

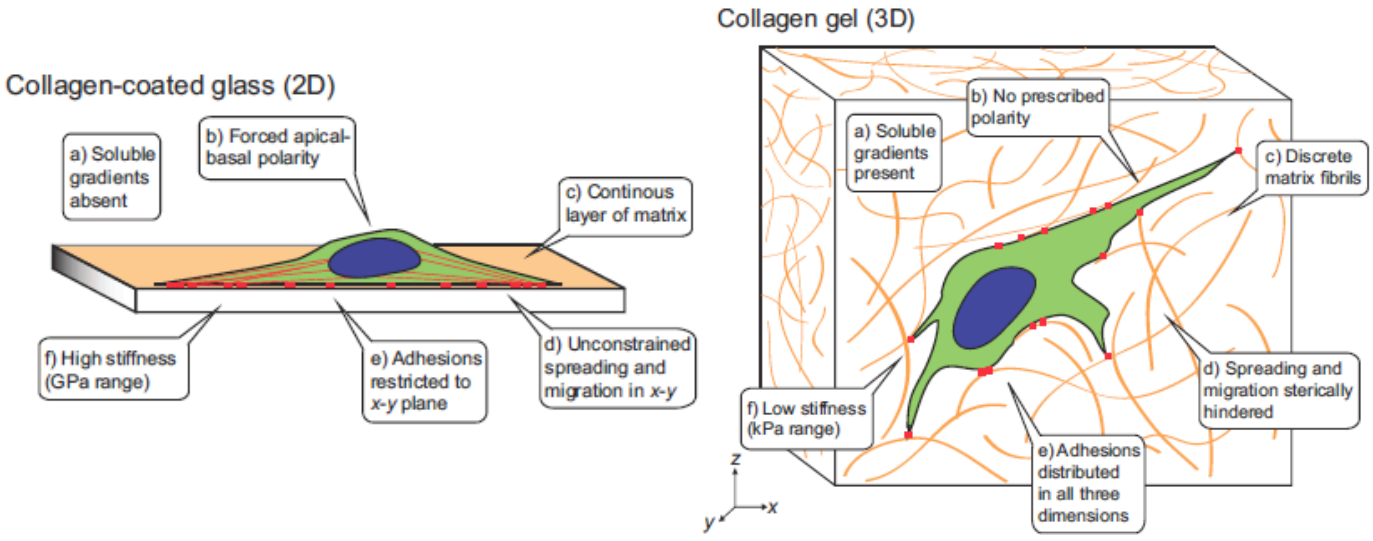

Figure 1.3: Depiction of different cues received by cells in 2D and 3D culture systems. Reprinted with permission from Christopher Chen. [71]

3D *in vitro* glial scarring models are either organotypic cultures or engineered scaffolds containing cell types of interest (microglia, astrocytes and neurons).

Organotypic cultures involve the removal of whole tissue from the animal that is then sliced into thin sections and cultured *ex vivo*. The thin nature of the slices allows cells in the tissue to survive for an extended period of time in supplemented media. The advantage of organotypic cultures is that they maintain cellular connections and the ECM environment native to that tissue. Ereifej et al. used organotypic 400 nm brain slices to model the foreign body response to polydimethyl siloxane (PDMS) nanopatterned pins [74]. The pins were placed on top of the organotypic cultures (not inserted) immediately after tissue was sliced to mimic the breach of the BBB during electrode insertion [74]. Although the authors did report a foreign body response to the PDMS pins, this model did not allow cells to interact with the 3D nature of the PDMS pin and doesn't allow a reductionist approach to evaluating electrode biocompatibility.

Engineered scaffolds are 3D structures that encapsulate cell types of interest (microglia, astrocytes and neurons). This structure is meant to mimic the ECM of the tissue to provide cues that may be missing in 2D cultures. One common commercially available scaffold is Matrigel. Matrigel is a gelatinous mixture containing laminin, entactin and collagen obtained from mouse sarcoma cells that is liquid at 4 °C and becomes solid at 37 °C. Cullen et al. used Matrigel as a scaffold to encapsulate astrocytes and neurons as a model for glial scarring [75]. In this model, no electrode was used, instead the reaction of neurons and astrocyte to mechanical deformation was investigated [75]. Frampton et al. utilized a modified alginate gel to look at glial scarring in response to an array of 16 iridium (Ir) neural probes. The modified alginate gel encapsulated astrocytes and microglia around the neural probe array in the presence of Ca^{++} ions [76, 77]. After 2 weeks, the alginate model exhibited similar cell distributions (microglia redistribution to electrode) to that previously reported *in vivo* and *in vitro* [77].

Both matrigel and alginate model systems produced a 3D environment and successfully cultured glial cells and neurons. However, these models do not fully model the ECM of the CNS. Native CNS contains relatively small amounts of fibrous proteins such as collagens and fibronectins (the primary components of Matrigel) and no alginate [78]. Instead, the ECM of the CNS is made up of large amounts of glycosaminoglycans [78]. Glycosaminoglycans are highly polymerized, unbranched chains of repeating disaccharide units. In their bound form

they form proteoglycans and when unbound they appear in the form of hyaluronic acid (HA) [78]. In addition to containing proteins not present in the CNS, neither the matrigel nor the alginate cultures demonstrate tunable mechanical properties. The CNS is a heterogeneous tissue with varying mechanical properties throughout [79]. Due to this heterogeneous nature, different regions of the CNS (white matter vs grey matter and brain versus spinal cord) are expected to have different elasticity or stiffness values. Stiffness is known to influence both cell behavior and electrode mechanical compatibility, making it a very important model parameter. To test the effect stiffness has on glial scarring, a matrix with tunable mechanical properties is necessary. Therefore, an improved 3D culture system for microglia and astrocytes capable of supporting an inserted microelectrode over the period of several weeks with tunable mechanical properties is required.

1.5 Experimental Outline

This thesis describes the development of a new 3D *in vitro* glial scarring model based on hyaluronic acid. This model is intended to allow the testing of multiple electrode designs and conditions simultaneously (be high-throughput) and a reductionist approach to electrode design. The model must also support the insertion of a microwire electrode over the period of several weeks and mimic the mechanical properties of the CNS. The model was developed in three parts: gel synthesis and characterization, preliminary 2D culture and cell-gel integration. Chapter 2 describes the development of a hyaluronic acid based scaffold capable of photocrosslinking under a green light emitting diode (LED) with tunable mechanical properties. Many factors were considered during development of the scaffold to ensure viable cell encapsulation and functionality of the glial scarring model including porosity and stability. Chapter 3 standardizes a method for the isolation and culture of microglia and astrocytes from whole tissue. Cell morphology and glial scarring in 2D determined in Chapter 3 were later compared to that in the 3D culture model. Chapter 4 evaluates the effects of cell encapsulation and changing scaffold properties on mixed glial cultures. This chapter also assesses the feasibility of using a 3D hyaluronic based scaffold as a model of glial scarring. Finally, the conclusions derived from the thesis are summarized in Chapter 5 and possible future directions are discussed.

Chapter 2.0

GEL SYNTHESIS AND CHARACTERIZATION

2.0 Introduction to Gel Synthesis and Characterization

This chapter explores the selection, synthesis and use of methacrylated hyaluronic acid (HAMA) as a scaffold for the encapsulation and culture of microglia and astrocytes. The cell encapsulation system standardized here is used later as a 3D model for glial scarring in Chapter 4. Cell encapsulation requires a cytocompatible material that is capable of transforming from an aqueous solution to an insoluble matrix *in situ*. In the case of HAMA, an aqueous solution is transformed under light into an insoluble matrix in the presence of suitable precursors. These precursors absorb the emitted light to form a radical, initiating radical crosslinking of macromer chains. The material, light and precursor solution must not only be biocompatible with cells before and during encapsulation, but also post-encapsulation when it has formed a matrix/scaffold. Unlike 2D cultures where cells are grown in a monolayer and have no barriers to migration or access to nutrients from media; cells in 3D culture navigate and modify their surroundings. As a result, many factors must be considered when developing a 3D culture system including porosity, culture stability and mechanical properties. Once crosslinked, the gel must also be easily manipulated, model the mechanical properties of the CNS and anchor a floating microwire before it can be used as a high-throughput model of glial scarring. To ensure the HAMA gel met all of these requirements, gel synthesis was standardized, precursors and light source for initiation were selected to ensure biocompatibility, a high-throughput system was developed and the gel was characterized (dynamic modulus, swelling behavior and gel structure). These results are used to further understand interactions between cells and the scaffold in Chapter 4.

2.1 HAMA Material Selection

The scaffold material used during 3D cell culture takes the place of the extracellular matrix (ECM) *in vitro.* As such, a scaffold for a 3D glial scarring model should fill the role of the CNS ECM as closely as possible. Choosing this material is not trivial, as many variables affect its success including architecture, cytocompatability and mechanical properties. The architecture of the scaffold must be porous enough to support cell growth and allow diffusion of nutrients while still maintaining sufficient mechanical integrity. The scaffold material and all of its components must also be

cytocompatable to minimize cells death as well as allow cell migration and attachment. These factors require mechanical and receptor based cues natively supplied by the ECM. In addition, using the 3D culture as a model of glial scarring adds further requirements such as homogenous cell distribution throughout the matrix, high-throughput production potential and the ability to easily modify mechanical stiffness to model different CNS tissue regions.

As discussed in the introduction, current 3D culture systems for glial scarring are based on materials used originally for cells present outside the CNS. Current cultures contain large amounts of fibrous proteins such as collagens and fibronectins as well as alginate that are not natively found in the CNS. Instead, native CNS ECM is composed of large amounts of glycosaminoglycans [78]. Glycosaminoglycans are highly polymerized, unbranched chains of repeating disaccharide units. In their bound form they form proteoglycans and when unbound they appear in the form of hyaluronic acid (HA) [78]. Hyaluronic acid is found widely throughout the body and is particularly abundant in the CNS [72, 80-83]. As a major component of the ECM, it is known to contribute to cell proliferation, signaling, migration and wound healing [84, 85].

When mixed with water, HA becomes a hydrogel and imbibes large quantities of water. This property has made it a popular cell scaffold used for many neural tissue applications though not as commonly for the growth of microglia and astrocytes [25, 86]. Through a simple benchtop reaction, HA may be conjugated with a methacrylate side group forming methacrylated hyaluronic acid (HAMA). This reaction enables cell encapsulation via radical crosslinking at 37 °C to form a porous hydrogel scaffold [87]. Hyaluronic acid is also able to bind to cell surface receptors (CD44 and RHAMM) and provides the mechanical cues necessary for cell proliferation and attachment [72, 83, 84]. Previous studies have demonstrated that the mechanical properties (swelling, porosity and stiffness) of HA gels are highly tunable, making it a good candidate for modeling various regions of the CNS (white vs. grey matter and brain vs spinal cord) [72, 73, 83, 88, 89]. Due to its tunable nature, capability of *in situ* crosslinking and similarity to CNS ECM, HA was chosen as the scaffold material for this 3D glial scarring model.

2.2 HAMA Macromer Synthesis

To enable radical crosslinking of HA and consequently cell encapsulation, a methacrylate group must first be attached to the backbone of the HA macromer, producing HAMA. The vinyl groups on the attached methacrylate are then able to react during crosslinking to create covalent bonds between HAMA macromers forming an insoluble matrix or gel [90]. HAMA synthesis is a nucleophilic reaction whereby an OH group on the HA macromer acts as an electron donor (Figure 2.1 and Equation 2.1) [91]. This synthesis should be consistent and reproducible for HAMA to be used as a 3D culture and for high-throughput testing of electrode parameters. The repeatability and extent of the reaction was evaluated through percent yield calculations and nuclear magnetic resonance spectroscopy.

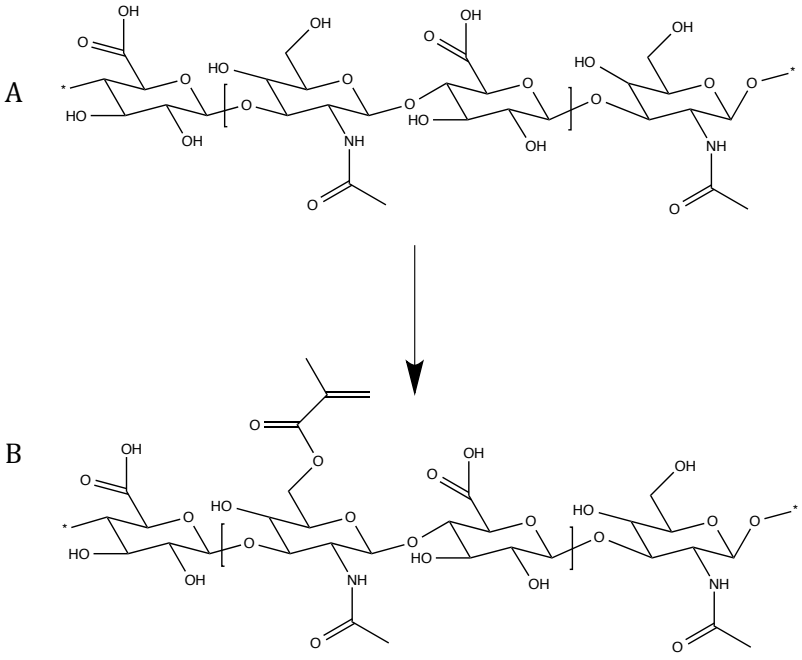

Figure 2.1: Unmodified hyaluronic acid (A) is modified with methacrylate groups (B).

$$2 \cdot C_{14}H_{21}NO_{11} + C_8H_{10}O_3 \rightarrow 2 \cdot C_{18}H_{25}NO_{12} + H_2O \quad [2.1]$$

For the reaction shown in Figure 2.1, hyaluronic acid sodium salt was dissolved in distilled water (ddH_2O) to a concentration of 1.0 wt%. Methacrylic anhydride (Sigma) was added dropwise in 20-fold excess while a pH of 8-12 was maintained with 5 M NaOH (Sigma) and monitored via pH paper. Because methacrylic

anhydride was not soluble in water, the reaction occurred in two-phases and required vigorous mixing to ensure the reaction went to completion. After multiple uses under an ambient air atmosphere, methacrylic anhydride reacted with moisture in the air to form methacrylic acid no longer capable of reacting with hyaluronic acid [92] (Equation 2.2).

$$C_8H_{10}O_3 + H_2O \rightarrow 2 \cdot C_5H_6O_2 \quad [2.2]$$

This conversion was found to detrimentally affect methacrylation after approximately 6 months (stock bottle opened weekly to an ambient air atmosphere). To avoid conversion of methacrylic anhydride to the acid form, the stock bottle was stored in a N_2 purged glovebox and single use aliquots (1000 µL to 3000 µL) were prepared. These aliquots were then wrapped in parafilm and stored in a vacuum desiccator. Various other methods have been developed to combat this issue in literature including using DMSO as a solvent or DMF as a co-solvent and reacting with glycidyl methacrylate instead of methacrylic anhydride [72, 80, 85, 92].

After all methacrylic anhydride was added, the solution was vigorously stirred (magnetic stirrer) for an additional 30 min. and the pH was monitored, covered with parafilm and incubated at 4 °C overnight. The next day, methacrylated hyaluronan (HAMA) was precipitated in cold acetone or ethanol. The precipitate was removed with forceps and placed into a microcentrifuge tubes for lyophilization (freeze drying). When lyophilization was complete, the sample was then ground to a powder using a mortar and pestle and stored at -20 °C until use. The average percent yield was determined to be 91.06 ± 13.83 % over ten trials.

2.2.1 Quantifying Degree of Methacrylation

The degree of methacrylation is known to effect hydrogel properties and was maintained between HAMA preparations. The relative number of methacrylate groups attached to hyaluronic acid macromers was verified with proton Nuclear Magnetic Resonance (NMR) spectroscopy. NMR spectroscopy is a technique that differentiates between protons based on differences in proton spin. Atoms in similar

configurations resonate at similar frequencies. In the case of methacrylated hyaluronic acid, the proton signal from an OH group was replaced with the proton signal from a CH_2 group, not present prior to the reaction (Figure 2.1). The average percent methacrylation was calculated by dividing the relative integrated intensity of the two methacrylate proton peaks (~6.1 and ~5.6 ppm) by the ten CH groups on the sugar (broad peak between ~4.0 – 3.0 ppm) [85]. A representative NMR spectroscopy image used to calculate percent conjugation of initial reaction is shown below (Figure 2.2). The average degree of modification was determined to be 93.89 ± 7.77 % over ten trials.

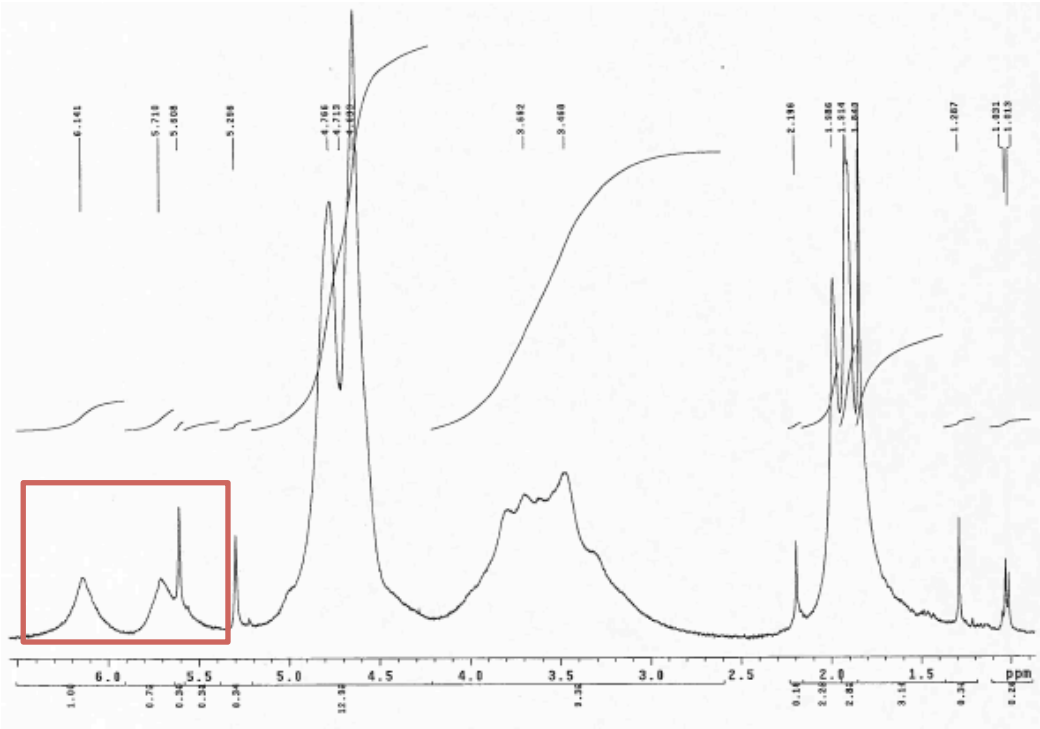

Figure 2.2: Representative NMR spectra after methacrylation using initial reaction protocol. Distinctive methacrylate proton peaks can be seen at ~6.1 and ~5.6 ppm (in red boxed area).

Initially, HAMA was synthesized in small quantities using 50 mg of HA, yielding an average of 53.00 mg of HAMA. In order to create a useable high-throughput technique, it was important to upscale the reaction and increase HAMA batch size without decreasing the percent yield or the percent modification. To increase yield, the reaction was scaled up 7.5 times the initial reaction using 375 mg of HA and 3000 µL of MA. Ensuring vigorous mixing during the addition of MA, successfully increased batch size without significantly changing percent yield. NMR spectroscopy

was used to verify methacrylation and determine the degree of methacrylation (Figure 2.3).

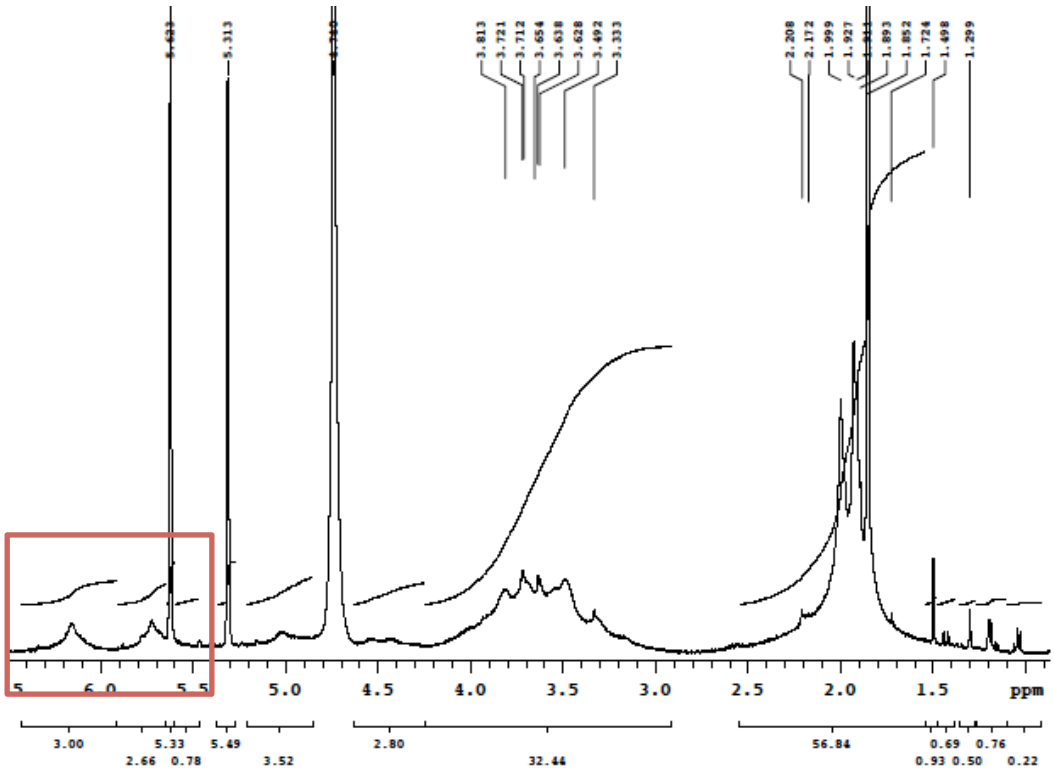

Figure 2.3: Representative NMR spectra after methacrylation using scaled up reaction protocol. Distinctive methacrylate proton peaks are at ~6.1 and ~5.6 ppm (in red boxed area).

Both the initial and upscaled reaction resulted in successful methacrylation as was evident from the methacrylate proton peaks at ~6.1 and ~5.6 ppm. In both spectra, there was a sharp peak at ~ 5.6 ppm that overlapped with the broader methacrylate peak. This peak is likely due to unreacted methacrylic anhydride that has become methacrylic acid. NMR spectra of methacrylic acid in literature indicate a sharp peak at ~5.6 ppm [93]. The yield, percent yield and percent modification for the initial and upscaled HAMA syntheses are sumarized in Table 2.1. HAMA synthesis was succesfully upscaled by 7.5 times the initial reaction as there is no significant difference between the percent modification or percent yield for the initial and upscaled reactions.

Table 2.1: HAMA reaction table for both initial and upscaled reactions.

HA (mg)	H2O (mL)	MA (µL)	Yield (mg)	Yield (%)	Modification (%)
50.00	5.00	400.00	53.00 ± 8.05	91.06 ± 13.83	93.89 ± 5.88
375.00	37.50	3000.00	420.60 ± 50.03	93.74 ± 7.77	94.48 ± 10.56

2.3 Selection of Photocrosslinking Components

After standardizing and upscaling HAMA synthesis, the precursors and light source used for photoencapsulation were chosen. To minimize cell death during encapsulation, the precursors and light source were selected for cytocompatibility. As described in Section 2.1, HAMA is capable of radical crosslinking to produce insoluble gels. Radical photocrosslinking occurs when radicals formed via light irradiation of precursors initiate crosslinking between macromer chains. Photocrosslinking has been used to encapsulate cells in polymer networks with varied stiffness, porosity and mesh size [72, 84, 94]. Radical crosslinking is dependent on photoinitiator concentration and type, light intensity, macromer concentration and degree of methacrylation [72]. Often, an ultra violet (UV) sensitive precursor is used because it requires only one precursor for the initiation of radical crosslinking. However, UV radiation is known to cause cell death and DNA mutations [95-97]. To avoid potential DNA mutations and cell death linked to UV exposure, a three-component precursor solution capable of excitement under high intensity green light emitting diode (LED) light (~520 nm, 60 mW, Cree XPE) was used. This three-component system was composed of triethanolamine (TEA, Sigma), 1-vinyl-2-pyrrolidinone (NVP, Sigma) and eosin Y (EY, Sigma). When excited by LED light, EY (the photosensitizer) gives an electron to TEA, creating radicals that initiate crosslinking. NVP accelerates radical formation [98].

These precursors were tested previously on mixed glial cultures to assess toxicity [99]. At higher concentrations (0.1 mM EY, 1 % (w/v) TEA and 0.2 % (w/v) NVP) significant cell death was observed [99]. However, when the precursor concentration was lowered (0.1 % (w/v) TEA, 0.1 % (w/v) NVP and 0.01 mM EY)

only minimal cell death was observed [99]. As free radicals are known to be toxic to cells, increased cell death upon light exposure occurred and was expected [99]. Cell death should be attenuated during encapsulation as the radicals affecting cells are instead being used to crosslink macromer chains. All further photocrosslinking and photoencapsulation used the most biocompatible precursor concentrations tested of 0.1 % (w/v) TEA, 0.1 % (w/v) NVP and 0.01 mM EY.

To prepare the gels, lyophilized HAMA was rehydrated in phosphate buffered saline (PBS) at the desired concentration (0.5, 0.75, 1.0 and 1.5 wt%) and allowed to sit overnight at room temperature. The next day the aqueous HAMA was thoroughly vortexed and/or triturated to ensure complete mixing. All precursors were added immediately prior to photopolymerization and thoroughly mixed. Aqueous HAMA and precursors were then injected via pipette onto a glass slide and exposed to LED light (~520 nm, 60 mW) for 2 min. After LED exposure the HAMA precursor solution had crosslinked to form an insoluble gel at all macromer weight fractions tested. Macromer weight fractions higher than 1.5 wt% were not tested because the precursor solution became too viscous for thorough mixing.

2.4 High-throughput Photoencapsulation System

After individual gels were successfully crosslinked using the established photoencapsulization system, it was modified to allow high-throughput and sterile photoencapsulation. To achieve a high-throughput system, multiple gels must be crosslinked at once in a repeatable and consistent manner. This required the design of appropriate molds to control gel shape and thickness as well as a method for handling multiple gels at once. To ensure consistent exposure to the LED light source and minimize contamination during crosslinking, an enclosure was developed. A method for gel attachment to glass coverslips was also developed to ensure stability through media changes during culture and immunolabelling procedures (requires regular changes of liquid surrounding the gel) as well as allow gel manipulation for microwire insertion. All of the equipment used for photocrosslinking and encapsulation was tested to ensure it could be sterilized for use in cell culture, reducing the chance of culture contamination without

detrimentally altering function. To achieve a reliable and consistent photoencapsulation system, a mold and holding mold were designed, a method for adhering gels to the glass was developed and an enclosure was set up to house the high intensity LED.

2.4.1 Gel Mold and Holding Mold

Molds for crosslinking were made from Polydimethylsiloxane (PDMS) (Sylgard, Dow Corning Ltd.) with an outer diameter of 15 mm and an inner diameter of 10 mm. Dimensions for cell culture gels were chosen based on microscope limitations (depth of ~1 mm) and coverslip diameter restrictions (18 mm for 12 well plates). These PDMS gaskets fit easily within the diameter of the glass coverslips, were resistant to high temperatures to allow sterilization and were reversibly adhesive so they could be used for multiple encapsulations. Molds for culture were stored in a solution of 70% EtOH. These molds were also used to produce gels for swelling and Cryo Scanning Electron Microscopy (SEM) experiments discussed later in Section 2.4. Similar PDMS molds with a height of 1 mm and a diameter of 25 mm were used for rheometry experiments later in this chapter, as the parallel plate was not available with a diameter smaller than 25 mm.

Although PDMS gasket molds controlled the height and diameter of the gels, crosslinking still occurred in the open bench-top environment without any protection against contamination and it was challenging to move coverslips during encapsulation without touching them or disturbing the gel before it was crosslinked. To improve aseptic technique and manipulation of the gels during crosslinking, a holding mold was designed. The holding mold was milled from an acrylic block to hold 24 coverslips and fit a typical culture plate lid allowing the simultaneous encapsulation of 24 gels in a sterile environment (Figure 2.4). Acrylic is also resistant to the high temperatures used during standard autoclave procedures so it may be sterilized between uses.

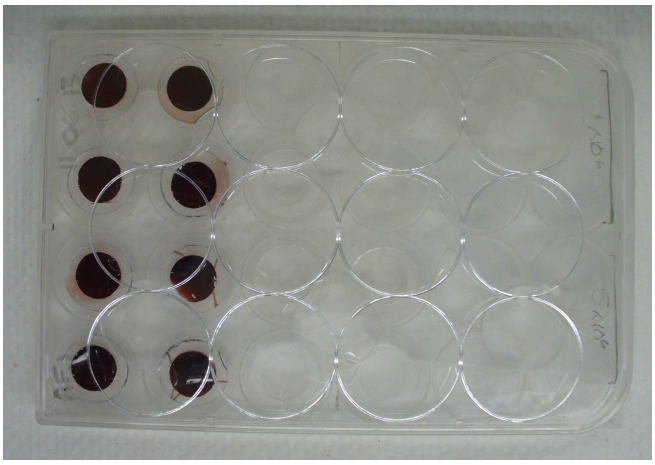

Figure 2.4: Acrylate holding mold with coverslips and PDMS molds. Some molds were filed with dye to increase contrast and demonstrate where the cell suspension would be placed.

2.4.2 Gel Attachment to Coverslips

HAMA gels slide easily across glass and plastic surfaces making them difficult to manipulate and move. Because gels must be removed from culture media during electrode insertion and the gel must stay in place during media changes and labeling procedures, a method of gel attachment to glass coverslips was standardized. Because Poly-L-lysine (PLL) was readily available in the lab and has been used in other 3D culture systems to encourage gel adhesion, it was used to attach gels to glass coverslips. PLL is a positively charged amino acid polymer commonly used in labs to encourage adhesion. It increases the electrostatic interaction of negatively charged ions by increasing the number of positively charged sites for binding. For coatings in all experiments, 50 μg/mL PLL was used (diluted in sterile ddH_20). The PLL mixture was left on coverslips overnight and aspirated the day of crosslinking then allowed to dry fully. PLL successfully attached adhered HAMA gel to glass coverslips as shown in Figure 2.5. Some gels were still lost during culture and immunolabelling, but the majority of gels were intact with gentle washing and careful handling.

Figure 2.5: HAMA gel adhered to glass coverslip with PLL coating to allow gel manipulation and stability during media changes

2.4.3 Photoencapsulation Enclosure

To further standardize the photoencapsulation system and improve aseptic technique, an enclosure was added. The enclosure was made out of black box board to prevent the user from being exposed to high intensity light during use (Figure 2.6). This enclosure housed the high intensity LED light source and held it at a constant height to ensure light intensity was constant at 60 mW for all encapsulations. A sliding door was also added to allow easy removal of the handling mold after encapsulation. A switch between the power source and the LED light allowed the user to control light exposure (Figure 2.6). Both the power source and enclosure were sterilized with 70 % EtOH before use in the laminar flow hood.

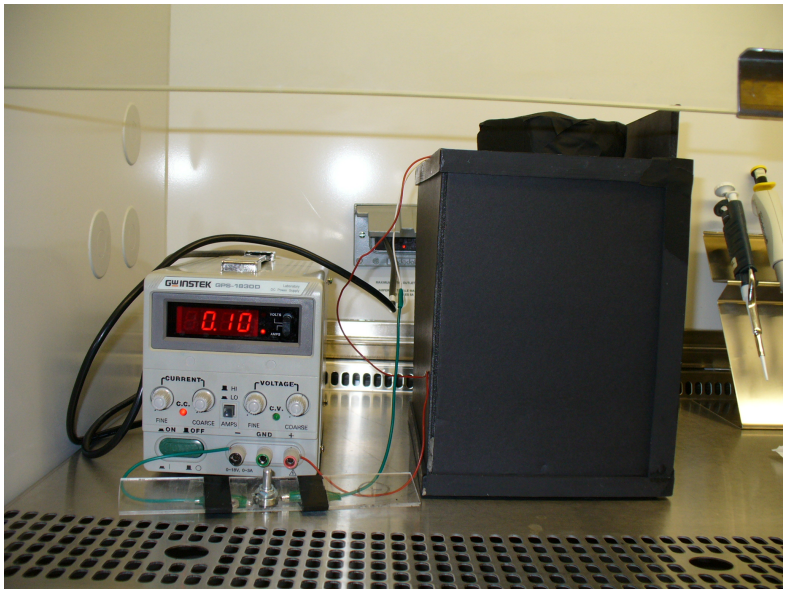

Figure 2.6: Power source (left) set at 100 mA and black box (right) to shield from high intensity LED light sterilized with 70 % EtOH in laminar flow hood.

2.5 Gel Characterization

To model the mechanical aspects of glial scarring it is important to model the mechanical nature of the CNS. Additionally, cell survival and behavior upon encapsulation is highly dependent upon gel properties including porosity and swelling. Microglia and astrocytes are mixed in with the precursor solution prior to crosslinking to achieve photoencapsulation that is explored in Chapter 4. In order to further understand the relationship between the HAMA scaffold and mixed glial cell population it is important to look at gel characteristics. Swelling, moduli of elasticity and pore size are important hydrogel characteristics that play a role in cell viability, motility and proliferation [72, 76, 100-102].

2.5.1 Gel Modulus

One of the overarching objectives of this study was to develop an in vitro cell scaffold capable of modeling the mechanical properties of the CNS. Cells are known to interact with their environment mechanically through mechanotransduction, whereby mechanical signals are converted to chemical stimuli. Mechanotrasnduction is linked to both cell proliferation and migration. As a result, gel stiffness could not only effect how astrocytes and microglia behave in the HAMA matrix, but also glial scarring. Mechanical incompatibility between the CNS and electrode has been proposed as a contributing factor to glial scarring. To test this aspect of electrode design in the 3D in vitro culture model, it is important that the HAMA gel stiffness matches the stiffness of CNS tissue. Many mechanical studies have been performed to determine the viscoelastic properties of CNS tissue. In general, shear modulus data shows a viscoelastic region for brain tissue below 0.5% strain with increasing storage and loss modulus as frequency increases [103]. Fewer studies exist of spinal cord modulus, most of which are in tension and cannot be compared to shear modulus data [104]. The most commonly reported modulus values for brain are on the order of a few kPa, though some studies have reported lower shear modulus values between 0.1 to 1 kPa [105-109]. This large range is likely due to the non-homogenous nature of CNS tissue, differences between CNS regions (white matter vs grey matter) and testing parameters [79, 103, 107]. Although there is still a certain degree of contention regarding the true shear modulus of brain and spinal cord tissue, these mechanical properties are very

important when setting up a 3D in vitro model. Modulus has not only been linked to cell proliferation and migration, but is also potentially a major factor in how a neural interfacing electrode interacts with the CNS.

A scaffold with tunable mechanical properties would allow modeling of glial scarring in different regions of the CNS (brain vs spinal cord). In literature, there are many methods reported for altering the mechanical properties of hydrogels including modifying degree of methacrylation, macromer blends and intensity of LED light [87, 88, 94, 100]. One of the most straightforward methods is modifying the macromer weight percent [72]. As the macromer weight fraction of the gel increases, so does its shear or compressive modulus. Most studies show tunable gel properties between 2-10 kPa [72, 83, 85, 88]. However, the study with the most comparable testing parameters and material reported shear modulus values between 50-35,000 Pa for macromer weight fractions between 1.5 and 8.0 wt% [83]. To establish how stiffness varies with macromer weight fraction, loss and storage modulus of the HAMA gel at weight fractions between 0.5-1.5 wt% were analyzed with parallel plate rheometry. A sample of adult rat brain was also tested to see how HAMA gel stiffness compared to whole CNS tissue tested under the same conditions.

HAMA gel dynamic modulus at macromer weight fractions between 0.5 and 1.5 wt% was investigated using a Physica MCR 301 Rheometer (Anton Paar GmbH, Ashland, VA)[1]. The CNS tissue sample was taken from a female adult Sprague-Dawely rat and used no longer than 1.5 hours postmortem (tissue used 4 hours postmortem has been shown to effect mechanical properties). The brain was sliced to a thickness of ~1.6 mm using a guide and razor blade then stored in brain buffer solution on ice until testing (within one hour of slicing). Multiple sections from one rat brain were tested and these values were averaged All samples were measured using 25 mm parallel plate geometry with a gap of 1 mm between the plates. Amplitude sweeps were performed for each HAMA wt% at 1 Hz between 0.05 and 100 % strain and 37 °C (Figure 2.7).

[1] Special thanks is given to Dr. Mirko Betti and Zied Khiari from the Department of Agricultural, Food and Nutritional Science at the University of Alberta for the training and use of the Rheometer.

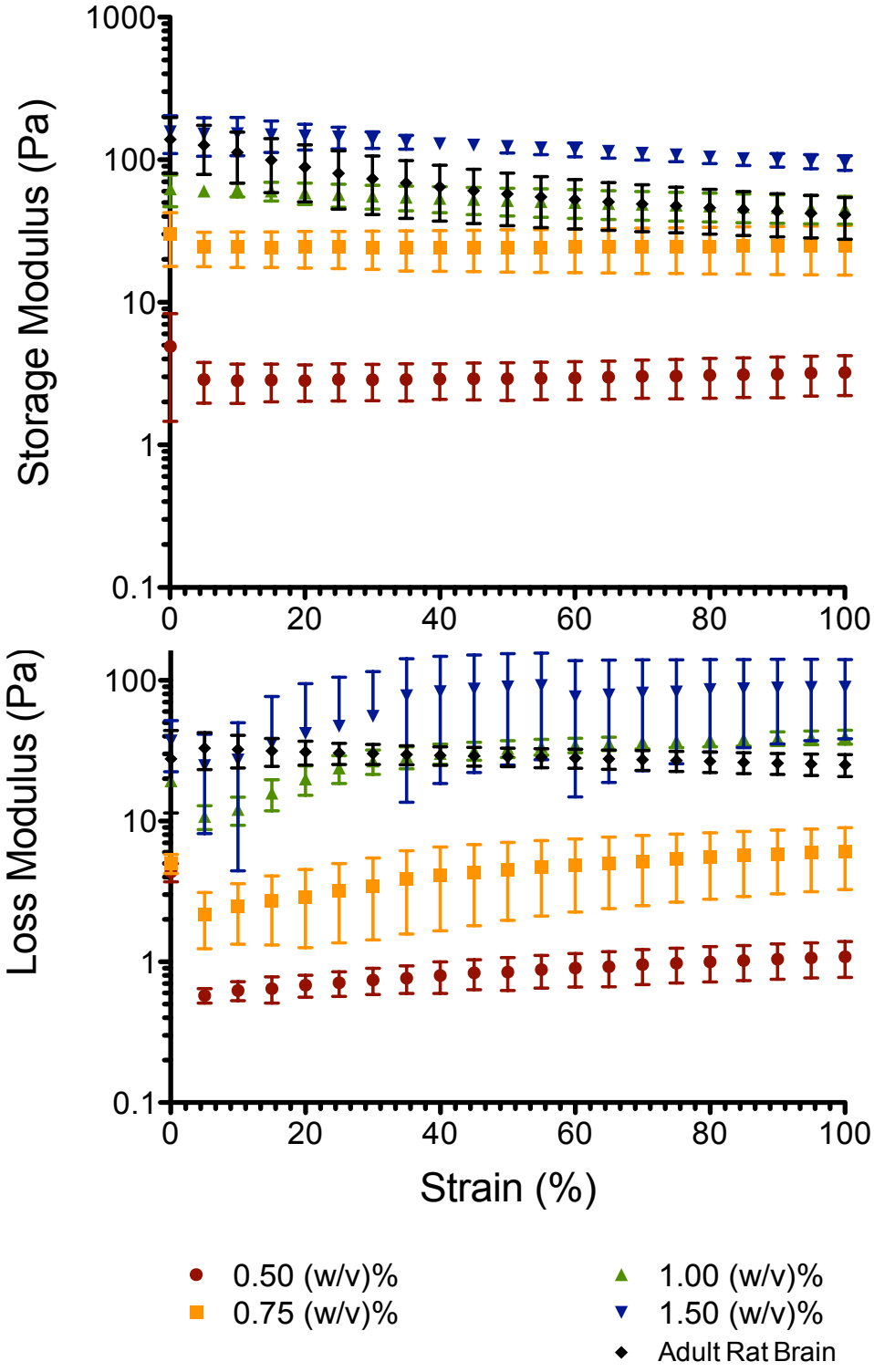

Figure 2.5: Amplitude sweeps between 0.05 – 100 % strain at a frequency of 1 Hz for HAMA gels with weight percentages between 0.5 and 1.5 and adult rat brain at 37 °C. N=4, SD.

The linear nature of the storage modulus during the amplitude sweep indicated that all samples were viscoelastic within the range of 0.05 to 100 % strain. Data from the amplitude sweep tests was used to determine average modulus values at 1 Hz.

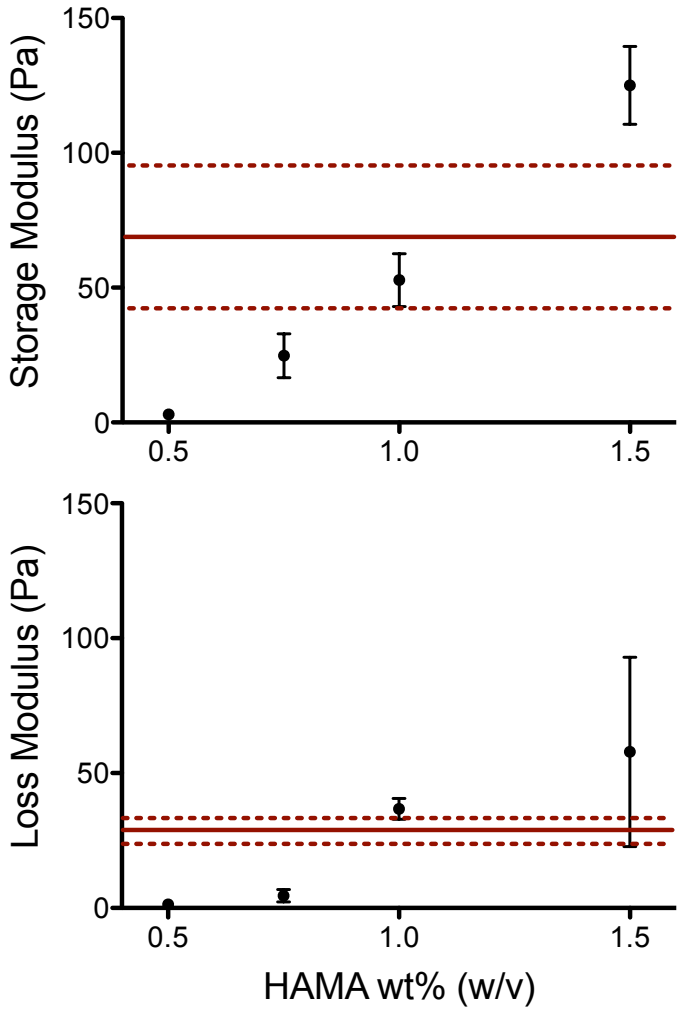

*Figure 2.6: Average storage and loss modulus values for each HAMA macromer weight percentage and adult rat brain (shown in **red**) as calculated from amplitude sweep curves. N=4, SD.*

These averages indicated a trend for increasing elastic modulus with increasing wt% between the range of ~3 to ~130 Pa (Figure 2.6). Average loss modulus values followed a similar trend although there was a large amount of variation in the 1.5 wt% sample. Tested adult rat brain samples were within the range of moduli produced by altering macromer weight fraction of the gel indicating that this technique may be used to tune gel properties and model different regions of the CNS. The large error bar seen for adult rat brain storage modulus may be due to the

inhomogenous nature of brain tissue. Transvere (coronal) sections were taken from whole brain tissue and would likely encompass many brain regions, resulting in greater variation between samples.

After amplitude sweeps of each sample were complete, a frequency sweep was run on the same sample. This was possible because amplitude sweeps were not performed outside the viscoelastic range for the HAMA gels so the gels remained intact. These measurements were performed at constant strain of 5 % in the frequency range of 0.01 to 100 Hz at 37 °C (Figure 2.7).

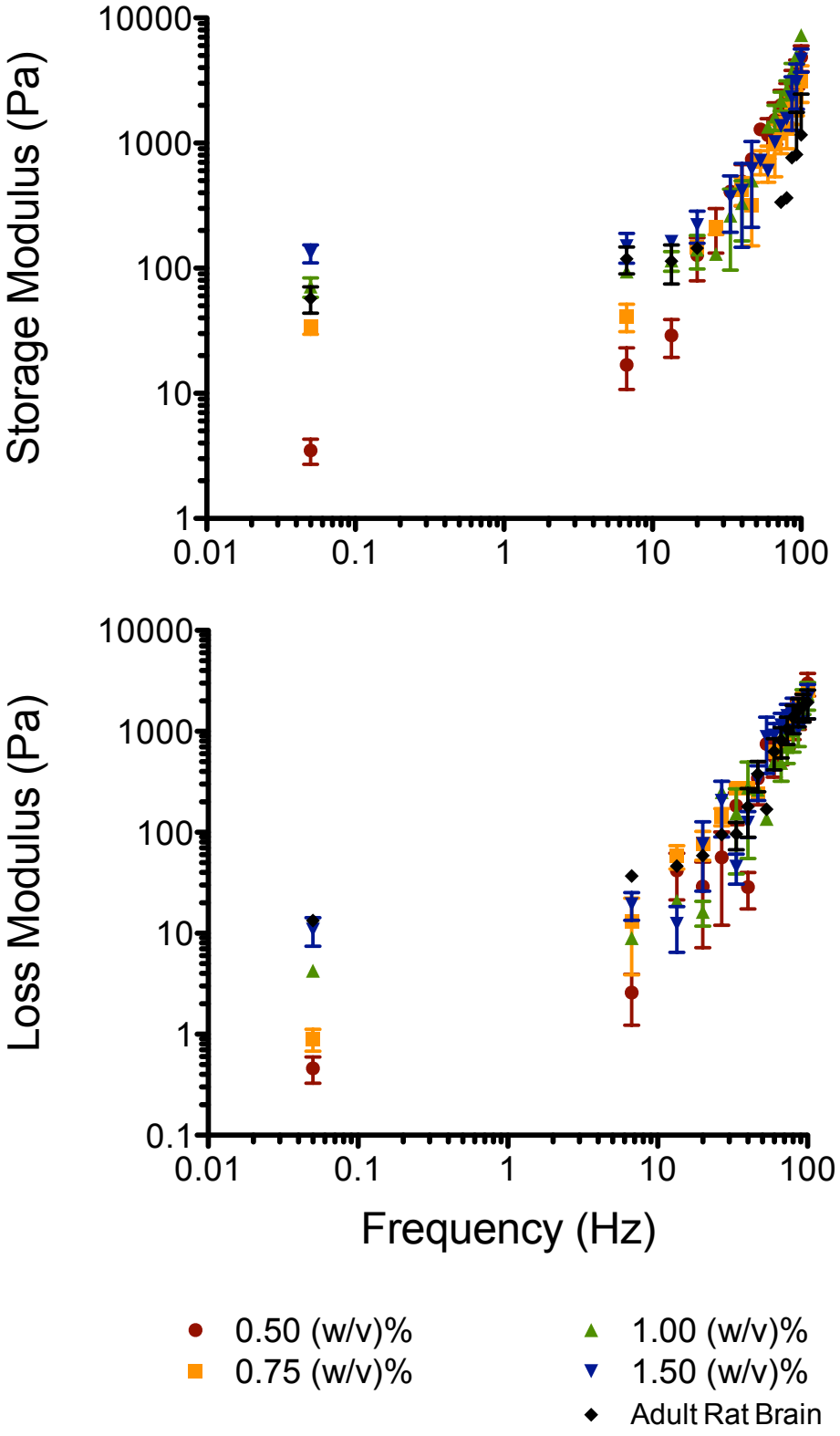

Figure 2.7: Frequency sweep of HAMA gels (0.5 to 1.5 wt%) and adult rat brain at 5 % strain between 0.01 and 100 Hz at 37 °C. N=4, SD.

At low frequencies, different macromer weight percentages had distinct moduli following a trend similar to that seen during the amplitude sweep. As frequency increased, storage modulus increased and converged to ~ 4 to 5 kPa. Loss modulus followed a similar trend with more variability. The adult rat brain samples also appeared to converge at a higher modulus values as frequency increased. This demonstrates the viscoelastic nature of CNS tissue and the ability of HAMA gels to model this trend.

2.5.2 Gel Porosity

Scaffold porosity modulates diffusion, cell attachment and migration. Pores in the network must be large enough that cells can fit within them, but not so large that they begin to interfere with the cells' ability to adhere and move through the network (microglia and astrocyte cell bodies 20-50 μm). Gels must also be porous to allow diffusion of nutrients through the network. Besides cell compatibility, gel porosity is linked to many other mechanical properties including stiffness, equilibrium swelling ratio (q) and crosslinking density [85, 87, 100, 110]. For example, an increase in gel stiffness is related to a decrease in pore size. An increase in gel stiffness as demonstrated in Section 2.3.1 would imply a decrease in pore size with increasing macromer weight fraction.

To investigate the structure of gels at varying weight percent hyaluronic acid, Cryo scanning electron microscopy (SEM) was used. Samples with macromer concentrations between 0.5 and 1.5 wt% were prepared on coverslips and left overnight in ddH_2O. The gels were immersed in liquid nitrogen to encourage amorphous water crystal growth. Gels were then fractured under liquid nitrogen to produce a clean surface and mounted onto the SEM stage. Samples were then transferred to the cooled SEM chamber for imaging on a Zeiss NV40 Dual beam FIB/SEM microscope (Figure 2.8)[2].

[2] Special thanks are given to Martin Kupsta at NRC-NINT for preparation and imaging of hydrogels for SEM analysis.

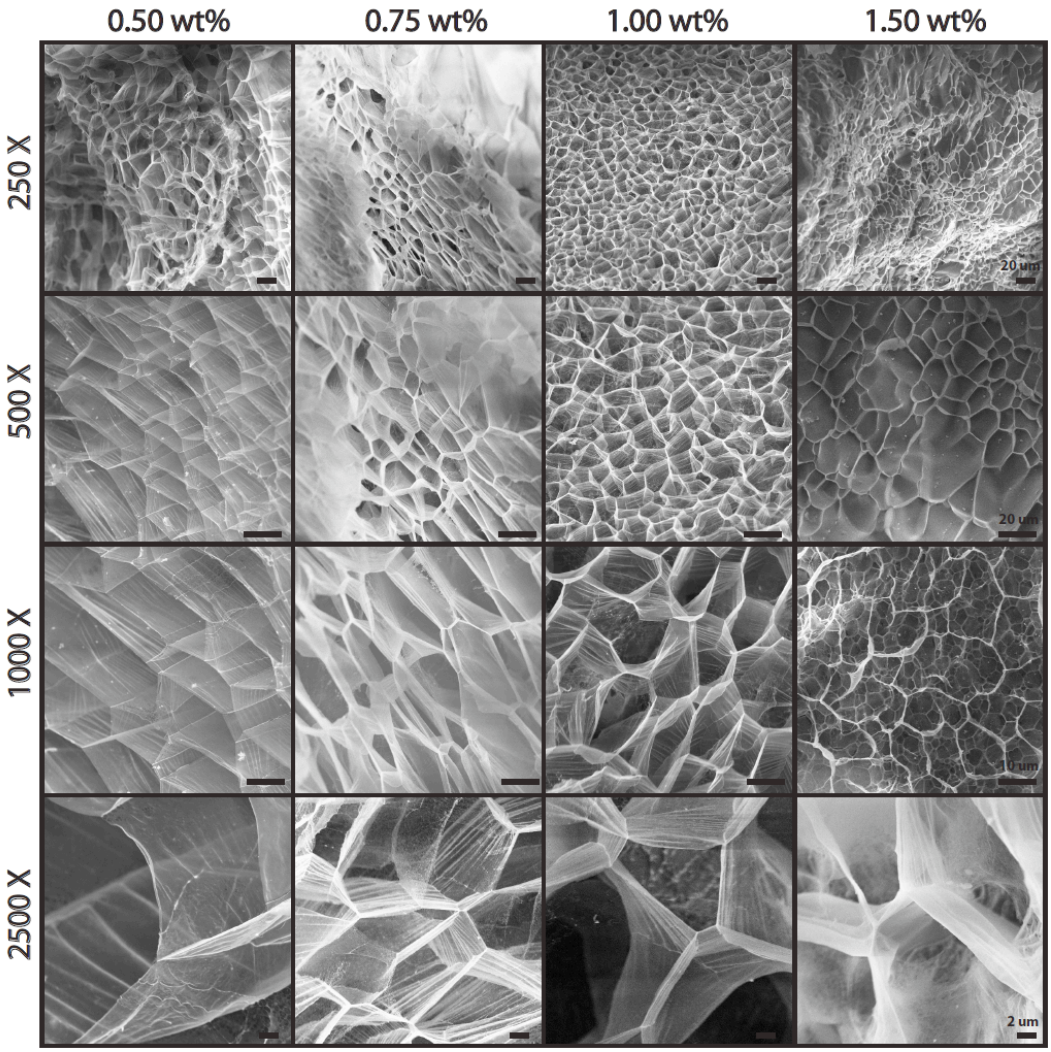

Figure 2.8: CryoSEM images of HAMA hydrogels with varying macromer weight fractions between 0.5 to 1.5 wt%

All macromer weight fractions tested (0.5 to 1.5 wt%) were porous. The lowest macromer fraction, 0.5 wt%, appeared to have elongated pores while the highest macromer weight fraction, 1.5 wt%, did not appear to have any pore direction. Although all weight fractions were porous, no obvious difference in pore size was observed between the different samples. Instead, wall thickness appeared to change between samples. 0.5 wt% HAMA gel walls were almost electron transparent while the 1.5 wt% sample was much thicker and more defined.

Because no significant difference in porosity could be determined from CryoSEM images, another gel property linked to pore size was investigated. Equilibrium

swelling ratio (q) is defined as the ratio of the wet gel weight (W_{wet}) to the dry gel weight (W_{dry}) as shown in Equation 2.3 [82, 98, 100]. It is a measure of the total water adsorption of a gel. A gel with tighter crosslinks, increased stiffness and decreasing porosity will exhibit greater retractive forces, resulting in less water absorption and a lower q value [100].

$$q = \frac{W_{wet}}{W_{dry}} \qquad [2.3]$$

After 24 hours in PBS solution at 37 °C, the gel was weighed (W_{wet}). Equilibrium swelling ratio (q) was then calculated using the dry weight of the gel used (W_{dry}) with Equation 2.3. Results showed a decreasing trend for q with increasing HAMA macromer wt% (Figure 2.8). This trend indicates a decrease in pore size as macromer weight fraction increases that may not be obvious from SEM images.

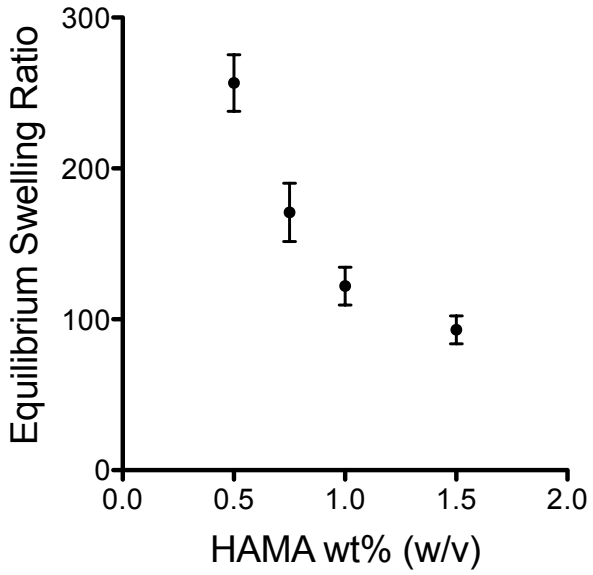

Figure 2.8: Equilibrium swelling ratio (q) of HAMA hydrogels at varying macromer weight percentages taken after 24 hours in PBS at 37 °C. N=3, SD.

2.5.3 Gel Swelling and Stability

Hydrogels are materials that imbibe large quantities of water (>100 % of their own weight) without dissolution [111]. Water retention and swelling in these gels are highly dependent upon degree of crosslinking, pH and temperature [111, 112]. For example, an increase in crosslinking density results in an decrease in equilibrium

water content and an increase in mechanical properties such as compressive modulus [100, 113]. As shown previously, increasing HAMA macromer wt% resulted in increased shear modulus and a decrease in equilibrium swelling ratio (q). When cells are encapsulated, any changes in dimension (until equilibrium is reached) are important to consider as they may affect cell viability and behavior. Previously, both contraction and swelling have been observed during cell encapsulation *in vitro* [94, 113]. As culture temperature and pH are highly regulated, swelling is most likely a result of changing macromer weight fraction. To investigate the effects of changing macromer weight fraction on swelling behavior equilibrium swelling percent (q') was studied.

Equilibrium swelling percent (q') was defined as the change in gel weight after 24 hours divided by the initial gel weight immediately after photopolymerization (Equation 2.4). This represents any change in gel swelling after encapsulation.

$$q' = \frac{W_{equil.} - W_{init.}}{W_{init.}} \qquad [2.4]$$

Immediately after photopolymerization, gels were weighed (W_{init}), the gel was then placed in PBS overnight at 37 °C and weighed again ($W_{equil.}$). Results indicated that gel swelling did take place after 24 hours in PBS, though there was no significant difference between HAMA macromer weight percentages (Figure 2.9).

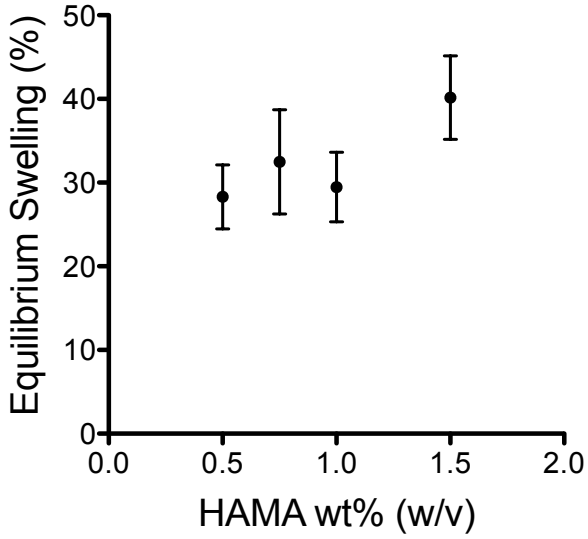

Figure 2.9: Equilibrium swelling percent (q') after 24 hours at various macromer weight percentages. N=3, SD.

As all gels imbibed water after 24 hours, cells do experience some change in gel structure after encapsulation. However, swelling was consistent regardless of macromer concentration so any changes should occur in all gels within the range tested.

2.6 Summary

In this chapter, the synthesis and characterization of an HA based hydrogel for cell culture was investigated. Hyaluronic acid was successfully modified with methacrylate groups. This reaction was upscaled from a yield of ~ 53 mg to ~ 420 mg without significantly changing the degree of modification or percent yield. The HAMA macromer was then photocrosslinked under high intensity LED light for 2 min (~520 nm, 60 mW) using a 3 component photoinitiator system (0.1 % (w/v) TEA, 0.1% (w/v) NVP and 0.01 mM EY) to produce an insoluble and porous hydrogel. Further studies were undertaken to characterize the mechanical and structural properties of the gel. Rheometry results from an amplitude sweep with a constant frequency of 1 Hz indicated a significant trend between increasing HAMA

macromer weight percent and storage modulus from~3 at 0.5 wt% to ~130 Pa at 1.5wt%. Adult rat brain tested under identical conditions had storage modulus values of ~ 80 Pa. This is within the range of HAMA tunable mechanical properties, suggesting HAMA is a suitable material for mechanically modeling regions of the CNS. Equilibrium swelling ration indicated a decrease in pore size with increasing macromer weight fraction though no significant decrease in porosity was observed with CryoSEM. Though CryoSEM did not indicate decreasing pore size, it did reveal an obvious increase in wall thickness with increasing macromer weight fraction. Finally, HAMA gels did swell after crosslinking, but there was no significant difference in the degree of swelling between samples. This suggests that all gels would apply similar forces to cells upon encapsulation. Based on the expected cytocompatibility, tunable mechanical properties, and porous nature of HAMA gels, they are expected to be strong candidates for 3D cell culture. The integration of cells within these gels will be examined in Chapter 4. To establish a basis for comparison, the culture of cells in 2D was first examined in Chapter 3.

Chapter 3.0
PRELIMINARY 2D CULTURE

3.0 Introduction to 2D Cell Culture

Chapter 3 investigates the mixed population of astrocytes and microglia to be used for 3D cell culture. The goals of this chapter are two-fold. The first goal is to isolate the cells of interest (microglia and astrocytes) from whole tissue. For this research, primary cells isolated from whole CNS tissue, not immortalized cell lines, are used. Isolating cells from primary tissue is preferable to using cell lines because the cells are more likely to maintain the majority of their receptors and functions. Microglia and astrocytes must be isolated because they are not the only cells in the CNS. CNS tissue also contains neurons, blood cells, epyndymal cells and oligodendrocytes. Both the brain and spinal cord regions contain glial cells and both regions of interest for electrode implantation, therefore both were considered in Section 3.1 as sources for mixed glial cultures. It is important to obtain a high cell yield and viability after isolation to ensure enough cells are available for 3D cell encapsulation and high-throughput analysis (Chapter 4). The second goal of this chapter is to characterize the mixed glial cultures after isolation from whole CNS tissue. Both cell morphology and behavior were considered during cell characterization. Cell morphology and behavior are particularly important when monitoring the progression of glial scarring, as changes are commonly used as indicators for activation state and to quantify the degree of glial scarring. Microglia are regularly classified as 'activated' when they appear amoeboid and astrocytes characteristically upregulate GFAP expression in their reactive state. Therefore, it is important to consider how the isolation process may alter cell morphology and behavior. Comparing isolated cell morphology and the foreign body response in 2D to reported *in vivo* behavior can provide insight into changes that may occur due to isolation. Cells in 3D culture are also reported to express different cell surface receptors and respond to stimuli in a different manner than they do in 2D. To evaluate any differences, characterization and cell behavior in 2D will be compared with that observed in 3D (Chapter 4). The techniques and procedures standardized in this chapter will also act as a baseline to be modified for 3D culture in Chapter 4.

3.1 Astrocyte and Microglia Isolation

The isolation of cells from primary tissue is a common technique used regularly for *in vitro* analysis referred to in literature as primary culture. By selecting the region of tissue removed, isolation technique as well as growth factors and nutrients to be supplied after isolation, cell types of interest for culture may be chosen. The cell types of interest in this study are astrocytes and microglia, which may be isolated from CNS tissue (both brain and spinal cord) using a trypsin dissociation technique. As electrodes are being developed for use in both the brain and spinal cord regions, it was of interest to consider cells from both the spinal cord and brain for isolation. To determine which CNS regions (brain or spinal cord) was most suitable for isolation, cell viability and yield were considered.

The isolation process has many steps. As outlined in Figure 3.1, mixed glial cultures were prepared from whole brain and spinal cord of day 1 rat pups through a series of steps including tissue extraction, tissue decomposition, suspension in new media, viability analysis and cell culture. Each of these steps was standardized to establish a method and the source tissue (brain or spinal cord) for the isolation of astrocytes and microglia from primary tissue to be used later for encapsulation in Chapter 4.

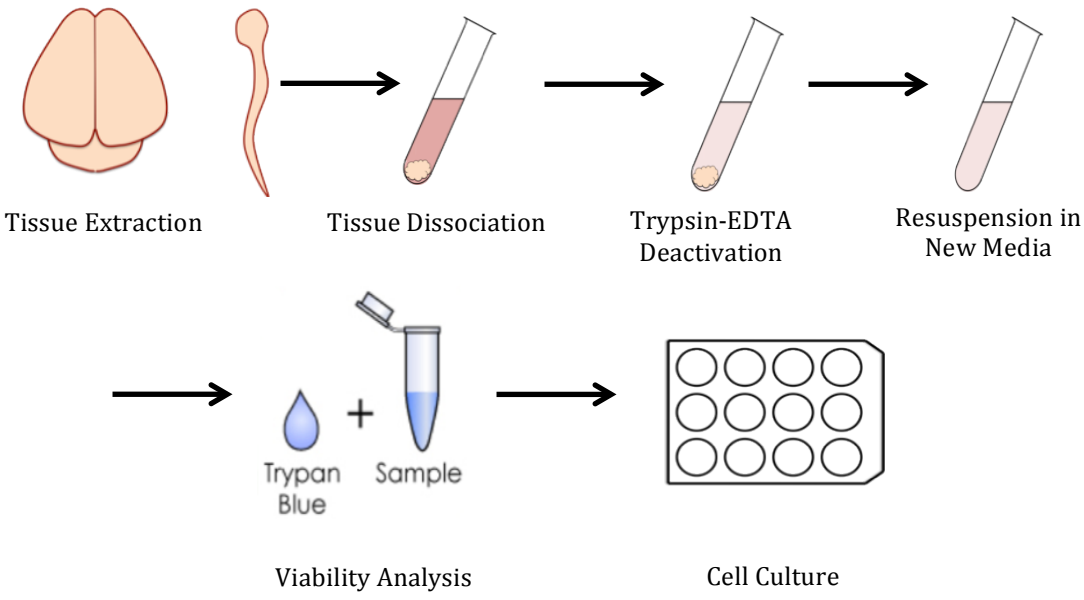

Figure 3.1: Outline for isolation of mixed glial cells from the CNS of day1 Sprague-Dawely rat pups.

3.1.1 Tissue extraction and enzymatic dissociation

Mixed glial cultures (astrocytes and microglia) were obtained from postnatal day one Sprague-Dawley rat whole brain and spinal cord. Rats were euthanized by decapitation and the brain and spinal cord were exposed. Whole brain and spinal cord tissue were removed using a metal spatula and placed into separate solutions of Hank's balanced salt solution (HBSS, Thermo Scientific) with 200 units/mL penicillin and 200 µg/mL streptomycin (PS, Gibco). At this point it, was apparent that spinal cords tissue was much smaller than brain tissue, but other features that may affect the relative cell types were difficult to distinguish by eye (white matter versus grey matter ect.). Meninges and surface vasculature were then gently removed from both the brain and spinal cord tissue separately using forceps. The brain was minced into ~ 1 mm^3 pieces using a scalpel. Minced whole brains were dissociated by enzymatic digestion in 0.25 % Trypsin and 1 mM Ethylenediaminetetraacetic acid (Trypsin-EDTA, Gibco) at 37 °C. The solution was then further dissociated into a single cell suspension via trituration. Cells were cultured on glass coverslips in 12 well tissue culture treated plates (Costar) coated with 2 µg/mL Poly-L-Lysine solution (PLL, Sigma) at 37 °C in a 5% CO_2 incubator. It was obvious upon dissection that spinal cord tissue volume was significantly less than brain tissue volume. Therefore, each brain was plated onto one 12 well plate while spinal cord tissue was pooled (4 spinal cords per one 12 well plate). Media was changed 2-3 times weekly with Dullbecco's Modified Eagle's Medium and Ham's nutrient mixture F-12 in a 1:1 ratio (DMEM/F12, Thermo Scientific) containing 10 % fetal bovine serum (FBS, Gibco) and PS.

3.1.2 Viability and Cell Yield Analysis

After trituration and before cell plating, cell viability and yield were assessed for both the brain and spinal cord isolations. To determine what percentage of cells remained viable, cells suspended in DMEM/F12+FBS+PS media were counted using a Trypan Blue exclusion assay. This assay uses Trypan Blue, a dye excluded from cells with intact cell membranes but not those cells with compromised cell membranes. Under light microscopy, dead cells appeared dark blue and live cells appeared bright white. This simple technique allows live and dead cells in

suspension to be quickly counted. To perform the assay, a small sample of suspended cells was pipetted into a microcentrifuge tube and then mixed with a known ratio of 0.5 wt% Trypan Blue (1:1 or 1:2 cell suspension to Trypan Blue by volume) called the dilution factor (DF) used later in the calculation of cell density (CD). Cells were mixed with Trypan Blue immediately before counting, as Trypan Blue is known to cause cell toxicity. A small amount of this solution was then pipetted into a Hemocytometer to count the average number of cells suspended in a specific volume. Cells on the upper and right lines were not counted to avoid counting cells twice (Figure 3.2).

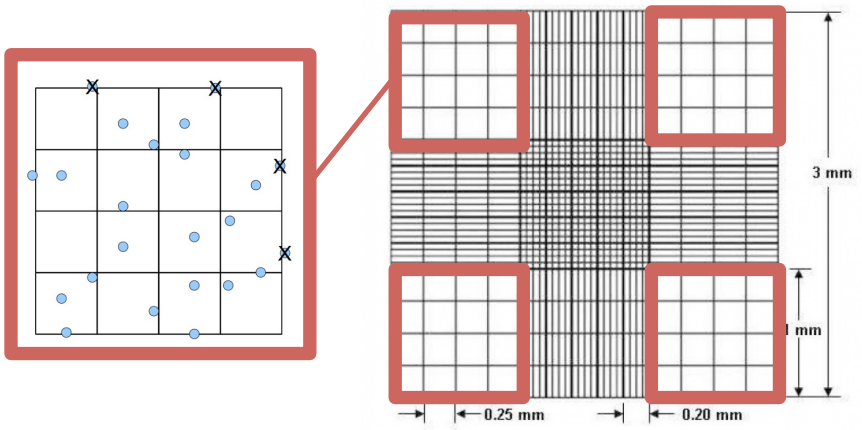

Figure 3.2: Depiction of Hemocytometer grid. Regions used for cell counting are outlined in red squares and represents 100nL volume. One red square is expanded to show example cell counts. The x's represent cells that would not be counted because they lay on the top and right lines.

All four large squares, outlined with red in Figure 3.2, were counted and averaged to determine the average live cell count and total cell count. These values were then used to determine CD of the cell suspension (Equation 3.1) and cell viability (Equation 3.2) and values are shown in Figure 3.3.

$$CD_{initial} = Average\ Live\ Cell\ Count \cdot DF \cdot 10^4 \quad [3.1]$$

$$\%\ Cell\ Viability = \frac{Live\ Cell\ Count}{Total\ Cell\ Count} \cdot 100 \quad [3.2]$$

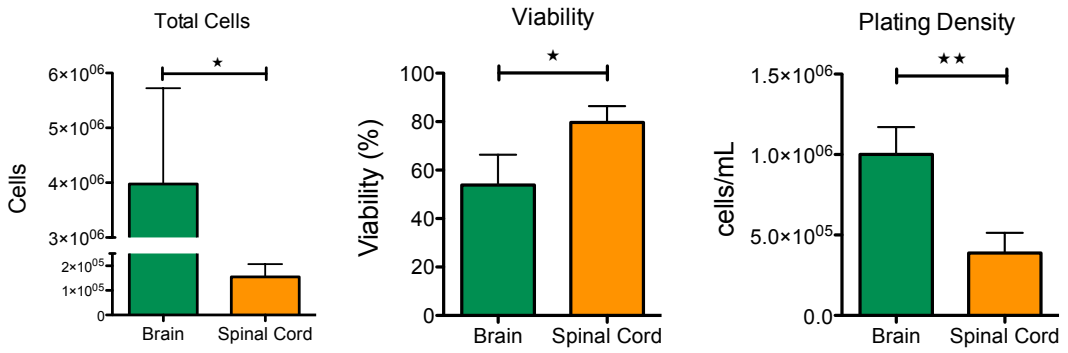

Figure 3.3:Total cells, initial viability and plating density determined via Trypan Blue exclusion assay immediately prior to cell plating. N=3, students t-test, SD, □□P<0.001, □ P<0.05 .

When normalized to the number of animals, brain tissues had significantly higher cell yield than that of spinal cord tissues. The average number of total cells obtained per spinal cord was $1.55x10^5 \pm 3.01x10^4$ cells. In comparison, the average number of total cells obtained per brain was $3.98x10^6 \pm 8.73x10^5$ cells, almost 26 times greater than the number isolated from spinal cord (Figure 2.3).

Seeding density was also lower in spinal cord cultures even after pooling spinal cord cells ($3.88x10^5 \pm 7.23x10^4$ cells/mL vs $1.00x10^6 \pm 8.52x10^4$ cells/mL), reflecting the smaller tissue volume observed upon extraction. In contrast to the increased yield, spinal cord cultures had higher initial cell viability when compared to brain cultures. Spinal cord viability was determined to be 79.7 ± 3.9 % and brain viability was 53.8 ± 6.2 %.

3.2 Characterization of Microglia and Astrocytes in 2D

After cell isolation, it was important to characterize microglia and astrocytes to ensure these cells were indeed isolated and assess cell morphology and behavior. Because the activation state and progression of glial scarring are often determined by cell morphology and increasing cell density at the electrode, it is important to determine if cell morphology and behavior are effected by isolation. To do this, both cell morphology and response to a foreign body (microelectrode) were evaluated in mixed glial cultures.

3.2.1 Morphology of Isolated Microglia and Astrocytes

Phase contrast optical microscopy provides limited information regarding the morphology of isolated brain and spinal cord cell cultures. Although it is possible to determine general health of the cells with phase contrast microscopy, it is very difficult to verify which cell types are present and which morphology they are presenting. In a normal, uninjured brain, both microglia and astrocytes are in their 'normal' or 'ramified' states. Microglia in their ramified state appear with many fine processes, while astrocytes take on a star-like appearance [15, 114]. These cells can become activated when exposed to stimulating factors or changes in the local environment [114]. Under stress, astrocytes also transition from a resting into a reactive phenotype. This transition is characterized by upregulated matrix production (including glial fibrillary acidic protein (GFAP) production), hypertrophy, and increased migration and proliferation [15]. In order to verify the presence of microglia and astrocytes in the culture (thus determining is cell isolation was successful) and characterize cell morphology further labeling was necessary.

Cell labeling via immunofluorescence is a common method for identifying cells both *in vivo* and in *in vitro* mixed cultures. The process of immunofluorescence labels specific proteins or peptides in a cell using antigens. Microglia are known to express a novel calcium binding protein, Iba1, which has not been found in other cells present in the CNS [115-117] and astrocytes are commonly characterized by labeling a likewise specific protein, GFAP [15, 115, 117]. Immunofluorescence is often used to identify microglia and astrocytes as well as determine their state of activation in response to a foreign body.

Cells from both brain and spinal cord cultures were first fixed with 10 % formalin for 20 min. at room temperature. After fixing, the cells were washed 3 times with PBS and incubated in blocking buffer containing PBS, 0.1 % Triton X-100 and 10 % normal horse serum (NHS) to permeabilize the cell phospholipid bilayer. Cells were washed three times with PBS and both primary antibodies (anti-mouse GFAP, Sigma and anti-rabbit Iba1, Wako) diluted 1:1000 in PBS were applied. Cells were then incubated overnight at 4 °C with gentle shaking. The next day, after primary

antibodies were applied, cells were washed three times with PBS and the secondary antibodies, Dylight 594 (1:200, Fisher) and Dylight 488 (1:200, Life Technologies) were added. The cells were incubated at room temperature in the presence of the secondary antibody for 1 hr on a shaker. The secondary antibodies were then aspirated and the cells were washed three times with PBS. The cells were then mounted on glass slides using Fluoromount-G. Negative were performed with wells incubated in the presence of secondary antibodies but not primary antibodies to confirm that no non-specific labeling occurred. Cells were imaged with a Olympus BX60 fluorescent microscope. Microglia (Iba1, red) and astrocytes (GFAP, green) were identified in both mixed brain and spinal cord cultures from day 1 Sprague-Dawely rat pups (Figure 3.4).

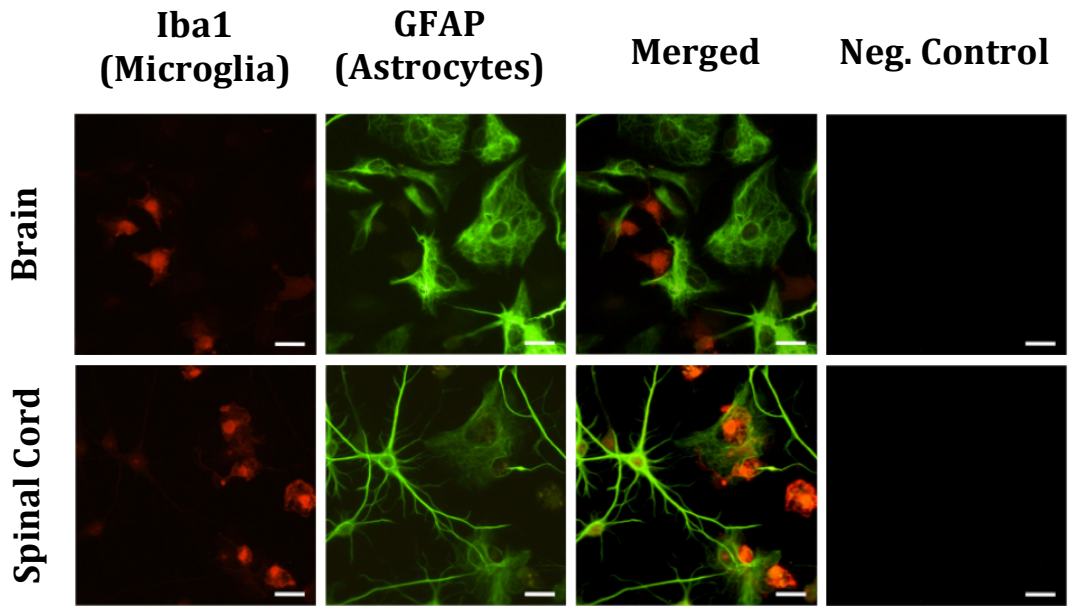

*Figure 3.4: One week old brain and spinal cord cells prepared on coverslips and mounted on slides with labeling for Iba1 (**red**) and GFAP (**green**). Scale bar 30 µm.*

Microglia (Iba 1, red) appeared to have bright cell bodies with faint processes, making it difficult to identify fine processes. The bright appearance of microglia cell bodies is likely because the Iba1 antigen is expressed in the cytoplasm and may not be as easily identified in cell processes. Although the Iba1 antigen is widely used to identify microglia in both animal and human specimens, it is known to be expressed in both microglia and macrophages [114]. As a result, it is impossible to differentiate between microglia and macrophages based purely on Iba1 labeling. This has lead to

much debate regarding the positive identification of microglia versus macrophages. However, it is unlikely that the cells labeled here are macrophages because the meninges and any remaining blood products were carefully removed during the isolation process. Iba1 is also expressed in microglia independent of microglia activation state (activated or ramified), and though it is upregulated during activation can not be used alone as an indicator of activation [114]. Instead, activation state was determined from cell morphology. In both cultures, microglia appeared to have a circular morphology indicating an activated state. Although no stimulating factors were added to the cultures, the process of isolating the cells from whole brain tissue did result in a change of the local environment, which may lead to the cells taking on an activated morphology. Previous studies have reported microglia assuming an activated morphology simply from being cultured in an *in vitro* environment and in the presence of soluble factors in culture media (FBS) [114]. This may explain the activated appearance of microglia in Figure 2.4. It should be noted that morphological changes are not always indicative of cell function and many studies have shown microglial cells are activated *in vitro* by the addition of a noxious stimulus [114]. These observations indicate that though the phenotype of glial cells may change *in vitro,* the cells still respond to stimuli in a manner similar to that seen *in vivo*. Whether or not microglia respond to microelectrodes in a manner similar to that observed *in vivo* will be tested in Section 3.3.

Astrocytes (GFAP, green) from both brain and spinal cord isolations were identified in protoplasmic (grey matter) and fibrous (white matter) morphologies. The protoplasmic morphology was clearly distinguishable from the fibrous morphology due to the extension of long, radial processes. Brain cultures appeared to have a greater number of astrocytes with a fibrous morphology and fewer cells with a protoplasmic morphology than spinal cord isolations. GFAP is believed to help maintain cell strength and is upregulated during activation but still present in normal astrocytes [75, 114]. Other indicators of astrocyte activation include hypertrophy, increased migration and proliferation [15]. Because none of these indicators were directly measured, it's difficult to discern if the astrocytes in Figure 3.4 are resting or reactive. It is important to note that there are many other

cells in the body that express GFAP including fibroblasts, leydig cells, keratinocytes, osteocytes, chondrocytes and stellate cells in the pancreas and liver [118-121]. However, the only other cells in the CNS known to express GFAP are ependymal cells. Because ependymal cells have only been observed to express GFAP during one stage of fetal development and cell isolation of astrocytes is from day 1 rat pups, it is unlikely that ependymal cells are also being labeled in Figure 3.4.

The morphologies observed here were considered when determining activation states from morphology in the 2D electrode time course study (Section 3.3) as well as during cell integration into the HAMA matrix (Chapter 4). Due to the low seeding density obtained from spinal cord isolations and the overall similarity between spinal cord and brain mixed cultures, all further experiments were performed with only microglia and astrocytes isolated from whole brain tissue. In the future, it may be of interest to pursue the encapsulation of spinal cord glial cells.

3.2.2 Isolated Microglia and Astrocyte Reaction to a Foreign Body in 2D

After mixed glial cultures were successfully isolated from whole tissue and characterized, their ability to respond to a foreign body (electrode) was tested. This was done to ensure that isolated and cultured mixed glial cells were capable of migrating and/or proliferating at a microelectrode in a manner comparable to that seen *in vivo*. *In vivo* experiments report microglia responding first to the presence of an electrode within hours to days followed by the encapsulation of the electrode by astrocytes over the period of weeks to months. The encapsulation of the electrode is termed glial scarring and is the result of microglia and astrocytes migrating to and proliferating at the electrode. As glial scarring progresses, cell density at the electrode increases. Monitoring the increase in cell density at the electrode interface is the most common and simple way to quantify glial scarring. These experiments were performed with only neonatal brain isolations due to the low cell yield from spinal cord isolations.

Previous work has shown the progression of glial scarring to different wire coatings in 2D by monitoring the response of astrocytes and microglia in mixed glial cultures to wires [11, 65, 67]. Here, a similar protocol was followed for 2D electrode drop

experiments. Polyimide coated stainless steel wires (30 or 50 µm) were cut into ~1 cm pieces and soaked in 70 % EtOH for 30 min to ensure that they were sterile. Ethanol was then removed and wires were dried under UV light. Wires were then placed onto the 2D cultures of mixed glial cells isolated from neonatal brain tissue. After wires had settled to the bottom of the culture dish, cells were incubated at 37 °C with 5 % CO_2 and media was changed every 3-4 days.

The extent and progression of glial scarring was quantified over 14 days via cell density. DAPI (4',6-diamidino-2-phenylindole, dihydrochloride) is a blue fluorescent stain that preferentially labels double stranded deoxyribonucleic acid (dsDNA) and is commonly used in conjunction with other fluorescent staining techniques to visualize nuclei [122]. One drop of Vectashield DAPI (Vector labs) was placed in the center of the each well and a glass coverslip was placed on top. This method caused no autoflourescene of the electrode and allowed quantification of increasing cell density at the electrode interface. DAPI labeling was performed at selected time points over 14 days (Figure 3.5). The electrode was denoted with dotted white lines to indicate the electrode interface.

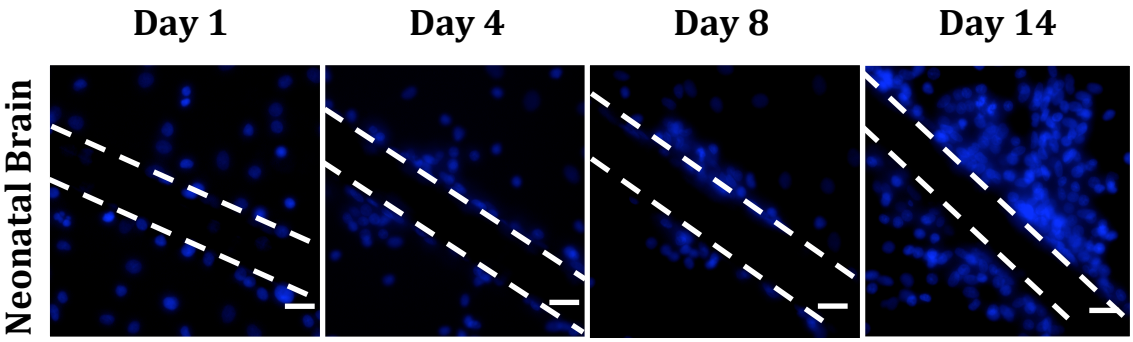

*Figure 3.5: Increasing cell density at microelectrode over 14 days indicated by cell nuclei (DAPI, **blue**). Electrode placement outlined with white dashed lines. Scale bar 20um.*

High cell density and clustering of cells made it difficult to count individual cells, so the average intensity at the electrode was calculated using ImageJ software (Figure 3.6) [123].

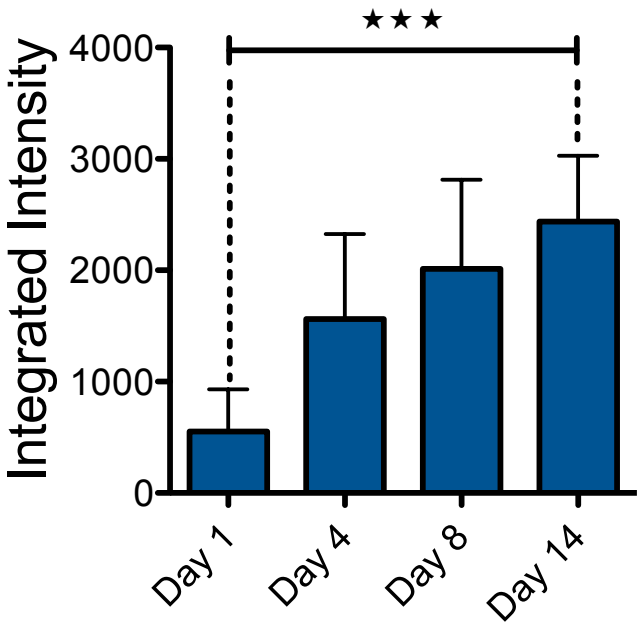

Figure 3.6: Increasing fluorescence intensity at microelectrode over 14 days. N=2, student's t test, SD, ★★★P<0.0001 .

Because DAPI selectively labels only the nuclei of cells, the integrated intensity represents both microglia and astrocytes at the interface of the electrode. An almost 5 fold increase in cell density was observed at the electrode using this technique.

Increasing cell density indicates a cellular response to the electrode over 14 days, but does not provide any information regarding the temporal response of each cell type. To determine when microglia and astrocytes respond to the electrode, cells were immunolabeled. At the desired time point, cells were fixed and labeled (GFAP and Iba1) to observe the cell specific response as previously described in section 3.2. In this case, Alexa Fluor 488 donkey anti-rabbit (Molecular Probes, 1:200) and Alexa Fluor 647 donkey anti-mouse (Molecular Probes, 1:200) were used as secondary antibodies instead of TexasRed donkey anti-rabbit and Cy-2 donkey anti-mouse respectively and cells were mounted with Fluormount-G in culture plates. It was difficult to maintain electrode stability throughout the entire time course and labeling procedures. As a result, some electrode shifting was observed during media washes and labeling.

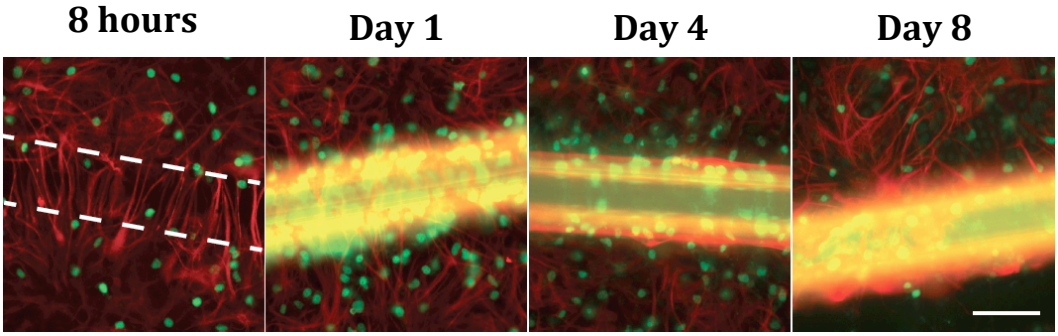

*Figure 3.7: Progression of glial scarring over 8 days in 2D mixed glial cultures. Microglia (Iba1, **green**) and astrocytes (GFAP, **red**) at the electrode. N=2. Scale bar 30 µm.*

Glial scarring over 8 days *in vitro* was similar to that reported in *in vivo* experiments. [15, 17]. At 8 hours the electrode was absent due to loss during immunolabeling (Figure 3.7). However, the space that the electrode occupied was still evident due to a lack of microglia cell bodies. It appeared that microglia had migrated out from under the dropped electrode at 8 hours, but no significant glial scarring had taken place. By day 1, microglia had migrated to and or proliferated at the electrode as indicated by an increase in Iba1 positive cells (Figure 3.7). Astrocyte processes were visibly beginning to line the electrode at day 4 and by day 8 astrocytes had started to encapsulate the electrode indicating gliosis (Figure 3.7). In some images, clusters of microglia cells and the electrode appeared yellow, likely due to distorted light during imaging.

The results of this study indicate that microglia and astrocytes from isolated mixed glial cultures demonstrate increased glial scarring over 2 weeks. These results follow closely with those previously published by Poikov et al. regarding an optimized *in vitro* model for glial scarring and *in vivo* results [11, 27, 124]. Some of the major drawbacks of such a 2D culture system including lack of vasculature and micromotions which have been linked to exacerbated glial scarring [11]. Polikov et al. suggest moving the wire during culture to mimic the motion of a microelectrode in the brain [11]. However, this was determined to be impossible in our cultures due to shifting of the electrode during culture as well as difficulty in accurately manipulating the small electrodes. It would be difficult to determine if changes in glial scarring were due to applied micromotions or artifacts of the technique. To our knowledge, this method has been used once in literature to compare electrode

coatings, but has never been used to compare other electrode characteristics such as size or geometry [67]. Later, Polikov et al. modified the glial scarring model to include a thin hydrogel coating around the electrode made from matrigel [66]. This hydrogel coating allowed cells to migrate into the scaffold surrounding the electrode and was peeled off for visualization at the desired time point [66]. Although this modification brought the glial scarring model one step closer to *in vivo* by creating a small 3D scaffold around the electrode, the electrode was still resting on top of a mixed glial 2D culture. To our knowledge, this model has also only been used to test the effect of soluble factors on glial scarring, not the effects of micromotion. In our opinion, the mechanical environment of the CNS including components of the ECM, stiffness, and 3D geometry may play a major role in the glial scarring response and the ability to model this is paramount.

3.3 Summary

Mixed glial cultures were successfully isolated from both brain and spinal cord tissue removed from day 1 rat pups. Spinal cord preparations had significantly higher seeding viability while brain had much higher seeding density. Both culture preparations were characterized to ensure that the cell types of interest, microglia and astrocytes, were present and to identify their morphology. Both neonatal brain and spinal cord cultures contained astrocytes and microglia. The morphology between glial cells in the brain and spinal cord cultures was similar. Because of the low cell yield from spinal cord preparations, further experiments were performed only with brain tissue. To investigate the cells ability to respond to a foreign body after isolation, brain cultures were then used as part of a 2D glial scarring model. The 2D electrode drop model showed progression of glial scarring similar to that of similar *in vitro* models and *in vivo* experiments over two weeks [11, 17, 65-67]. Immunolabeling indicated that microglia were the first to respond to the electrode (day 1) followed by astrocytes (day 4). However, the fine microwires shifted easily during media changes and labeling, making it impossible to test the reaction of the mixed glial 2D cultures to micromotion. The isolation and labeling techniques standardized in this chapter were combined with the photocrosslinking system

developed in Chapter 2 to produce mixed glial 3D cultures and investigate their use as a glial scarring model in Chapter 4.

Chapter 4.0

CELL-GEL INTEGRATION

4.0 Introduction to Cell-Gel Integration

Chapter 4 examines the encapsulation of isolated mixed glial cultures from Chapter 3 using the previously developed photocrosslinking system with tunable mechanical properties (Chapter 2) and the feasibility of using this gel-cell system as a 3D model for glial scarring. As discussed in Chapter 2, the HAMA photocrosslinking system must be cytocompatible. Microglia and astrocytes must remain viable before, during and after encapsulation. The first experiment performed was to ensure that viable cells could be encapsulated in the HAMA matrix. After this was demonstrated, steps were taken to optimize cell viability over 7 days by modifying seeding density. Once seeding density was optimized, microglia and astrocytes were characterized. This morphology was compared to what was observed in 2D cultures to determine any changes that may have occurred due to encapsulation. In Chapter 2, it was shown that the HAMA gel mechanical properties could be tuned by modifying macromer weight fraction to potentially model different regions of the CNS (spinal cord vs brain or white matter vs grey matter). However, modifying macromer weight fraction also altered gel structure (in particular wall thickness). To determine if increasing macromer weight fraction effected microglia and astrocytes, cell viability was monitored in various gel constructs over 7 days. The tunable properties of the gel are only beneficial if cells remain viable, therefore this experiment gives insight into the limits of the model. In addition to modeling the mechanical aspects of the CNS, the gel-cell construct must also function as a model of glial scarring. The electrode must be stable during culture without electrode shifting and microglia and astrocytes must be visualized at the electrode interface. Ideally the model will allow progression of glial scarring in response to an electrode (increased cell density at the electrode) to be monitored over many weeks. To examine this, the temporal progression of glial scarring was observed over 21 days and this data was compared to existing models. These results were used to determine the feasibility of using an HAMA photocrosslinking system to monitor glial scarring at a microwire-cell interface.

4.1 Photoencapsulation of Mixed Cultures

To create an *in vitro* model of glial scarring, it was necessary to start with a mixed glial population of astrocytes and microglia homogenously distributed throughout the HAMA gel. To achieve this, isolated glia cells were mixed with aqueous HAMA macromer then exposed to green LED light to initiate crosslinking. The isolation of mixed glial cells from whole tissue (Chapter 3) ends with the cells adhered to the bottom of 2D cell culture plates. Before these cells could be mixed with aqueous HAMA, it was first necessary to first lift the cells from the plate using trypsin. This entire process is outlined in Figure 4.1 beginning with the isolated cells on 2D culture plates and ending with the cells encapsulated in the HAMA matrix. This section describes each of the steps in the procedure to encapsulated mixed glial cells.

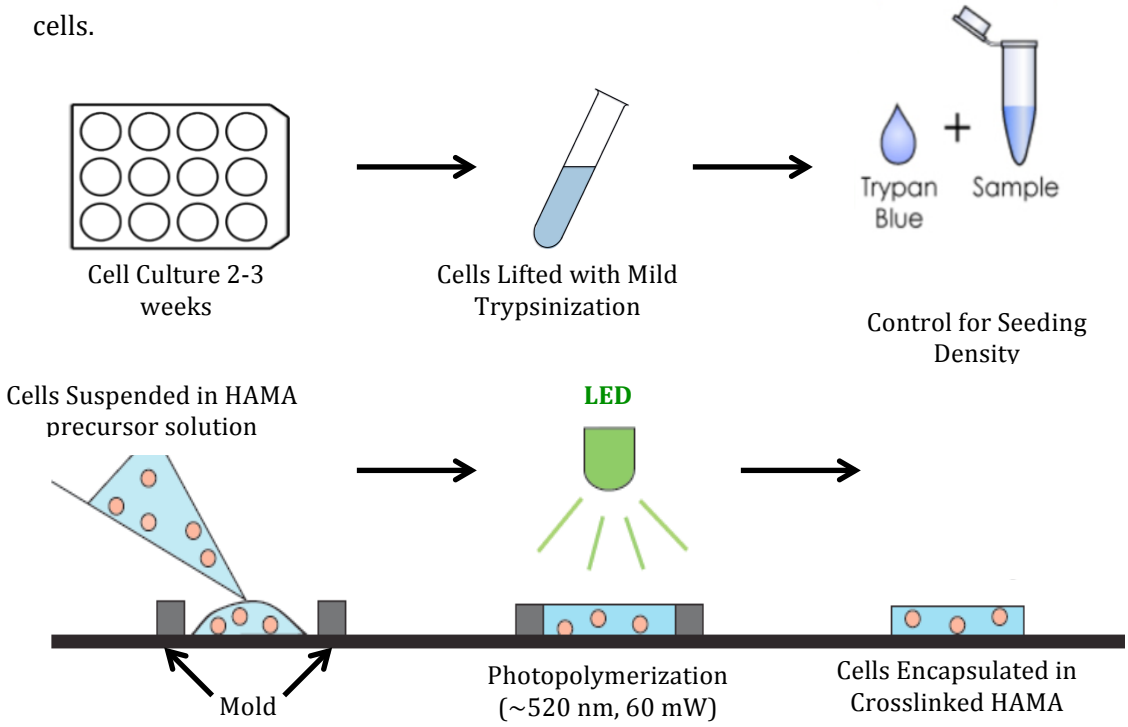

Figure 4.1: Photoencapsulation method for 3D culture of mixed glial (astrocytes and microglia) cultures.

4.1.1 Mild Trypsinization and Cell Dissociation

In order to achieve cell dispersion throughout the entire scaffold, mixed glial cells were photoencapsulated in HAMA. This process began with mixed glial cells cultured for 2-3 weeks to confluence on polystyrene culture plates as described in section 3.1. After 2-3 weeks of culture on PLL treated polystyrene plates, cells were

adherent to the bottom of the plate. To lift cells from the plate, a mild trypsinization technique was used. Although mild trypsinization has been used previously to isolate microglia, the lifted cells are not often used as mixed glial cultures [125]. Because other studies have not looked at phenotype or viability of this cell population, it was necessary to characterize the cells before using them for encapsulation.

Mild trypsinization uses a solution of 0.075 % Trypsin and 0.3 mM EDTA in DMEM/F12. This solution was obtained by mixing the Trypsin solution used for tissue dissociation (0.25 % Trypsin and 1 mM EDTA) with DMEM/F12 in a 1:3 ratio. Media was aspirated from plates and then the cells were covered with the diluted Trypsin-EDTA solution. After 15-30 min, cells lifted off the bottom of the culture plate in a film that was collected with a 1000 µL pipette.

After cells were collected, the trypsin solution was spun down to pellet cells then decanted and cells were resuspended in DMEM/F12 with 10 % FBS and 2 % PS to prevent any unnecessary damage due to prolonged Trypsin-EDTA exposure. Cells were mechanically separated through trituration in a manner similar to 2D cell culture tissue dissociation (section 3.1). To further reduce the residual Trypsin-EDTA and remove unwanted cell debris, media was decanted again and resuspended in new media. These cells were then plated again onto PLL coated cell culture plates. After one week of culture, these cells were immunolabeled following the protocol outlined in section 3.6. Both microglia and astrocytes were present (Figure 3.7).

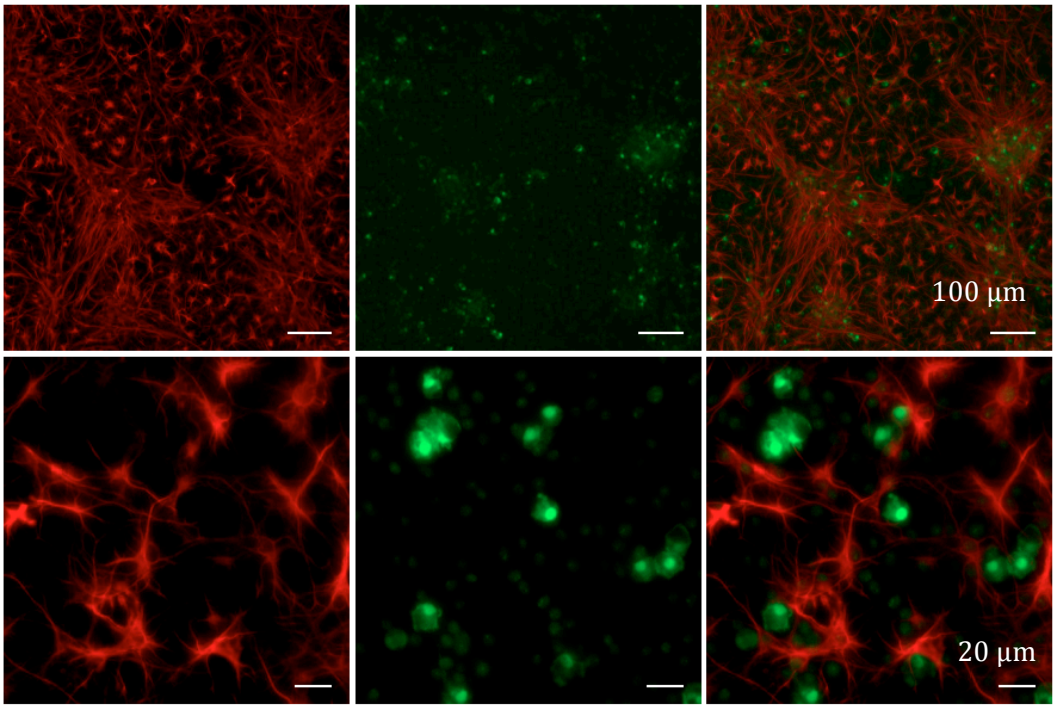

*Figure 4.2: Astrocytes (**red**, GFAP) and microglia (**green**, Iba1) from mild trypsinization protocol.*

Primarily protoplasmic astrocytes were identified, but some fibrous astrocytes were also present. Similar to previous characterization in Section 3.2.1, microglia appeared to have a circular morphology indicative of the activated microglial state. On average, more astrocytes than microglia were observed which is similar to ratios observed *in vivo* [76, 126]. Because both cell types were present in the lifted cell mixture and representative of both *in vivo* and *in vitro* cells, the mild trypsinization method was used to obtain mixed glial cultures for photoencapsulation. Culturing cells prior to encapsulation also improved cell viability and eliminated residual debris that would be present if cells were encapsulated immediately after tissue dissociation.

4.1.2 Suspension in HAMA

To homogeneously encapsulate cells in a gel, the cells were suspended in aqueous 0.5 wt% HAMA. To ensure full hydration of the HAMA macromer, gel solutions were prepared at least 24 hours before encapsulation (Chapter 2) and then mixed with the desired concentration of cells. To determine the volume of cell suspension required to obtain the desired cell density, a Trypan Blue assay was performed as

described in Section 3.1. During initial experiments, cells were seeded at a density of $1x10^6$ cells/mL because this is a seeding density similar to that utilized in 2D culture. When the volume of suspended cells required for the desired cell density had been calculated, it was pipetted into a conical vial. The cell suspension was then centrifuged for 2 min. to form a pellet and media was decanted. Any remaining media was removed with a micropipette. The desired volume of HAMA and precursors (TEA and NVP only) was then pipetted into the conical containing the cell pellet. EY was not added at this point because it is light sensitive and would result in premature crosslinking. The pellet was then mixed into the HAMA mixture with repeated pipetting until the mixture was homogenous and all cells were in suspension.

4.1.3 Photoencapsulation

All equipment used for encapsulation was sterilized in 70 % ethanol. Equipment and solutions (HAMA, NVP and TEA) were then exposed to UV light inside the laminar flow hood for 30 min. Coverslips were coated with PLL as described in Section 2.3.2. The PLL mixture was left on coverslips overnight and aspirated on the day of culture. Before adherence of gels, the coverslips were completely dried under a laminar flow hood. Coverslips were then placed into the acrylate holding mold and PDMS cell culture molds were placed onto each coverslip with sterilized forceps (Figure 3.9). If coverslips and PDMS molds were not completely dry after sterilization in EtOH, some leaking of HAMA solution was observed. In this case, gels often did not hold the desired shape.

Eosin Y was then added only to the portion to be encapsulated immediately. Before addition of EY, lights in the laminar flow hood were turned off to avoid inadvertent excitement of the photoinitiator. Cell suspension in aqueous HAMA with precursors was then pipetted into the PDMS molds. The acrylic holding mold was then placed inside the photoencapsulation enclosure and exposed to high intensity LED light (~520 nm, 60 mW) for 2 min (Figure 3.10).

PDMS molds were carefully removed with sterilized forceps and coverslips with attached gels were placed into each well. Gels were then covered in DMEM/F12

media supplemented with 10 % FBS and 2 % PS. Media was changed every 3-4 days. Although great care was taken to gently wash and manipulate gels, some gels were lost during media changes due to weak adhesion of gels to the coverslip. After 4 days, gels were observed to determine the presence of cells. For imaging, gels were inverted onto coverglasses and viewed under differential interface contrast (DIC) on a Leica DMI6000B (Figure 4.3).

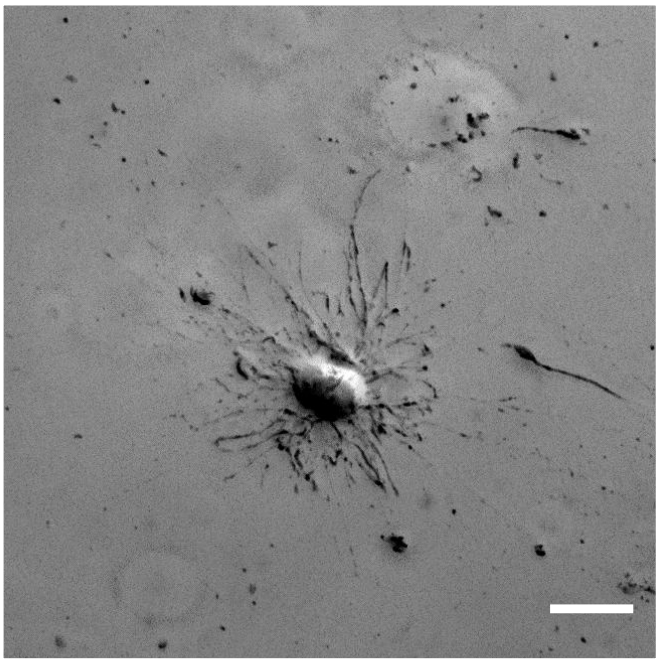

Figure 4.3: DIC image of a viable cell encapsulated in HAMA gel after 4 days.

Cells were considered viable if they had extended processes into the matrix and non-adherent if they appeared round and circular. Even without immunolabelling, many fine processes were visible on viable cells.

4.2 Optimizing Cell Viability Through Seeding Density

Although viable cells were identified in HAMA cultures after photoencapsulation, in the 0.5 wt% gel at a seeding density of $1x10^6$ cells/mL, viable cells were few and far between. The number of viable cells was not high enough for use as a model of glial scarring. One of the variables that can affect cell viability in culture is cell density. Cells interact through chemical cell-cell signaling which has been known to play a

role in cell survival [127-130]. Cell density has also been reported to influence supplies of oxygen and nutrients in culture which may also mitigate cell survival [127, 130]. The optimal seeding density for 3D culture may be higher than the required in 2D culture because cells in 3D are distributed throughout a greater volume than in 2D culture where cells form a monolayer. To evaluate how cell viability changes with increasing seeding density, cell-gel constructs were evaluated at cell densities between $1x10^6$ cells/mL and $1x10^7$ cells/mL over 7 days. Cells were encapsulated in the 0.5 wt% HAMA gel and monitored over 7 days. By day 7 cell processes were observed at both the $5x10^6$ and $1x10^7$ cell/mL cell densities (Figure 4.4). Cell processes were rarely observed at the $1x10^6$ cells/mL cell density even after 1 week of culture.

A live/dead membrane permeability assay was chosen to enable quick viability analysis within the gel. This assay uses two nucleic acid stains that selectively bind to dsDNA: Syto13 (Molecular Probes) is a membrane permeable dye that enters all cells, while StytoxOrange (Molecular Probes) is a membrane impermeable dye that only stains the nuclei of cells with compromised membranes. By using both of these dyes, it was possible to count those cells that living (Syto13, green) and dead/dying cells (SytoxOrange, red/orange). Co-labeling with both dyes is possible, but SytoxOrange is capable of displacing Syto13 from the dsDNA binding site at higher concentrations. This causes some dead/dying cells to appear orange (co-labeled) and others red (only SytoxOrange).

One day and 7 days post encapsulation, 5 mM Syto13 was added to each well. Thirty minutes later, 5 μM SytoxOrange was added to the same well and left on for 30 additional minutes. In total, cells were incubated with Syto13 for 30 min. and SytoxOrange for 1 hr. After the incubation period, cells were washed with DMEM/F12 three times and fixed with 10 % formalin for 20 min. Within 24 hr of staining the gels were imaged. If gels were imaged later than 24 hr, an increased number of co-labeled dead cells were seen. This is likely due to slight permeabilization of cell membranes and diffusion of the dyes through the gel. Dead cells appeared red or orange while live cells appeared green (Figure 4.5). Images were taken on an inverted fluorescent microscope so and out of plane cells appear

out of focus. Even without confocal microscopy, distinct nuclei were observed. Some cell clumping was seen in the gel in addition to individual cells. Negative controls for this assay were done with cell-less HAMA gels to verify that Syto13 and SytoxOrange did not label components of the gel (not shown).

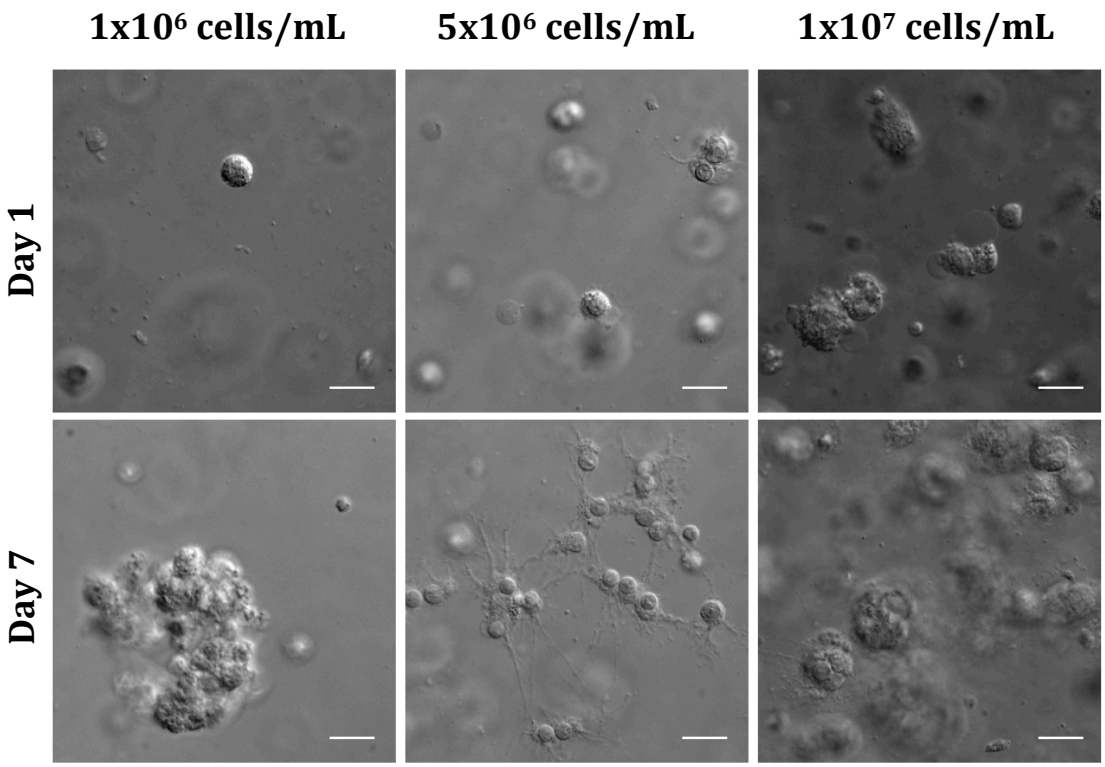

Figure 4.4: DIC images showing cell processes at seeding densities between 1x10⁶ and 1x10⁷ cells/mL over 7 days. Representative images of N=3 independent experiments. Scale bar20 µm.

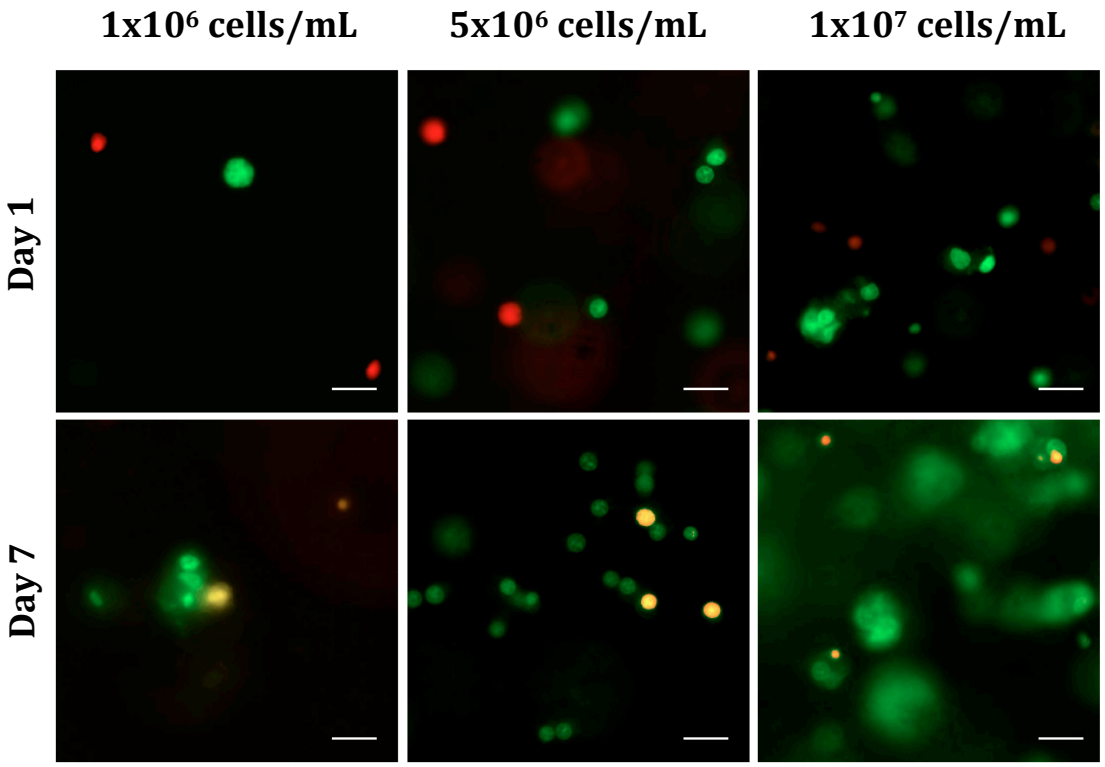

*Figure 4.5: Live/dead (**Syto13**/**SytoxOrange**) membrane permeability cell viability assay of cell densities between 1x10⁶ cells/mL and 1x10⁷ cells/mL at 1 and 7 days post encapsulation. Representative images of N=3 independent experiments. Scale Bar 20 µm.*

Cell viability at the various cell densities was also quantified by counting live and dead cells (Figure 4.6). A minimum of three wells and six images per well were counted in each experiment. These counts indicated a significant difference between cell densities.

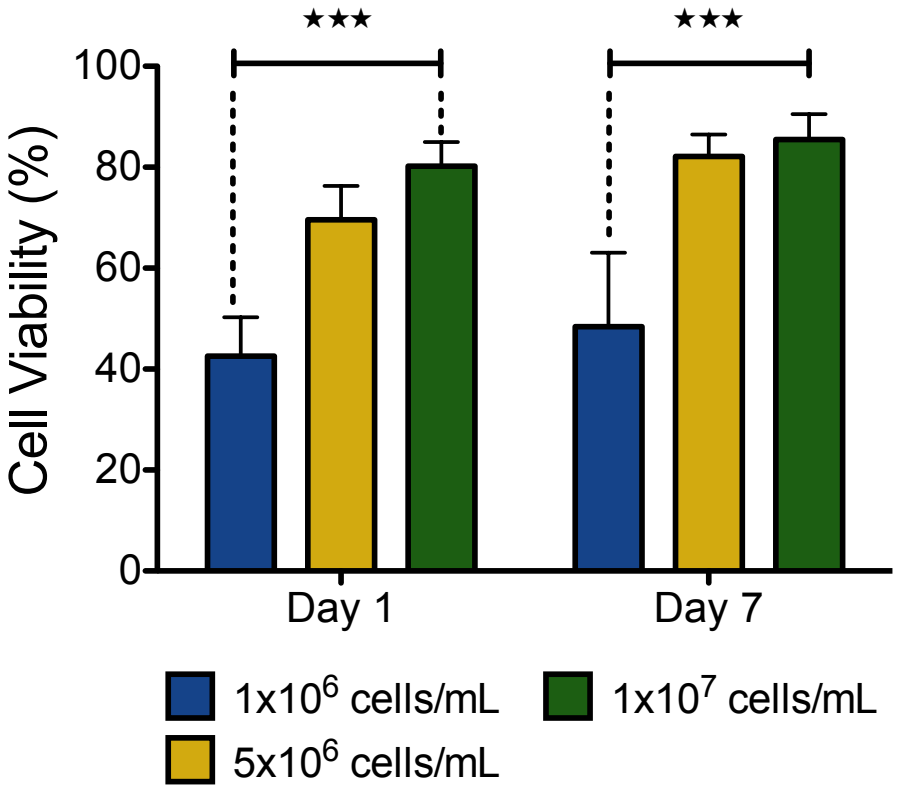

Figure 4.6: Quantification of cell viability at day 1 and day 7 for seeding densities between $1x10^6$ cells/mL and $1x10^7$ cells/mL. Representative images of N=3 independent experiments 2 way ANOVA. ★★★P<0.0001, SD.

At day 1 post encapsulation, cell viability for the lowest cell density ($1x10^6$ cells/mL) was 42.60 ± 7.67 % and the highest cell density ($1x10^7$ cells/mL) had a significantly higher viability of 80.20 ± 4.82 %. This trend of increasing cell viability was observed both with increasing cell density and increasing culture time post encapsulation. Cell viability at $5x10^6$ cells/mL (82.17 ± 4.36 %) was not significantly different from that of $1x10^7$ cells/mL cell density at day 7, but was significantly lower at day 1 (69.60 ± 6.73 % vs. 80.20 ± 4.82 %). The most consistent cell viability observed over one week of culture was at the $1x10^7$ cell/mL cell density.

Increasing cell viability at higher cell densities is likely due to the role of cell-cell interactions in cell survival [127-130]. Other *in vitro* 3D culture studies of microglia and astrocytes have reported use of similar cell densities [76, 131]. However, the actual density of microglia and astrocytes reported *in vivo* is much higher (~$3.4x10^{13}$ cells/mL) [126]. Glial cell density also varies with brain region, gender and age [132]. Because higher cell densities confounded effective characterization of cell morphology, they were not investigated. All subsequent experiments were carried out with a cell density of $1x10^7$ cells/mL allowing for optimal and consistent cell viability while still enabling cell morphology analysis.

4.3 Characterization of 3D Cultures

The live/dead assay indicated that viable cells were present in the gel, but did not characterize the cells present. To further develop a model for glial scarring it was essential to ensure that both microglia and astrocytes were successfully encapsulated, as they are the primary components of the glial scar. It is also important to investigate the morphology of microglia and astrocytes in the gel to determine if photoencapsulation had any affect. To characterize cells encapsulated in 0.5 wt% HAMA gels, fluorescent labeling was used. The procedure was similar to that used for 2D immunochemistry (Section 3.1) and also labeled Iba1 (microglia) and GFAP (astrocytes). Some alterations, namely increasing Triton X-100 concentration and duration of secondary antibody labeling, were made to account for slower diffusion of antibodies through the gel.

Seven days post encapsulation in a 0.5 wt% HAMA gel, cells were fixed with 10 % formalin for 20 min at room temperature. After fixing, the cells were washed 3 times with PBS and incubated in blocking buffer (PBS, 0.5 % Triton X-100 and 10 % NHS). After a one hour incubation time with mild shaking, cells were washed three times with PBS and both primary antibodies (anti-mouse GFAP and anti-rabbit Iba1) diluted 1:1000 in PBS with 0.2 % Triton X-100 were applied. The cells were then incubated overnight at 4 °C with mild shaking.

The next day, after the primary antibodies were applied, gels were washed three times with PBS and secondary antibodies, Alexa Fluor 488 donkey anti-rabbit (Molecular Probes, 1:200) and Alexa Fluor 647 donkey anti-mouse (Molecular Probes, 1:200) with 0.2 % Triton X-100 were added. The gels were incubated overnight at 4 °C with mild shaking, then the secondary antibodies were removed and gels washed three times with PBS. For imaging, gels were inverted onto glass slides essentially sandwiching the gel between two glass surfaces. Images were taken on a Leica DMI6000B inverted fluorescent microscope through a series of z planes and maximum projections were compiled in ImageJ software to represent 3D images in 2D. Negative controls were performed in the same manner as 2D cultures to ensure non-specific labeling was not taking place.

Astrocytes appeared with extensive processes (Figure 4.7 A) and were sometimes clustered in the gel. Microglia present in the gel often appeared rounded with a circular morphology similar to that seen in 2D (Figure 3.4) as seen in Figure 4.7 A, but were also seen with numerous extended processes (Figure 4.7 B) indicating a more ramified microglial morphology. Microglia also appeared to wrap processes around other cells in the gel, perhaps indicating phagocytic activity. From these observations, it was concluded that both microglia and astrocytes were not only viable within the gel, but also attaching to the gel, interacting with the gel and interacting with each other in a manner characteristic of *in vivo*. The bright cell body labeling observed with Iba1 made it difficult to see less intensely labeled microglia processes.

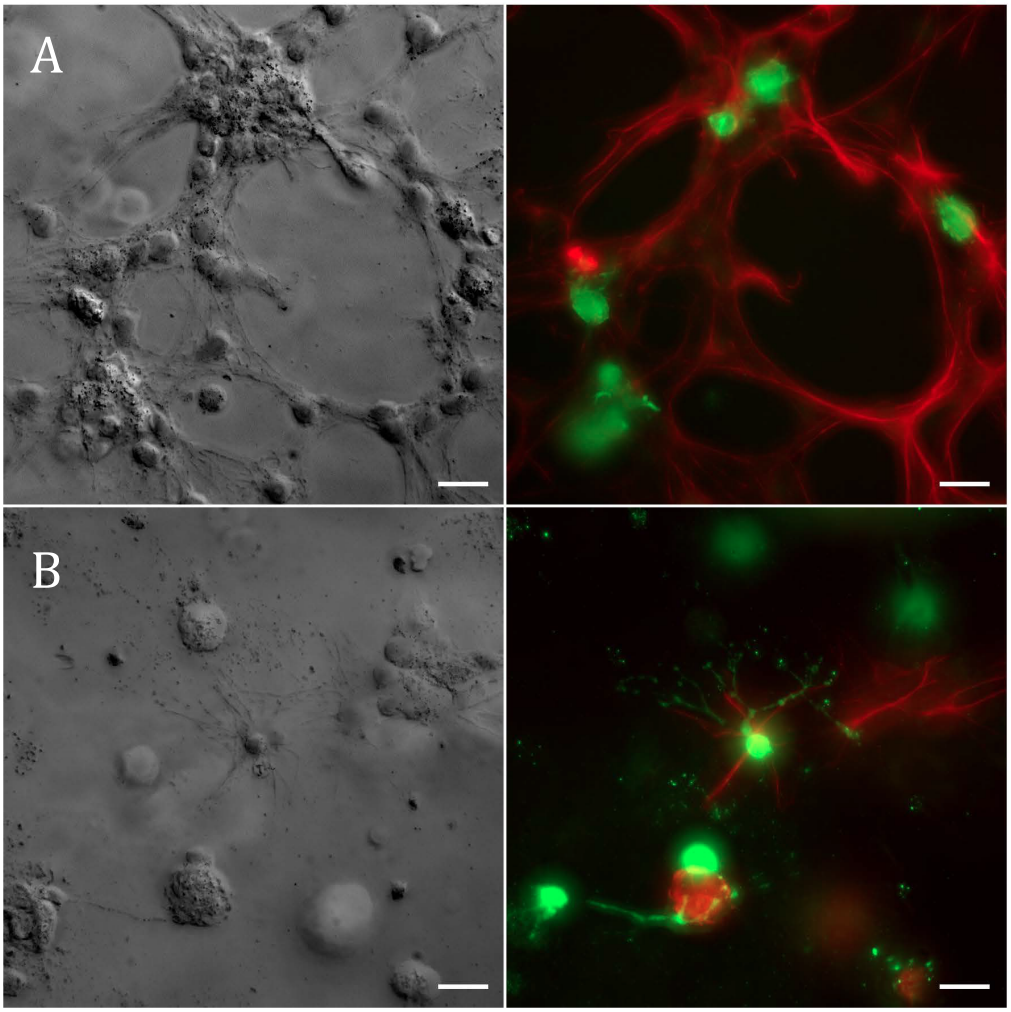

*Figure 4.7: Left: DIC images, Right: Astrocytes (**red**, GFAP) and microglia (**green**, Iba1). Cells cultured for one week in 0.5 wt% HAMA gel. Scale bar 20 µm.*

Few studies exist of 3D mixed glial cultures. Frampton et al. demonstrated a 3D alginate mixed culture of astrocytes and microglia, in which microglia appeared to have an amoeboid/activated morphology with only short processes [76]. There are considerably more studies of 3D astrocyte cultures with or without neurons [75, 88, 131, 133, 134]. In all of these studies, astrocytes appeared with a similar stellate morphology to cells in Figure 4.7 and different from 2D morphology in Figure 3.4. *In vivo* histology and 3D confocal reconstruction has also shown similar microglia and astrocyte morphologies [135, 136]. Processes in both astrocytes and microglia extended through multiple z planes of the gel indicating that the cells were interacting with the 3D environment of the HAMA scaffold.

4.4 Varying HAMA wt%

Varying macromer weight percent was shown to modify gel elastic modulus (Section 2.4). Changing modulus would allow for flexibility when modeling different regions of the brain (white matter vs. grey matter etc.). However, changing macromer weight percent also altered the structure of the gel (Section 2.4) and it was important to assess how this might affect cell viability. Over 7 days, cell viability was analyzed with a membrane permeability live/dead assay (Section 4.2) at macromer weight fractions between 0.5 and 1.5 wt% (Figure 4.8). Distinct nuclei were observed for both live (green) and dead (red/orange) cells. Cells out of plane appeared out of focus, but did not interfere with cell counting. DIC images were also taken at each time point. These images show cell processes extension for all weight percentages by day 7 post encapsulation except 1.5 wt% (Figure 4.9).

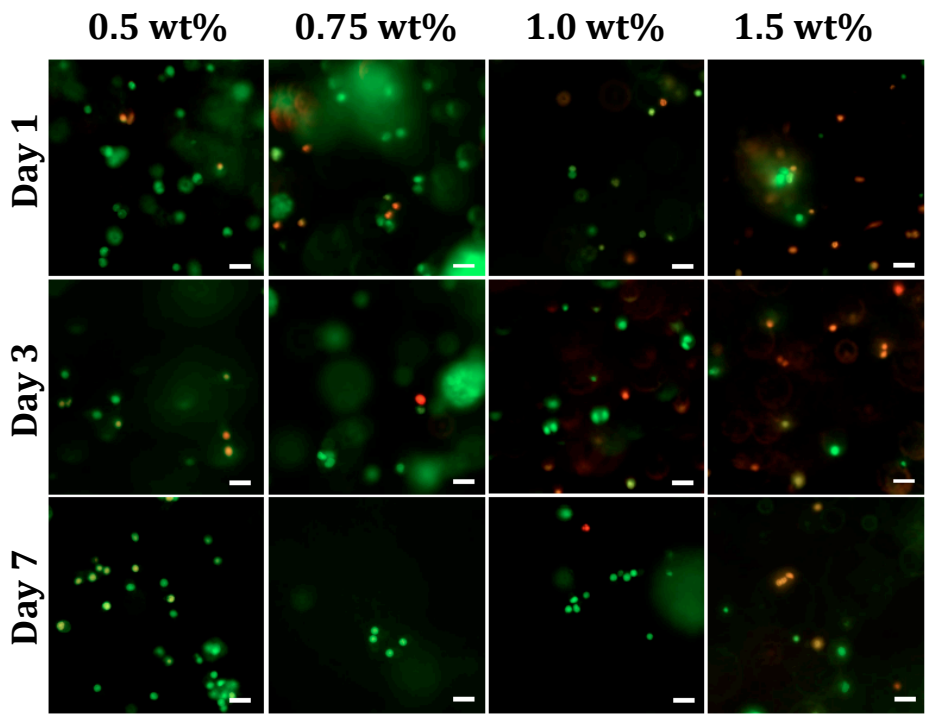

*Figure 4.8: Live/dead (**Syto13**/**SytoxOrange**) membrane permeability cell viability assay of macromer concentrations between 0.5 and 1.5 wt% at 1, 3 and 7 days post encapsulation. Representative images of N=3 independent experiments. Scale Bar 20 µm.*

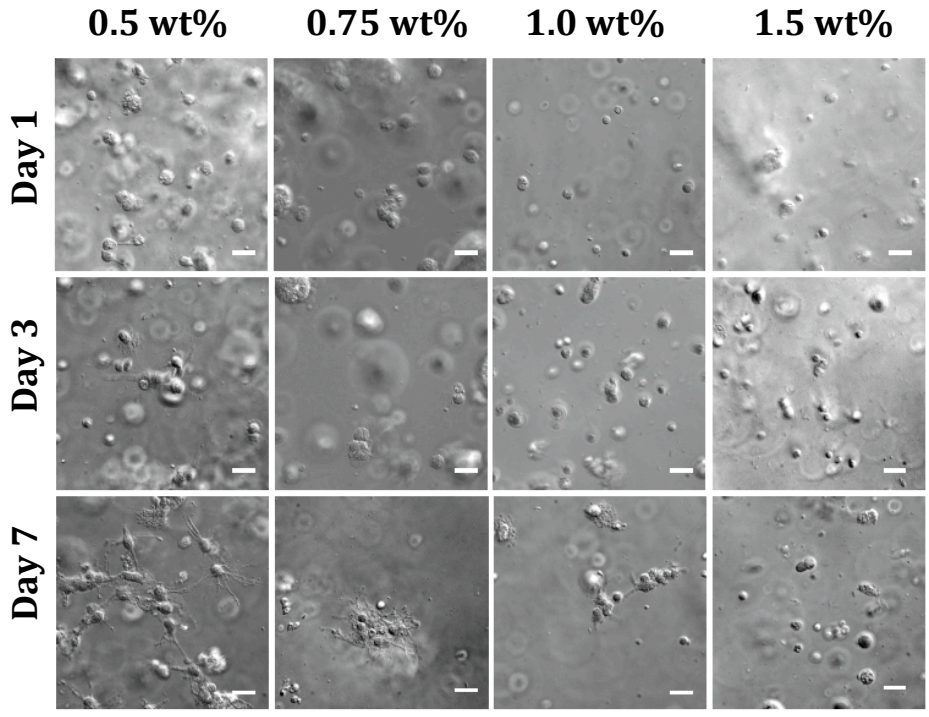

Figure 4.9: DIC images showing cell processes at macromer weight percentages between 0.5 and 1.5 wt% over 7 days. Representative images of N=3 independent experiments. Scale bar 20 µm.

Cell viability at the various cell macromer weight fractions was quantified by counting live and dead cells (Figure 4.10). In accordance with counts performed in Section 4.2, a minimum of three wells and six images per well were counted in each experiment. These counts indicated a significant difference between cell densities.

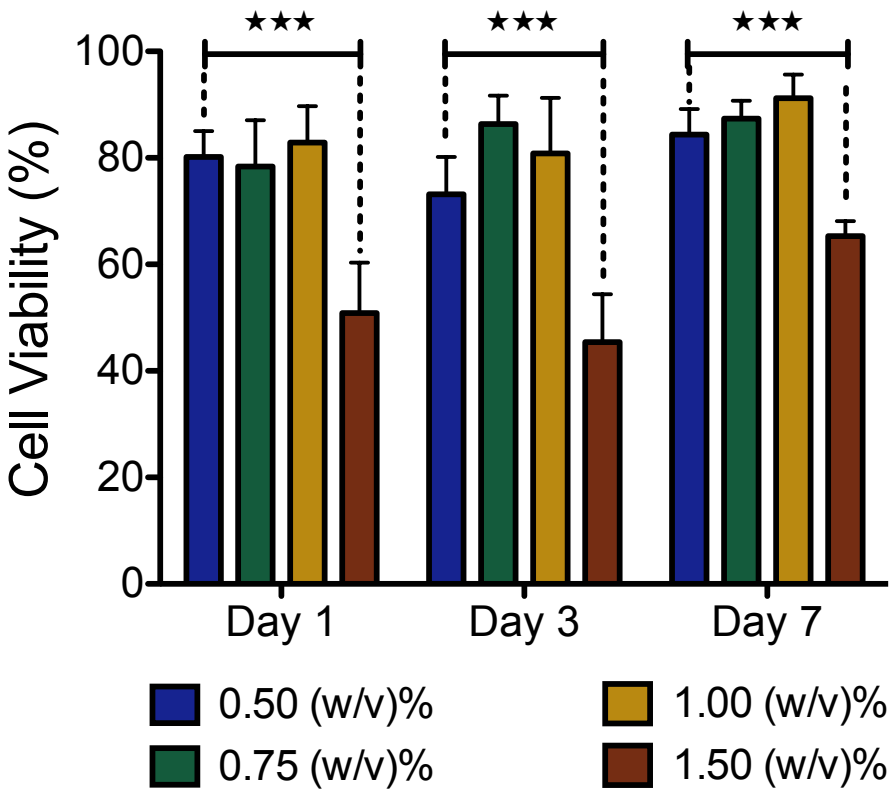

Figure 4.10: Quantification of cell viability at day 1 and day 7 for seeding densities between 1x10⁶ cells/mL and 1x10⁷ cells/mL. Representative images of N=3 independent experiments. 2-way ANOVA. ★★★P<0.0001, SD.

Cell viability was consistent for macromer concentrations between 0.5 and 1.0 wt% over all 7 days at ~80 % (Figure 4.17). However, cell viability decreased significantly at 1.5 wt% (~50 %). Although some recovery of cell viability was seen at day 7 with 1x10⁶ cells/mL cell density (42.60 ± 7.67 % to 48.40 ± 14.67 %), cell viability did not recover to that of 1x10⁷ cells/mL cell density at day 7 (85.50 ± 5.05 %).

Although HAMA gels became stiffer with increasing macromer weight fraction, physical cues from increasing stiffness are unlikely the cause of increased cell death. In 2D culture, cells are grown on substantially stiffer polystyrene culture plates without affecting cell viability. Varied scaffold stiffness has been correlated with processes extension, cell differentiation and varying cell expression, but not cell death [72, 88, 130, 137-140]. Some studies have shown decreasing pore size of hyaluronic acid gels with increasing macromer weight percent, which may affect cell viability [141, 142]. However, CryoSEM data in Section 2.5 indicated no obvious change in pore size. Instead, CryoSEM data indicated a change in wall thickness. The walls of the lowest weight percent gel (0.5 wt%) were extremely thin (almost electron transparent) while the 1.5 wt% gel had much thicker walls. This may limit the ability of glia to modify the gel structure as well as the transportation of nutrients through the gel. Another possible explanation for increased cell death could be reaction kinetics during encapsulation. Altering the macromer concentration changes the number of acrylate groups available for crosslinking and is likely to change crosslinking kinetics. Changes to the number of radical groups during crosslinking, speed of the reaction, initiation of the reaction or termination of the reaction could effect cell viability [138].

4.5 Electrode Stability and Visualization

For the HAMA gel-cell system to be a successful model of glial scarring, the electrode must be stable in the gel under culture conditions. Loss of the electrode or extensive electrode shifting would compromise the study as each time the electrode moved to a new location, as though the glial response was starting over. Because the extent of glial scarring is determined by cell density at the electrode, it is also important that microglia and astrocytes can be visualized at the electrode surface.

To assess electrode stability, a Pt/Ir polyimide coated microwire with a 30 μm diameter was inserted into HAMA gels with encapsulated cells. Wires were sterilized in the same manner as 2D electrode drop experiments (soaked in 70 % EtOH for 30 min, dried under UV light). When dry, electrode pieces were carefully lifted with sterilized forceps and gently inserted into gels 4 to 7 days post

encapsulation. To aid in gel manipulation during insertion, gels attached to coverslips were lifted out and placed into the acrylate holding mold (Chapter 2). This allowed the gel to be tilted and moved to achieve the ideal angle for electrode insertion. Great care was taken to insert wires into the center of the gel and not along the bottom next to the coverslip (Figure 4.11).

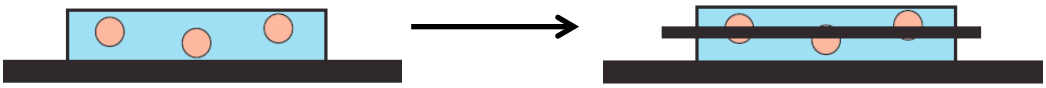

Figure 4.11: Schematic showing microwire insertion into HAMA gels with encapsulated mixed glial cultures

Gels supported suspended electrodes and no electrode shifting was observed during culture. To determine if cells could be visualized at the electrode interface, microglia and astrocytes were labeled following the protocol described in Section 4.3 (Figure 4.12).

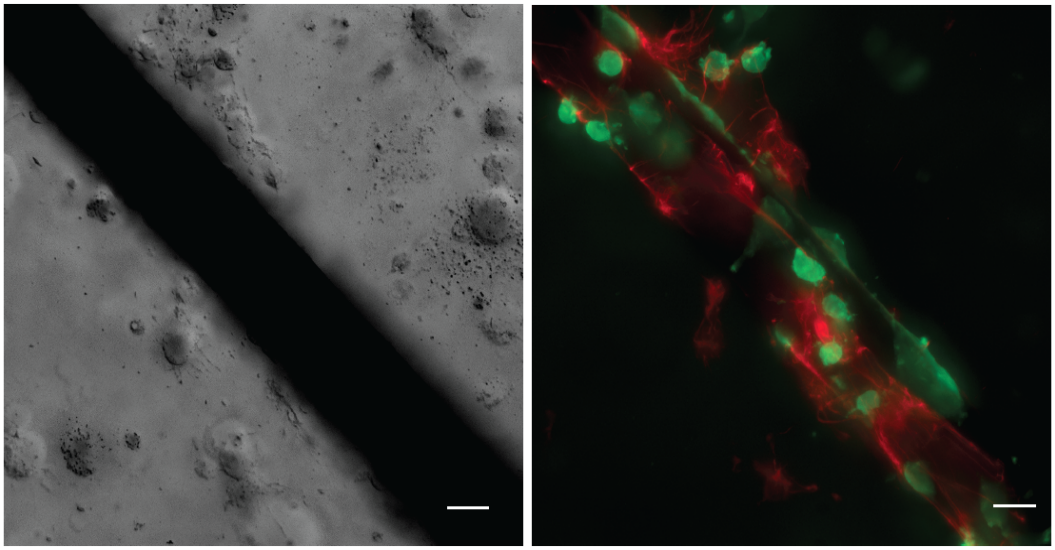

*Figure 4.12: DIC image of electrode inserted into cells encapsulated in crosslinked 0.5 wt% HAMA gel after 1 week post insertion (left) and Microglia (Iba1, **green**) and astrocytes (GFAP, **red**) appearing at electrode interface (right). Scale bar 20 µm.*

Both microglia (Iba1, green) and astrocytes (GFAP, red) were seen at the electrode one-week post insertion (Figure 4.12). Microglia appeared with a circular morphology characteristic of an activated morphology. Some microglia appear to be

spread out along the electrode as if they were attempting phagocytosis. Astrocytes also appear at the electrode interface although it is difficult to differentiate between protoplasmic and fibrous morphologies. From these images it is also impossible to determine the state of astrocyte activation (normal vs reactive). It does appear that astrocytes are lining the electrode forming a glial scar.

4.6 3D Electrode Time Course

Microglia react first to the electrode within hours to days and astrocytes follow shortly after within a week during *in vivo* studies. This is known as the acute inflammatory response. The chronic inflammatory response (and increasing cell density) has been known to continue for many weeks after the electrode is inserted and has been reported for months. Astrocytes *in vivo* have been reported to increase in density up to 500 μm from the electrode over 12 weeks post implantation [15]. Analysis of stab wounds in rats has reported a noticeable increase in microglia at day 1 with peaks in number microglia at day 3 and day 7 [124]. Because this study was of a stab wound (the microwire was removed immediately after insertion), the number of microglia decrease significantly after 7 days, returning to base levels [124]. *In vivo* studies of the cellular reaction to foreign bodies have also indicated an increase in microglia at the electrode as early as days 1-4 [15]. Reports of the microglial response at later time points is varied with some reporting a sustained glial response up to 16 weeks post implantation and others claiming no microglia at the electrode. The temporal response of microglia and astrocytes were monitored over 21 days to determine the extent of glial scarring (acute or chronic) and compare it to previously reported results.

Wires were inserted into gels following the same procedure used in Section 4.5. At each time point gels were removed, cells were fixed with formalin and cells were labeled using the immunolabelling procedure standardized in Section 4.3. Immunomicrographs of glial scarring were taken at both 10x (Figure 4.13) and 40x (Figure 4.14) magnification.

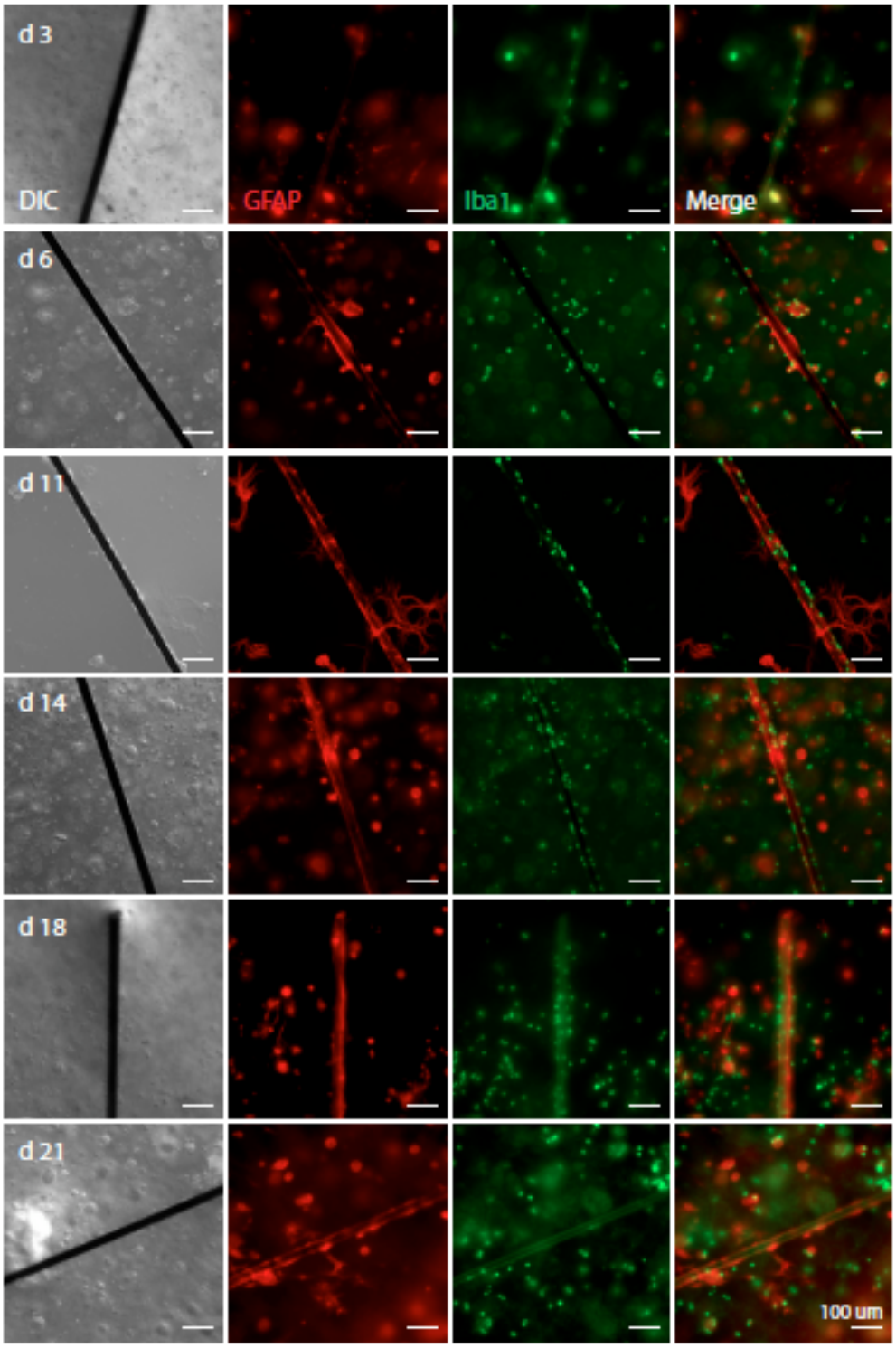

*Figure 4.13: Progression of glial scarring over 21 days in 3D mixed glial cultures. Microglia (Iba1, **green**) and astrocytes (GFAP, **red**) at the electrode. Low magnification (10x), representative images of N=3 independent experiments.*

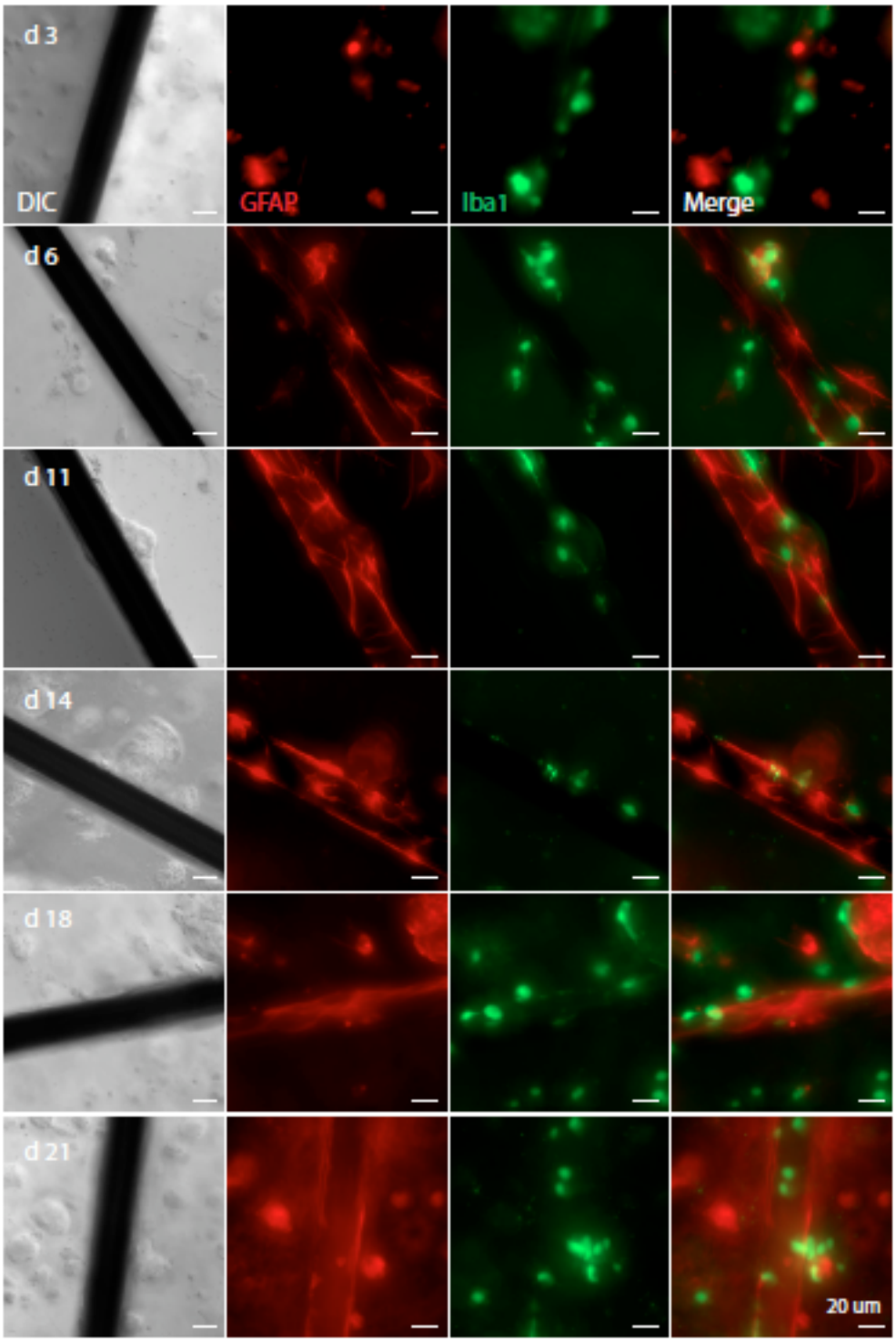

*Figure 4.14: Progression of glial scarring over 21 days in 3D mixed glial cultures. Microglia (Iba1, **green**) and astrocytes (GFAP, **red**) at the electrode. High magnification (40x), representative images of N=3 independent experiments.*

The temporal response of microglia and astrocytes to the electrode was similar to that observed in 2D (Chapter 3), but slightly delayed. Microglia (Iba1, green) were seen at the microelectrode by day 3 in the hydrogel model, while they were first seen at day 1 in the monolayer model. Astrocytes (GFAP, red) were first observed beginning to line the electrode at day 6 in the hydrogel model and began to line the electrode by day 4 in the 2D culture. This delay may be due to reduced motility of cells or limited diffusion of signaling factors in the gel when compared to the 2D system. By day 11 there was an obvious presence of astrocytes at the electrode interface. Although this is different from the 2D model, it is within the expected time period reported in literature [130]. At later time points (14-21 days), microglia and astrocytes remained at the electrode, but no obvious further increase in astrocyte cell density was observed.

As described in Section 1.2, the cellular response to neural interfacing electrodes is classified as the acute inflammatory response, glial scarring and the chronic inflammatory response (Figure 1.1). The amoeboid morphology of microglia and the appearance of astrocytes at the electrode interface (Figures 4.13 and 4.14) up to day 6 reflect the acute inflammatory response reported in literature [15, 17]. Glial scarring and the chronic inflammatory response is typically described as persistent activation of microglia and astrocytes for weeks and months after electrode insertion. This chronic inflammatory response and glial scarring is often classified as increased cell density at the electrode, which could not be discerned from Figures 4.13 and 4.14 due to confounding luminescence from other planes [17]. A common challenge when imaging 3D gels was obtaining images without confounding luminescence from other planes. Cells from above or below the electrode interface produced a haze that made it difficult to clearly determine the cell density at the electrode. To overcome these limitations when imaging 3D gels, images from day 6 and day 21 gels were taken again on a confocal microscope (Figure 4.15).

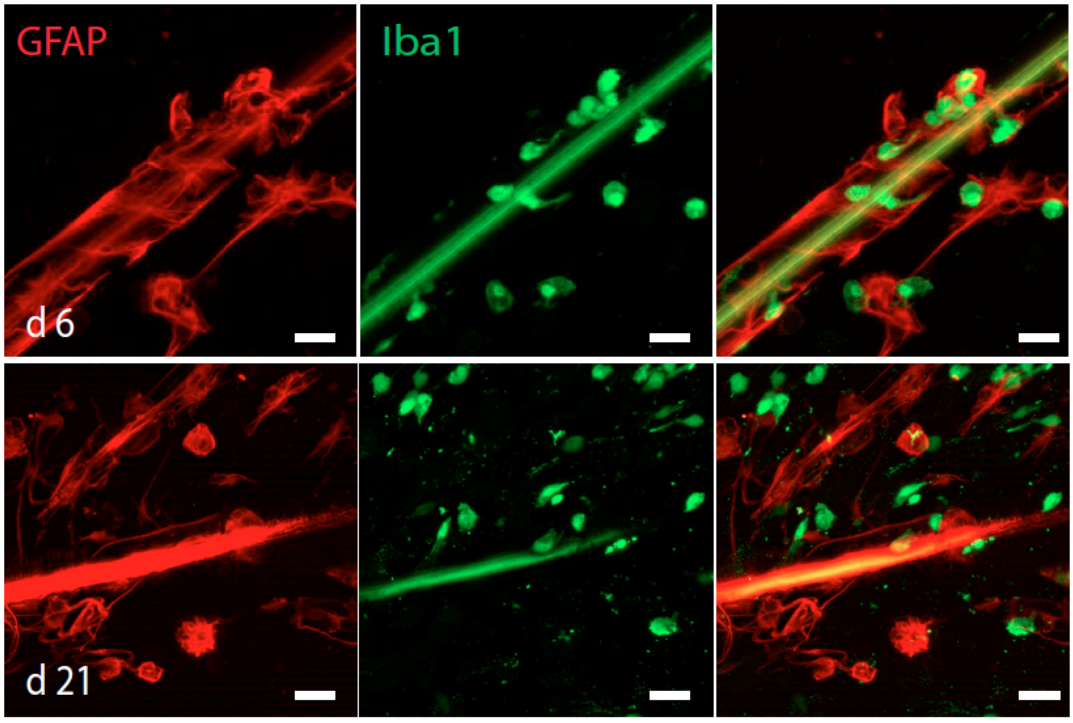

*Figure 4.15: Confocal microscopy images at day 6 and day 21 after electrode insertion. Microglia (Iba1, **green**) and astrocytes (GFAP, **red**). Scale bar: 30 um.*

Confocal microscopy provided clear images of both microglia (Iba1, green) and astrocytes (GFAP, red) at the electrode both at day 6 and day 21 post electrode insertion. Confocal images show microglia with an amoeboid morphology at day 6 and this morphology persists at day 21 (Figure 4.15). Astrocytes are also persistent at the electrode interface in the confocal images. It is difficult to determine if the astrocytes are in their reactive phenotype because indicators of astrocyte activation including migration, proliferation and hypertrophy were not directly measured. It was also difficult to determine an increase in cell density at the electrode even after confocal imaging. From Figures 4.13 to 4.15, cell density at the electrode appears to remain consistent between day 6 to day 21. To determine if the cell-gel system is modeling the chronic inflammatory response, further quantification of cell density at the electrode and investigation into the activation state of astrocytes and microglia would need to be performed.

There are also many differences between *in vivo* tests and our 3D model that may explain a lack of increased cell density over 21 days including micromotion and chemical stimuli. Electrodes inserted into the CNS also undergo continuous

micromotion, which is absent in the current 3D model [11, 17]. It is possible that one or some of these factors may need to be added to the model before it can effectively model chronic glial scarring to electrodes. The 3D *in vitro* model also fails to mimic the breach of the blood brain barrier and cell injury. As a result, many of the factors present after electrode insertions *in vivo* are not present in the 3D model including pro-inflammatory cytokines, growth factors and adenosine triphosphate (ATP) [11, 66, 143, 144]. The model could be easily manipulated to incorporate these differences by introducing soluble factors present after a breach of the BBB or gentle shaking during culture to model micromotion. In addition, these factors could be added to the 3D *in vitro* model individually in a controlled manner to determine which factors and to what extent each factor contributes to chronic glial scarring.

4.7 Summary

Mixed glial cultures were successfully encapsulated via photopolmerization. This method allowed for homogenous distribution of cells throughout the HAMA gel. Cell viability increased with increasing cell density and optimal cell density for identification and viability was determined to be 10^7 cells/mL. Although this cell density is similar to other 3D culture models of glia, actual cell density in the brain is orders of magnitude higher [76, 134]. In the future, this cell density may have to be further optimized for the foreign body response model. Both microglia and astrocytes were successfully encapsulated and cultured for one week. Cell morphologies were representative of that seen *in vivo* and in other *in vitro* 3D cultures containing glia [76, 88, 131, 132]. With increasing macromer weight percent, cell viability decreased. One possible explanation for this decreasing viability at increased macromer weight fractions is the increasing wall thickness observed in Section 2.5.2. A 30 μm microwire was stable after insertion in 0.5 wt% gels and microglia and astrocytes were visible at the interface. This model system successfully modeled the acute inflammatory response. The persistent amoeboid morphology of microglia between day 6 and day 21 post electrode implantation indicates sustained activation of microglia as part of the chronic inflammatory response. However, it was difficult to determine an increase in cell density at the electrode and the activation state of astrocytes. Further experiments may be

required to verify persistence of glial activation and chronic inflammation over 21 days. Other factors (cytokines IL-1α, IL-1β , growth factors PDGF and BMP-2, micromotion or ATP) may be necessary to produce consistent glial scarring over an extended period [66, 143, 144].

Chapter 5.0

Future Work and Conclusions

5.0 Overview

The work described in this thesis covers the initial setup and characterization of a model system for the 3D culture of microglia and astrocytes in an HAMA hydrogel. This chapter discusses possible future directions for the model including improvements to the model system, further understanding the extent of the model and future experiments. Finally, thesis conclusions are summarized.

5.1 Improving the Photocrosslinking System

In Chapter 2, the first steps towards creating a reliable, high-throughput photocrosslinking system were. This development included gel attachment of HAMA gels to glass coverslips, an enclosure that controlled the height, and therefore intensity, of the light source and choosing precursor concentrations to initiate crosslinking. Additional steps to further optimize the photocrosslinking system are described below.

5.1.1 Gel Attachment to Coverslips

Gel attachment to glass coverslips is required as part of the photocrosslinking system to allow manipulation of the gels. This is essential for the insertion of microwires and prevents gels from being aspirated during media changes and immunolabelling. For all experiments in this thesis, PLL was used to adhere gels. Though the electrostatic bond between the gel and PLL held gels to the coverslips, some gels were still lost during washes [145]. To reduce the number of gels lost during culture and labeling, a stronger bond is recommended. Both 3-(Trimethoxysilyl)propylmethacrylate (TPM, Sigma) and (3-Aminopropyl)triethoxysilane (APTS, Sigma) were considered as possible alternatives [146, 147]. The covalent bonding provided from these coatings is expected to be stronger than the electrostatic bonding achieved with PLL [146, 147]. Preliminary testing indicated that both TPM and APTS bonded HAMA gels to glass coverslips, as crosslinked gels without cells were stable under cell culture conditions for 2 weeks. Further experiments with encapsulated cells in the HAMA gels are required to test the feasibility of these coatings for 3D cell culture.

5.1.2 Light Distribution

Photocrosslinking of HAMA is initiated when the precursor EY is excited by green light (~523 nm, 60 mW) as described in Section 2.3. Crosslinking was performed under one 3 LED clustered array from Cree. The clustered array was able to illuminate a circular area with a diameter of ~ 90 mm before the light intensity drastically decreased. In some crosslinking experiments, it was observed that gels on the edge of this radius did not crosslink as thoroughly as those in the center, indicating a decrease in light intensity near the edge of the illuminated area. If more than one holding mold is used at a time, improved light distribution would be required to ensure crosslinking of all gels. A new setup is proposed with multiple LED clusters distributed such that the illuminated areas overlap (Figure 5.1). To ensure even light distribution, a diffuser could be designed that would sit between the LED array and the holding mold [148].

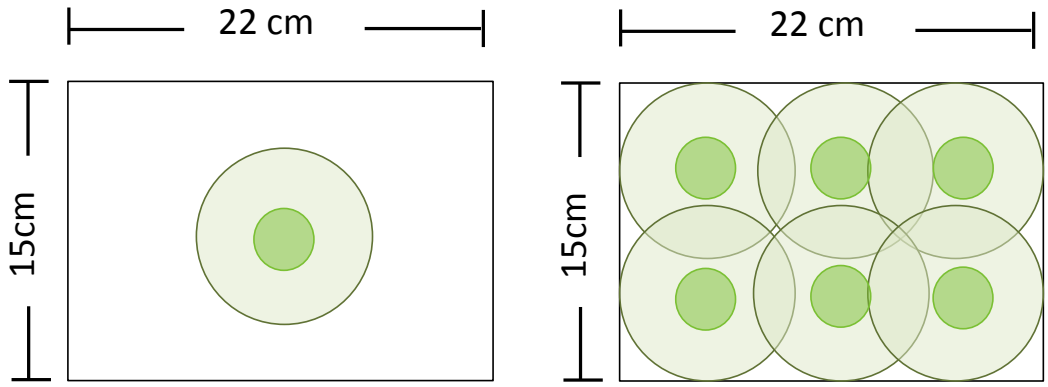

Figure 5.1: Schematic of photocrosslinking enclosure with one LED cluster array and the area illuminated by that array (left) and the proposed set of LED clusters organized with overlapping regions of illumination (right).

5.1.3 Optimize Precursor Concentration and Light Exposure Time

In Chapter 2, Section 2.3, precursor concentrations were chosen based on previously tested cell viability outcomes and duration of light exposure was chosen arbitrarily based on previous literature [72, 99]. The lower precursor concentrations (0.1 % (w/v) TEA, 0.1 % (w/v) NVP and 0.01 mM EY) were determined to cause minimal cell death and therefore considered better than the higher concentrations tested [99]. However, only two concentrations were tested and the effects of light intensity of duration were not considered. The reason this was not done is because

it is difficult to determine empirically when the HAMA gel is fully crosslinked. As such, it is possible that precursor concentrations, light intensity and duration of light exposure may still be higher than necessary. To ensure cells are not exposed to radicals or precursors unnecessarily during crosslinking, an evaluation of crosslinking kinetics would be necessary. Varying precursor concentrations, light intensity and exposure while assessing the HAMA gel point (when the gel becomes fully crosslinked) would determine the ideal photocrosslinking environment. This could be done using techniques such as Photo Differential Scanning Calorimetry (DSC) or Photo Rheometry [72, 149, 150].

5.2 Streamlining Cell Isolation

The isolation of microglia and astrocytes from whole tissue in Chapter 3 is necessary for photoencapsulated. The isolation procedure described in Chapter 3 involves the culture of a mixed glial population on culture plates. Over the course of one week, cells that are not supported by nutrients in the culture media die off, leaving microglia, astrocytes and oligodendrocytes. These cells were then resuspended for encapsulation. During optimization, this method allowed mixed glial cells to be isolated from whole brain tissue and reduced the amount of debris during encapsulation. However, purer cultures could be obtained directly, perhaps more effectively via a separation method such as a Percoll gradient [151, 152]. Percoll is a low viscosity density gradient that allows cells to be separated based on density [153]. It is used to isolate cell types, organelles and viruses [153]. A percoll separation protocol involves mixing the cell homogenate after initial trypsinization followed by density centrifugation [153]. Layers with a density similar to that of microglia and astrocytes would then be removed to selectively isolate these cells. This would not only potentially increase specificity and yield, but also decrease time between cell isolation and encapsulation.

5.3 Increasing Model Complexity

Throughout this thesis, cell focus has revolved around microglia and astrocytes. These cell types were chosen specifically because they are the primary responders

to foreign bodies in the CNS and are known to play a crucial role in glial scarring [15, 17]. The reduced complexity of the developed model allows researchers to take a critical view of how electrode parameters influence the response of microglia and astrocytes specifically. However, there are other cell types in the CNS and it would be naïve to pretend they were not also of interest during the analysis of glial scarring. One cell type of particular added interest is the neuron. Neurons produce signals picked up by recording electrodes. Neuronal cell death and the retraction of neuronal processes from the electrode result in loss of electrode functionality [17]. As such, the end goal of mitigating glial scarring is to improve neuronal signals. The addition of neurons to the model would allow the overall affect of electrode design on neuronal growth and survival to be monitored. Though not trivial, many research groups have successfully cultured neurons in 3D gels [75, 86, 130, 131, 134, 154]. In fact, neurons are one of the most commonly 3D cultured neuronal cell followed by astrocytes. As a new cell type in the model, neurons would require unique preparation methods, growth factors, and possibly attachment motifs.

In Chapter 2, microglia and astrocytes were obtained from day 1 Sprague-Dawely rat pups. Although neurons are also present in the tissue used to obtain microglia and astrocytes, post-natal neurons are less plastic and more difficult to culture. Instead, pre-natal neurons are more commonly cultured because they are more robust and rebound from the isolation procedure more easily. As a result, the isolation and culture configuration must be optimized again when neurons are added to the model. Many possible culture configurations exist and some suggested possibilities are depicted in Figure 5.2. The first suggested configuration involves the seeding of neurons onto pre-existing mixed glial cells in an HAMA gel (Figure 5.2 A). In this configuration, neurons would grow on top of the gel and extend processes into the gel. In this way, the extension or retraction of neuron processes could be analyzed. Figure 5.2 B shows a second suggested configuration with microglia, astrocytes and neurons all encapsulated together in the gel. One possible caveat of this method is that neurons are known to be quite sensitive to radicals and therefore may be more sensitive to the encapsulation process. A third option, Figure 5.2 C, enables the separation of neuronal and glial media. Here, mixed glial cultures are encapsulated on the underside of a culture insert. Inserts allow the

exchange of soluble factors across a fine mesh, but not through the walls of the insert. Neurons would then be cultured in a monolayer on the topside of the mesh. Neurons in this configuration can extend processes across the mesh in response to glial response on the underside. The last configuration is depicted in Figure 5.2 D, and consists of a mixed glial culture encapsulated in an HAMA gel with a separate HAMA gel containing neurons crosslinked on top. This method would require a two-step photocrosslinking process. Neurons and glia would again share media as cell do in configurations A and B, but not C and the neurons would be layered on top of mixed glial cultures instead of mixed with glial cells as they are in A and C. However, instead of a monolayer of neurons, a 3D culture of neurons would exist. The benefit of this method is that a unique matrix could be developed for neurons separate from the matrix used for glial encapsulation. Which of these culture configurations would be optimal depends upon both the research question being asked as well as challenges that may arise during neuronal culture.

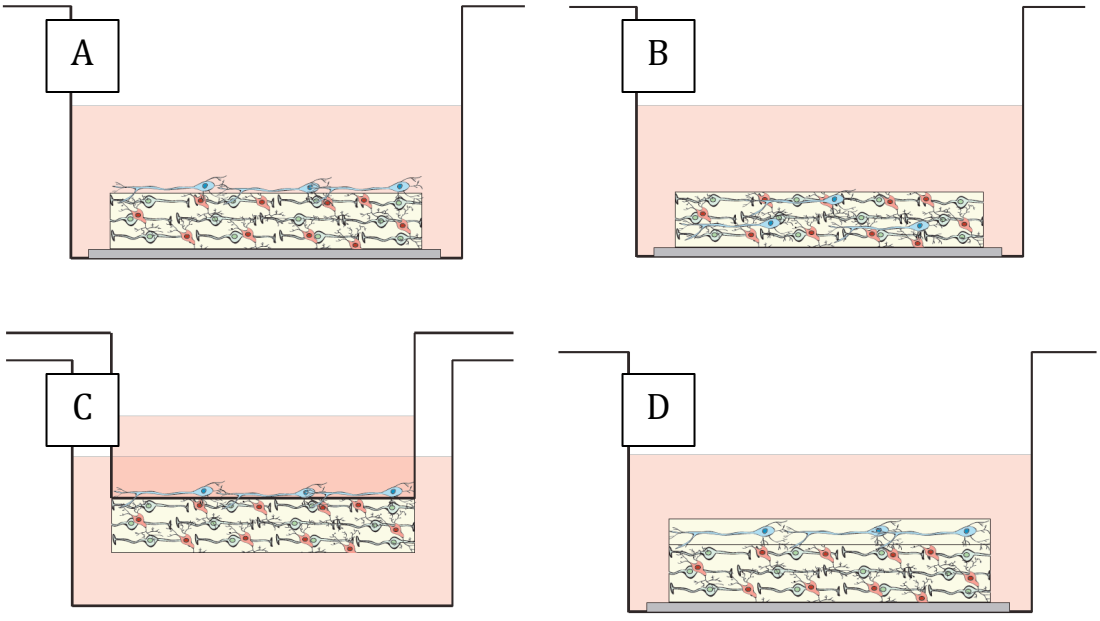

*Figure 5.2: Possible culture configurations for the culture of microglia (**red**), astrocytes (**green**) and neurons (**blue**) together. A) Microglia and astrocytes encapsulated in HAMA gel attached to a glass coverslip with neurons seeded on top of gel. B) Microglia, astrocyte and neurons encapsulated in HAMA gel together. C) Microglia and astrocytes encapsulated in on the reverse side of a culture insert with neurons seeded on the other side. D) Microglia and astrocytes encapsulated in an HAMA gel attached to a coverslip with neurons encapsulated in a gel layered on top of the mixed glial culture.*

Microglia and astrocytes cultures were supplemented with 10 % FBS, 2 % PS and DMEM/F12. This combined culture media provided microglia and astrocytes with the nutrients and growth factors they required to survive and proliferate. Neurons require additional growth factors for optimal survival and growth including B-27 and L-glutamine [130]. In 2D culture 2 % B-27 and 500 μM L-glutamate are added prior to plating. It is also common practice to only change part of the culture media each time to maintain growth factors in the media released by neurons during culture. In addition, neurons do not proliferate in culture. As other cells proliferate (particularly astrocytes) they often compete with neurons for space. As a result, culture media should be considered when adding neurons to the model. In most culture configurations, neurons and glia share culture media. In these cases, culture media must be optimized to determine which combination of FBS, B-27 and L-glutamate will support neurons, microglia and astrocytes together. In configuration C from Figure 5.2, the insert allows a separation of media between the neurons and mixed glia.

In addition to changes that may have to be made to culture preparation and media, neuronal cell attachment should also be considered. Although the results of this thesis indicated glial cell attachment, literature reports low cell attachment for cells grown on hyaluronic acid gels [155]. Collagen, gelatin and RGD are often added to hyaluronic acid gels in order to encourage neuron attachment [130]. Preliminary experiments of the encapsulation of neurons from embryonic Sprague-Dawley rats in HAMA gels found a lack of processes extension and low cell viability. These experiments were performed with the intention of culturing only neurons and so did not contain microglia or astrocytes. *In vivo*, microglia, astrocytes and neurons have an interdependent relationship [130]. Glial cells are known to release many factors that regulate neuron growth, differentiation and function thereby drastically improving neuronal survival [130]. It is possible that the culture of microglia and astrocytes with neurons would improve cell attachment. Further testing must be performed to determine which environment optimizes neuronal viability, growth and function.

5.4 Establish Degree of Response (Acute vs Chronic)

The final experiments performed in Chapter 4 suggest that cell density at the electrode increases from day 3 through 11, but are unable to determine if there is an increase in cell density beyond this. This indicates that the tested 3D culture, models the acute inflammatory response, but not necessarily chronic. It also suggests that factors responsible for the chronic inflammatory response may not present in our model. Although this model can be used as is to investigate methods for mitigating the acute glial response to an electrode, it would be beneficial to determine if it also models the chronic inflammatory response and/or which factors lead to the chronic response. A series of next steps for establishing the acute vs chronic response in the model are suggested below.

5.4.1 Quantify Cell Density

Cell density at the electrode interface is related to the progress of glial scarring. In literature this progression is classified as the acute inflammatory response, glial scarring and the chronic inflammatory response. The acute inflammatory response is characterized by the initial reaction of microglia and astrocytes to the electrode. This initial response of microglia and astrocytes to an inserted electrode was observed in Figures 4.13 and 4.14. A persistent increase in glial scarring for an extended period of time is characterized as a chronic inflammatory response. And increasing cell density surrounding the electrode (up to 500 μm from the electrode surface) over several weeks to months is often used to determine the extent of the chronic inflammatory response and glial scarring. In Figures 4.13 and 4.14 it was difficult to determine if there was an increase in cell density after 6 days post electrode insertion and therefore it was difficult to determine if the chronic inflammatory response was being modeled. Quantifying cell density over time would confirm the degree of glial scarring in the model (acute or chronic response). However, due to 3D nature of the gel, light diffraction and layered cells make it difficult to quantify the cellular response. Confocal imaging would allow a single plane to be analyzed without confounding light from other planes. This technique paired with nuclei labeling (similar to that in Section 3.3) would facilitate quantification of the cellular response and verify any increase, decrease or plateau in cell number at the electrode. This data, together with the temporal response

would clarify if the current model is limited to the acute inflammatory response or if there is a chronic response that was just not obvious from the qualitative study.

5.4.2 Consider Additional Factors Contributing to Glial Scarring

The glial scarring model proposed in this thesis has many factors missing that would normally be present during *in vivo* trials. The absence of these factors may limit the extent of glial scarring resulting in only acute glial scarring. Integrating these factors into the model may allow not only acute, but also chronic glial scarring to be analyzed.

For example, there is no breach of the BBB and therefore, no external cells or clotting factors introduced during insertion. As a result, many of the inflammatory factors infiltrating macrophages present after electrode insertion *in vivo* are not present in the 3D model. These factors include pro-inflammatory cytokines, growth factors and ATP. Polikov et al demonstrated the necessity of Neurobasal media with B27 and bFGF supplements for consistent glial scarring *in vitro* [11]. In another study, Polikov et al. also investigated the effects of soluble factors on the extent of glial scarring [66]. This study indicated that the pro-inflammatory cytokines IL-1α, IL-1β as well as the growth factors PDGF and BMP-2 significantly increased the extent of glial scarring [66]. Another factor known to activate microglia is ATP, which is released from injured or dying cells (as would occur when an electrode is inserted into the CNS) [143, 144].

In addition to chemical factors, mechanical motion may also play a significant role in glial scarring. Our actions throughout the day as well as internal motion due to blood flow and respiration result in mechanical stresses and strains being continuously applied to CNS tissue [17]. Strain as a result of daily motion was determined to be between 2 to 30 μm in rodent cortex [17]. Due to mechanical mismatch between the electrode and CNS tissue, the electrode does not move or deform with these daily movements. *In vivo* models predominantly fix electrodes to the bone after insertion to ensure that they remain in place (Table 1.1). As the electrode is held in place, the tissue moves separately causing compression, expansion and even tearing of the tissue [17]. Untethered electrodes have been

shown to improve mechanical mismatch to a certain degree and therefore decrease the degree of glial scarring [31]. Stagnant media surrounds the 3D glial scarring model developed in Chapter 4 with little mechanical force being applied to the scaffold. The electrode is also unfixed and free to move with any movement during media changes. The addition of micromotion to the model may lead to chronic glial scarring. This could be achieved by adding motion to the entire system (culture plate on a shaker), deforming the scaffold, or moving the electrode during culture in a controlled manner.

A combination of chemical and mechanical cues is likely required to model the chronic inflammatory response to an electrode. Systematic manipulation of these factors while quantifying the glial response would provide valuable information regarding the degree to which various factors contribute to glial scarring.

5.5 Electrode Design

The primary reason for creating a 3D *in vitro* model of glial scarring is to improve electrode functionality. Many electrode parameters have been suggested as contributors to glial scarring including size, geometry, coating, stiffness, fixation method and surface roughness. The model may be used to determine the relative significance of each of these parameters. Once the chemical and mechanical factors contributing to glial scarring have been determined, they can be used to mitigate and guide the glial scarring response. Contributing factors or electrode properties modulating glial scarring can then be integrated into electrode design. In parallel, existing electrode designs may be compared in a high-throughput consistent fashion to determine which design is optimal for various regions of the CNS.

5.6 Conclusions

Electrode biocompatibility with the CNS is holding back clinical implementation and advancement of neural prostheses. To be considered for clinical use, electrodes must remain functional over many decades. Glial scarring involving microglia and astrocytes in the CNS is believed to be a major contributor to loss of electrode

function. Although the cellular response involving microglia and astrocytes has been well documented, current *in vivo* models are complex and time consuming making it difficult to determine the exact degree to which different electrode parameters influence glial scarring. To pin point which factors have the most impact on glial scarring a new high-throughput 3D culture model is required. To allow testing of various electrode parameters, the model was designed to support glial cells (microglia and astrocytes) with a floating microwire for a period of several weeks as well as mimic the mechanical properties of CNS tissue. The developed model consisted of a HAMA based scaffold. Aqueous HAMA, microglia and astrocytes were mixed with precursors then exposed to green LED light to initiate crosslinking. Once crosslinked, an insoluble gel with a homogenous distribution of microglia and astrocytes was created. This 3D culture was then used to model glial scarring. Model design and development took place in three parts; gel synthesis and characterization (Chapter 2), preliminary 2D culture (Chapter 3) and cell-gel integration (Chapter 4). Conclusions from each of these parts are detailed below.

Hyaluronic acid was chosen as a scaffold due to its reported cytocompatibility and ability to be easy functionalized for photocrosslinking. Once functionalized to create HAMA, HA may be crosslinked in the presence of LED light and precursors to form an insoluble gel scaffold. The synthesis of HAMA was standardized and upscaled to yield an average of 420.60 ± 50.03 mg each time. The average percent modification was verified with NMR and determined to be 94.48 ± 10.56 mg each time. This amount of macromer can create a maximum of 84.12 mL at 0.5 wt% (~841 gels) and a minimum of 28.04 mL at 1.5 wt% (~280 gels) of crosslinked HAMA gel. Green LED light along with lower precursor concentrations (0.1 % (w/v) TEA, 0.1 % (w/v) NVP and 0.01 mM EY) was chosen over UV light for crosslinking to reduce cell death during photoencapsulation. A high-throughput photocrosslinking system was developed to allow easy and sterile cell encapsulation of 24 gels in parallel. This system included PDMS molds to control gel shape, an acrylic holding mold for easy transfers and an LED enclosure. Glass coverslips coated in PLL were shown to sufficiently attach HAMA gels to glass to allow media changes and electrode insertion without loss of gels. Once the photocrosslinking system was established, mechanical properties of the gel were investigated. Increasing macromer weight

fraction (0.5 to 1.5 wt%) was shown to modify storage modulus between 3-130 Pa. These values were then compared to a sample of adult rat brain tested under identical conditions. The storage modulus of adult rat brain was found to be between 32 – 90 Pa, within the tunable range of HAMA storage modulus. Gel porosity was assessed to determine if the HAMA gel is sufficiently porous to enable cell survival and growth at all weight fractions tested. CryoSEM indicated that all weight fractions (0.5 to 1.5 wt%) were porous. Although SEM images did not reveal any significant change in pore size between weight fractions, equilibrium swelling ratio did. As macromer weight fraction increased, the equilibrium swelling ratio decreased, which has been correlated with decreasing pore size in hydrogel materials. Finally, the degree of swelling after crosslinking (equilibrium swelling percent) was investigated. As no significant difference for equilibrium swelling percent was observed, it was concluded that all gel undergo experience similar forces due to swelling after crosslinking. Together these results demonstrate a high-throughput method for the synthesis and photocrosslinking of a porous scaffold that may be used for cell encapsulation.

Microglia and astrocytes are the primary contributors to glial scarring in the CNS and were therefore the cells of interest in the developed model. Before microglia and astrocytes were encapsulated in the HAMA gel, they were isolated from whole CNS tissue. Both the spinal cord and brain of day 1 neonatal Sprague-Dawley rat pups were considered as a source of mixed glia. Microglia and astrocytes were successfully isolated from both the spinal cord and brain. However, the low yield and therefore plating density of spinal cord made it an impractical cell source for gel encapsulation. Brain tissue yielded 25 times more cells than spinal cord tissue. As a result, only brain tissue was used in further experiments. After isolation, mixed glia cells were characterized to determine how the isolation process affected cell morphology. Both protoplasmic and fibrous astrocytes were identified. Microglia appeared in a rounded morphology indicative of an activated state (common in 2D culture). Glial response to an electrode was also tested before moving to the 3D model to ensure that glial cells were still capable of migrating to/or proliferating at an electrode after isolation. DAPI labeling of cell nuclei showed a significant increase in cell density at an electrode interface over 14 days. Immuno labeling revealed

microglia arriving first at the electrode (~1 day) with astrocytes responding later (~4 days). These results are in agreement with previous *in vivo* and *in vitro* studies of the temporal inflammatory response, indicating that cells still respond to foreign bodies after isolation [17]. These preliminary 2D culture studies standardized microglia and astrocyte isolation from whole brain tissue. The results found in 2D were later compared to those in 3D to assess the effects of encapsulation and a 3D environment on cell morphology and behavior.

The final stage of model development involved the integration of microglia and astrocytes from Chapter 3 with the HAMA gel developed in Chapter 2. At an initial seeding density of $1x10^6$ cells/mL, a limited number of viable cells were observed in the HAMA gel. When cell density was increased to $1x10^7$ cells/mL, cell viability also increased from ~50 to 80 % one day post encapsulation. The highest seeding density tested, $1x10^7$ cells/mL, demonstrated the most consistent cell viability and was therefore used for all future encapsulations. Microglia and astrocytes were also characterized in the HAMA gels to observe morphology and compare it to that observed in 2D cultures. Astrocytes in the gel appeared with a stellate morphology similar to that seen in other 3D cultures and the protoplasmic morphology observed in 2D. Microglia in the 3D cultures were observed with both an amoeboid and ramified morphology indicative of activated and ramified states respectively. This was contrasting to microglia in 2D, which appeared predominantly amoeboid. Once viable cultures were established in HAMA gels, the effect of macromer weight fraction (for the purposes of altering gel stiffness) was analyzed. Cell viability was found to be consistent across all weight fractions tested (0.5, 0.75 and 1.0 wt%) except 1.5 wt%. The 1.5 wt% gel had significantly lower cell viability. This viability was recovered slightly over 7 days, but never reached that of the other weight fractions. This is likely due to the changing gel structure observed in Chapter 2. Increasing wall thickness likely affects nutrient diffusion through the gel and the cells ability to break down and modify the HAMA matrix that may in turn effect cell viability. Next the feasibility of using the HAMA gel-cell system as a model of glial scarring was assessed. An electrode inserted over 7 days was stable through media changes and labeling. Both microglia and astrocytes were observed at the electrode interface after 7 days, appearing to line the electrode in a manner similar to that of

glial scarring. The temporal response of microglia and astrocytes was studied over 21 days. Microglia appeared first at the electrode (~3 days) and astrocytes appeared shortly after (~6 days). Though these times points were slightly later than those seen in 2D, it is still within the reported range for cellular responses *in vivo*. The delayed response may be due to limited migration through the gel, limited diffusion of signaling factors through the matrix or the less activated state that the cells are in during 3D culture. This initial response to the electrode demonstrated successful modeling of the acute inflammatory response in the 3D model. However, it could not be determined if cell density continued to increase, as is characteristic of chronic inflammatory response. This implies that the model may require additional factors (chemokines, growth factors, etc.) that are not present *in vitro*, but are present *in vivo* to establish a model of the chronic inflammatory response. This scaffold may be used to test the acute response of microglia and astrocytes to an electrode as well as other studies of mixed glial cultures where a 3D structure is beneficial (drug and migration assays).

REFERENCES

1. Information, C.I.f.H., *The burden of neurological diseases, disorders and injuries in Canada*. 2007.
2. Farry, A. and D. Baxter. *The Incidence and Prevalence of Spinal Cord Injury in Canada*. Rick Hansen Institute 2010.
3. Kim, G.B., P. Fattahi, and M.R. Abidian, *Electrode-neural tissue interactions: Immune responses, current technologies, and future directions*, in *Biomaterials Surface Science*, A. Taubert, J.F. Mano, and J.C. Rodriguez-Cabello, Editors. 2013.
4. Chestek, C.A., et al., *Neural prosthetic systems: Current problems and future directions.* 31st Annual International Conference of the IEEE EMBs, 2009.
5. Tudor, M., L. Tudor, and K.I. Tudor, *Hans Berger (1873-1941)- the history of electroencephalography.* Acta Medica Croatica, 2005. **59**(4): p. 307- 313.
6. Fetz, E.E., *Operant conditioning of cortical unit activity.* Science, 1969. **163**: p. 955-958.
7. Hochberg, L.R., et al., *Reach and grasp by people with tetraplegia using a neurally controlled robotic arm.* Nature, 2012. **485**: p. 372-375.
8. Holinski, B.J., et al., *Restoring stepping after spinal cord injury using intraspinal microstimulation and novel control strategies.* 33rd Annual International Conference of the IEEE EMBS, 2011.
9. Moxon, K.A., et al., *Long-term recordings of Multiple, Single-Neurons for Clinical Applications: The Emerging Role of the Bioactive Microelectrode.* Materials, 2009. **2**: p. 1762-1794.
10. Ware, T., et al., *Smart polymer for neural interfaces.* Polymer Reviews, 2013. **53**: p. 108-129.
11. Polikov, V.S., et al., *In vitro model of glial scarring around neuroelectrodes chronically implanted in the CNS.* Biomaterials, 2006. **27**: p. 5368-5376.
12. Hochberg, L.R., et al., *Neuronal ensemble control of prosthetic devices by a human with tetraplegia.* Nature, 2006. **442**: p. 164-171.
13. Chestek, C.A., et al., *Long-term stability of neural prosthetic control signals from silicon cortical arrays in rhesus macaque motor cortex.* Journal of Neural Engineering, 2011. **8**.
14. Suner, S., et al., *Reliability of signals from a chronically implanted, silicon-based electrode array in non-human primate primary motor cortex.* IEEE Transactions on Neural Systems and Rehabilitation Engineering, 2005. **13**(4): p. 524-541.
15. Polikov, V.S., P.A. Tresco, and W.M. Reichert, *Response of brain tissue to chronically implanted neural electrodes.* Journal of Neuroscience Methods, 2005. **148**: p. 1-18.
16. Gao, Z., et al., *Reciprocal modulation between microglia and astrocyte in reactive gliosis following the CNS injury.* Molecular Neurobioogy, 2013.
17. He, W. and R.V. Bellamkonda, *A molecular perspective on understanding and modulating the performance of chronic central*

nervous system recording electrodes, in *Indwelling Neural Implants: Strategies for Contending with the In Vivo Environment*. 2008.
18. He, B., et al., *Grand challenges in interfacing engineering with life sciences and medicine.* IEEE Transactions on Biomedical Engineering, 2013. **60**(3).
19. Bryers, J.D., C.M. Giachelli, and B.D. Ratner, *Engineering Biomaterials to Integrate and Heal: The Biocompatibility Paradigm Shifts.* Biotechnology and Bioengineering, 2012. **109**(8): p. 1898-1911.
20. Anderson, J.M., *Biological Responses to Materials.* Annual Reviews of Material Research, 2001. **31**: p. 81-110.
21. Anderson, J.M., A. Rodriguez, and D.T. Chang, *Foreign Body Reaction to Biomaterials.* Seminars in Immunology, 2008. **20**: p. 86-100.
22. Khandwekar, A. and C.K. Rho, *Modulation of Cellular Responses on Engineered Polyurethant Implants.* Journal of Biomedical Materials Research 2012. **100 A**: p. 2211-2222.
23. Hanisch, U.K., *Microglia as a source and target of cytokines.* Glia, 2002. **40**: p. 140-155.
24. Ohsawa, K. and S. Kohsaka, *Dynamic motility of microglia: Purinergic modulation of microglial movement in the normal and pathological brain.* Glia, 2011. **59**: p. 1793-1799.
25. Zhong, Y. and R.V. Bellamkonda, *Biomaterials for the central nervous system.* Journal of the Royal Society Interface, 2008. **5**: p. 957-975.
26. Sofroniew, M. and H. Vinters, *Astrocytes:: biology and pathology.* Acto Neuropathologica, 2010. **119**: p. 7-35.
27. Landis, D.M.D., *The early reaction of non-neuronal cells to brain injury.* Annual Review of Neuroscience, 1994(17): p. 133-151.
28. Stroncek, J.D. and W.M. Reichert, *Overview of wound healing in different tissue types*, in *Indwelling Neural Implants: Strategies for Contending with the In Vivo Environment*, W.M. Reichert, Editor. 2008, CRC Press: Boca Raton.
29. Inc., M. *Deep brain stimulation for movement disorders*. 2013 [cited 2013 October 29].
30. Kumar, K., C. Toth, and R. Nath, *Deep brain stimulation for intractable pain: A 15-year experience.* Neurosurgery, 1997. **40**(4): p. 736-747.
31. Thelin, J., et al., *Implant size and fixation mode strongly influence reaction in the CNS.* PlosOne, 2011. **6**(1).
32. Lind, G., et al., *Multiple implants do not aggravate the tissue reaction in rat brain.* PlosOne, 2012. **7**(10).
33. Szarowski, D.H., et al., *Brain responses to micro-machined silicon devices.* Brain Research, 2003. **983**: p. 23-35.
34. Biran, R., D.C. Martin, and P.A. Tresco, *The brain tissue response to implanted silicon microelectrode arrays is increased when the device is tethered to the skull.* Journal of Biomedical Materials Research, 2007. **82**: p. 169-178.

35. Spataro, L., et al., *Dexamethasone treatment reduces astroglia responses to inserted neuroprosthetic devices in rat neocortex.* Experimental Neurology, 2005. **194**: p. 289-300.
36. He, W., et al., *A novel anti-inflammatory surface for neural electrodes.* Advanced Materials, 2007. **19**: p. 3529-3533.
37. Azemi, E., C.F. Lagenaur, and X.T. Cui, *The surface immobilization of the neural adhesion molecule L1 on neural probes and its effect on neuronal density and gliosis at the probe/tissue interface.* Biomaterials, 2011. **32**: p. 681-692.
38. Cheng, X., et al., *Platinum wire implants coated with PEDOT/carbon nanotube conducting polymer films in the brain of rats: A histological evaluation.* Journal of Wuhan University of Technology - Materials Science Edition, 2013. **27**(6): p. 1053-1057.
39. Kozai, T.D.Y., et al., *In vivo two-photon microscopy reveals immediate microglial reaction to implantation of microelectrode through implantation of microelectrode through extension of processes.* Journal of Neural Engineering, 2012. **9**.
40. Misra, A., et al., *Preventing neuronal damage and inflammation in vivo during cortical microelectrode implantation through the use of poloxamer P-188.* Journal of Neural Engineering, 2013. **10**.
41. Woolley, A.J., H.A. Desai, and K.J. Otto, *Chronic intracortical microelectrode arrays induce non-uniform, depth related tissue responses.* Journal of Neural Engineering, 2013. **10**.
42. Markwardt, N.T., J. Stokol, and R.L.R. II, *Sub-meninges implantation reduces immune response to neural implants.* Journal of Neruoscience Methods, 2013. **214**: p. 119-125.
43. Davis, T.S., et al., *Spatial and temporal characteristics of V1 microstimulation during chronic implantation of a microelectrode array in a behaving macaque.* Journal of Neural Engineering, 2012. **9**.
44. Prasad, A. and J.C. Sanchez, *Quantifying long-term microelectrode array functionality using chronic in vivo impedance testing.* Journal of Neural Engineering, 2012. **9**: p. 1741-2560.
45. Kolarcik, C.L., et al., *In vivo effects of L1 coating on inflammation and neuronal health at the electrode-tissue interface in rat spinal cord and dorsal root ganglion.* Acta Biomaterialia, 2012. **8**: p. 3561-3575.
46. Potter, K.A., et al., *Stab injury and device implantation within the brain results in inversely multiphasic neuroinflammatory and neurodegenerative responses.* Journal of Neural Engineering, 2012. **9**.
47. Harris, J.P., et al., *Mechanically adaptive intracortical implants improve the proximity of neuronal cell bodies.* Journal of Neural Engineering, 2011. **8**.
48. Welenhuysen, M., et al., *Effect of insertion speed on tissue response and insertion mechanics of a chronically implanted silicon-based beural probe.* IEEE Transactions on Biomedical Engineering, 2011. **58**(11): p. 3250-3259.

49. Hassler, C., et al., *Chronic intracortical implantation of saccharose-coated flexible shaft electrode into the cortex of rats.* 3rd Annual International Conference of the IEEE EMBS, 2011.
50. Bamford, J.A., K.G. Todd, and V.K. Mushawar, *The effects of intraspinal microstimulation on spinal cord tissue in rat.* Biomaterials, 2010. **31**: p. 5552-5563.
51. Winslow, B.D. and P.A. Tresco, *Quantitative analysis of the tissue response to chronically implanted microwire electrodes in rat cortex.* Biomaterials, 2010. **31**: p. 1558-1567.
52. McConnell, G.C., et al., *Implanted neural electrodes cause chronic, local inflammation that is correlated with local neurodegeneration.* Journal of Neural Engineering, 2009. **6**.
53. Chen, Y.-Y., et al., *Design and fabrication of a polyimide-based microelectrode array: Application in neural recording and repeatable electrolytic lesion in rat brain.* Journal of Neuroscience Methods, 2009. **182**: p. 6-16.
54. Stice, P. and J. Muthuswamy, *Assessment of gliosis around moveable implants in the brain.* Journal of Neural Engineering, 2009. **6**.
55. Leung, B.K., et al., *Characterization of microglial attachment and cytokine release on biomaterials of differing surface chemistry.* Biomaterials, 2008. **29**: p. 3289-3297.
56. Yeager, J.D., et al., *Characterization of flexible ECoG electrode arrays for chronic recording in awake rats.* Journal of Neuroscience Methods, 2008. **173**: p. 279-285.
57. Mercanzini, A., et al., *Demonstration of cortical recording and reduced inflammatory response using flexible polymer neural probes.* IEEE MEMS, 2007: p. 573-576.
58. Zhong, Y. and R.V. Bellamkonda, *Dexamethasone-coated neural probes elicit attenuated inflammatory response and neuronal loss compared to uncoated neural probes.* Brain Research, 2007. **1148**: p. 15-27.
59. Rennaker, R.L., et al., *Minocycline increases quality and longevity of chronic neural recordings.* Journal of Neural Engineering, 2007. **4**: p. L1-L5.
60. Griffith, R.W. and D.R. Humphrey, *Long-term gliosis around chronically implanted platinum electrodes in the Rhesus Macaque motor cortex.* Neuroscience Letters, 2006. **406**: p. 81-86.
61. Biran, R., D.C. Martin, and P.A. Tresco, *Neuronal cell loss accompanies the brain tissue response to chronically implanted silicon microelectrode arrays.* Experimental Neurology, 2005. **195**: p. 115-126.
62. Moxon, K.A., et al., *Ceramic-based multisite electrode arrays for chronic single-neuron recording.* IEEE Transactions on Biomedical Engineering, 2004. **51**(4).
63. Yuen, T.G.H., W.F. Agnew, and L.A. Bullara, *Tissue response to potential neuroprosthetic materials implanted subdurally.* Biomaterials, 1986. **8**: p. 138-141.

64. Xiao, Y., et al., *Surface modification of neural probes with conducting polymer poly(hydroxymethylated-3,3-ethylenedioxythiophene) and its biocompatability.* Applied Biochemistry and Biotechnology, 2006. **128**.
65. Polikov, V.S., et al., *Control protocol for robust in vitro glial scar formation around microwires: essential roles of bFGF and serum in gliosis.* Journal of Neuroscience Methods, 2009. **181**: p. 170-177.
66. Polikov, V.S., J.-S. Hong, and W.M. Reichert, *Soluble factor effects on glial cell reactivity at the surface of gel-coated microwires.* Journal of Neruoscience Methods, 2010. **190**: p. 180-187.
67. Achyuta, A.K.H., et al., *Biocompatability assessment of insulating silicone polymer coatings using an in vitro glial scar assay.* Macrocolecular Bioscience, 2010. **10**: p. 872-880.
68. Page, H., P. Flood, and E.G. Reynaud, *Three-dimensional tissue cultures: current trends and beyond.* Cell Tissue Research, 2013. **352**: p. 123-131.
69. Breslin, S. and L. O'Driscoll, *Three-dimensional cell culture: the missing link in drug discovery.* Drug Discovery Today, 2012. **18**(5/6): p. 240-249.
70. Gurski, L.A., et al., *3D matrices for anti-cancer drug testing and development.* Oncology Issues, 2010: p. 20-25.
71. Baker, B.M. and C.S. Chen, *Deconstructing the third dimension - how 3D culture microenvironments alter cellular cues.* Journal of Cell Science, 2012. **125**: p. 3015-3024.
72. Hachet, E., et al., *Design of biomimetic cell-interactive substrates using hyaluronic acid hydrogels with tunable mechanical properties.* BioMacromolecules, 2012. **13**: p. 1818-1827.
73. Rehfeldt, F., et al., *Hyaluronic acid matrices show matrix stiffness in 2D and 3D dictates cytoskeletal order and myosin-II phosphorylation within stem cells.* Integrative Biology, 2012. **4**: p. 422-430.
74. Ereifej, E.S., et al., *Examining the inflammatory response to nanopatterned polydimethylsiloxan using organotypic brain slice methods.* Journal of Neuroscience Methods, 2013. **217**: p. 17-25.
75. Cullen, D.K., C.M. Simon, and M.C. LaPlaca, *Strain rate-dependant induction of reactive astrogliosis and cell death in three-dimensional neural-astrocytic co-cultures.* Brain Research, 2007. **1158**: p. 103-115.
76. Frampton, J.P., et al., *Fabrication and optimization of alginate hydrogel constructs for use in 3D neural cell culture.* Biomedical Materials, 2011. **6**: p. 1-18.
77. Frampton, J.P., et al., *Effects of glial cells on electrode impedance recorded from neural prosthetic devices in vitro.* Annals of Biomedical Engineering, 2010. **38**(3).
78. Novak, U. and A.H. Kaye, *Extracellulat matrix and the brain: componets and function.* Journal of Clinical Neuroscience, 2000. **7**(4): p. 280-290.
79. Cheng, S., E.C. Clake, and L.E. Bilston, *Rheological properties of the tissues of the central nervous systen: A review.* Medical Engineering and Physics, 2008: p. 1318-1337.

80. Smejkalova, D., et al., *Structural and conformation differences of acrylated hyaluronan modified in protic and aprotic solvent system.* Carbohydrate Polymers, 2012. **87**: p. 1460-1466.
81. Outasti, S., et al., *The CD44/integrins interplay and the significance of receptor binding and re-presentation in the uptake of RGD-fuctionalized hyaluronic acid.* Biomaterials, 2012. **33**: p. 1120-1134.
82. Collins, M.N. and C. Birkinshaw, *Comparison of the effectiveness of four different crosslinking agents with hyaluronic acid hydrogel films for tissue-culture application.* Journal of Applied Polymer Science, 2007. **104**: p. 3183-3191.
83. Ananthanaraynan, B., Y. Kim, and S. Kumar, *Elucidating the mechanobiology of malignant brain tumors using a brain matrix-mimetic hyaluronic acid hydrogel platform.* Biomaterials, 2011. **32**: p. 7913-7923.
84. Seidlits, S.K., et al., *The effects of hyaluronic acid hydrogels with tunable mechanical properties on neural progenitor cell differentiation.* Biomaterials, 2010. **31**: p. 3930-3940.
85. Bencherif, S.A., et al., *Influence of the degree of methacrylation on hyaluronic acid hydrogels properties.* Biomaterials, 2008. **29**: p. 1739-1749.
86. LaPlaca, M.C., et al., *Three-dimensional neuronal cultures*, in *Methods in Bioengineering: 3D Tissue Engineering*, F. Berthiaume and J. Morgan, Editors. 2010, Artech House Publishers: London.
87. Smeds, K.A. and M.W. Grinstaff, *Photocrosslinkable polysaccharides for in situ hydrogel formation.* Journal of Biomedical Materials Research, 2001. **54**: p. 115-121.
88. Seidlits, S.K., et al., *The effects of hyaluronic acid hydrogels with tunable mechanical properties on neural progenitor cell differentiation.* Biomaterials, 2010. **31**: p. 3930-3940.
89. Leach, J.B., et al., *Photocrosslinked hyaluronic acid hydrogels: natural, biodegradable tissue engineering scaffolds.* Biotechnology and Bioengineering, 2002. **82**(5): p. 578-589.
90. Naghash, H.J., O. Okay, and Y. Yagci, *Gel formation by chain-crosslinking photopolymerization of methyl methacrylate and ethylene glycol dimethacrylate.* Polymer, 1997. **38**(5): p. 1187-1196.
91. Nettles, D.L., et al., *Photocrosslinkable Hyaluronan as a Scaffold for Articular Cartilage Repair.* Annals of Biomedical Engineering, 2004. **32**(3): p. 391-397.
92. Oudshoorn, M.H.M., et al., *Synthesis of methacrylated hyaluronic acid with tailored degree of substitution.* Polymer, 2007. **48**: p. 1915-1920.
93. Sigma-Aldrich. *Methacrylic acid*. 2013 [cited 2013 October 15, 2013].
94. Bian, L., et al., *The influence of hyaluronic acid hydrogel crosslinking density and macromolecular diffusivity on human MSC chondrogenesis and hypertrophy.* Biomaterials, 2013. **34**: p. 413-421.

95. Mouret, S., A. Forestier, and T. Douki, *The specificity of UVA-induced DNA damage in human malnocytes.* Photochemical and Photobiological Sciences, 2012. **11**(15): p. 155-162.
96. Russo, A., et al., *Genestin inhibits UV light-induced plasmid DNA damage and cell growth in human melanoma cells.* Journal of Nutritional Biochemistry, 2006. **17**: p. 103-108.
97. Sander, C.S., et al., *Role of oxidative stress and the antioxidant network in cutaneous carcinogenisis.* International Journal of Dermatology, 2004. **43**: p. 326-335.
98. Bahney, C.S., et al., *Visible light photoinitiation of mesenchymal stem cell-laden bioresponsive hydrogels.* European Cells and Materials, 2011. **22**: p. 43-55.
99. Chow, A., *Developing three-dimensional hydrogel cell scaffolds to assess the biocompatability of intraspinal microstimulation electrodes*, A. Elias, Editor. 2011, University of Alberta.
100. Bryant, S.J. and K.S. Anseth, *Photopolymerization of Hydrogel Scaffolds.*
101. Haycock, J.W., *3D Cell Culture: A Review of Current Approaches and Techniques*. Methdos in Molecular Biology. Vol. 695. 2011: Springer Protocols.
102. Erickson, I.E., et al., *Macromer density influences mesenchymal stem cell chrondrogenesis and maturation in photocrosslinkes hyaluronic acid hydrogels.* Osteoarthritis and Cartilage, 2009. **17**: p. 1639-1648.
103. Bilston, L.E., *Brain Tissue Mechanical Properties*, in *Studies in Mechanobiology, Tissue Engineering and Biomaterials*, A. Gefen and R. Aviv, Editors. 2011, Springer. p. 11-24.
104. Clarke, E.C., *Spinal Cord Mechanical Properties*, in *Studies in Mechanobiology, Tissue Engineering and Biomaterials*, A. Gefen and R. Aviv, Editors. 2011, Springer.
105. Discher, D.E., D.J. Mooney, and P.W. Zandstra, *Growth factors, matrices, and forces combine and control stem cells.* Science, 2009. **324**: p. 1673-1677.
106. Flanagan, L.A., et al., *Neurite branching on deformable substrates.* Developmental Neuroscience, 2002. **13**(18): p. 2411-2415.
107. Hrapko, M., et al., *The influence of test conditions on characterization of the mechnical properties of brain tissue.* Journal of Biomechanical Engineering, 2008. **130**.
108. Prange, M.T. and S.S. Margulies, *Regional, directional, and age-dependant properties of the brain undergoing large deformation.* Transaction of the ASME, 2002. **124**: p. 244-252.
109. Fallenstein, G.T. and V.D. Hulce, *Dynamic mechanical properties of human brain tissue.* Journal of Biomechanics, 1969. **2**: p. 217-226.
110. Camci-Unal, G., et al., *Synthesis and characterization of hybrid hyaluronic acid-gelatin hydrogels.* BioMacromolecules, 2013. **14**: p. 1085-1092.

111. Bruck, S.D., *Aspects of Three Types of Hydrogels for Biomedical Applications.* Journal of Biomedical Materials Research, 1973. **7**: p. 387-404.
112. Ganji, F., S. Vasheghani-Farahani, and E. Vasheghani-Farahani, *Theoretical description of hydrogel swelling: A review.* Iranian Polymer Journal, 2010. **19**(5): p. 375-398.
113. Collins, M.N. and C. Birkinshaw, *Physical properties of crosslinked hyaluronic acid hydrogels.* Journal of Material Science: Materials Methods, 2008. **19**: p. 3335-3343.
114. Boche, D., V.H. Perry, and J.A.R. Nicoll, *Review: Activation patterns of microglia and their identification in the human brain.* Neuropathology and Applied Neurobiology, 2013. **39**: p. 3-18.
115. Yip, P., et al., *Rapid isolation and culture of primary microglia from adult mouse spinal cord.* Journal of Neuroscience Methods, 2009. **183**: p. 223-237.
116. Beggs, S. and M. Salter, *Stereological and somatotopic analysis of the spinal microglial response to peripheral nerve injury.* Brain, Behaviour and Immunity, 2007: p. 624-633.
117. Gibbons, H. and M. Dragunow, *Adult human brain cell culture for neuroscience research.* The International Journal of Biochemistry and Cell Biology, 2010. **42**: p. 844-856.
118. Danielyan, L., et al., *Keratinocytes as depository of ammonium-inducible glutamine synthetase: age- and anatomy-dependant distribution in human and rat skin.* PlosOne, 2009. **4**(2): p. 1-13.
119. Davidoff, M.S., et al., *Leydig cells of the human testis possess astrocyte and oligodendrocyte marker molecules.* Acta Histochemica, 2002. **104**(1): p. 30-49.
120. Miyako, H., et al., *Phenotypes of articular disc cells in the rat tempromandibular joint as demonstrated by immunohistochemistry for nestin and GFAP.* Journal of Anatomy, 2011. **219**: p. 472-480.
121. Apte, M.V., et al., *Periacinar stellate shaped cells in rat pancreas: identification, isolation, and culture.* Gut, 1998. **43**: p. 128-133.
122. Probes, M. *DAPI Nucleic Acid Stain*. 2006 [cited 2011 December 11]; Available from: http://probes.invitrogen.com/media/pis/mp01306.pdf.
123. Schneider, C.A., W.S. Rasband, and K.W. Eliceiri, *NIH Image to ImageJ: 25 years of image analysis.* Nature Methods, 2012. **9**(7): p. 671-675.
124. Fujita, T., et al., *Cellular dynamics of macrophages and microglial cells in reaction to stab wounds in rat cerebral cortex.* Acta Neurochirurgica, 1998. **140**: p. 275-279.
125. Saura, J., J.M. Tusell, and J. Serratosa, *High-yield isolation of murine microglia by mild trypsinization.* Glia, 2003. **44**: p. 183-189.
126. Bjornsson, C.S., et al., *Associative image analysis: A method for automated quantification of 3D multi-parameter images of brain tissue.* Journal of Neurscience Methods, 2008. **170**: p. 165-178.

127. Yavin, E. and D.M. Billia, *Apoptotic death in cerebral hemisphere cells is density dependant and modulated by transient oxygen and glucose deprivation.* Journal of Neuroscience Research, 1997. **47**: p. 471-478.
128. Bos, C.v.d., et al., *p21 cip1 rescues human mesenchymal stem cells from apoptosis induced by low-density culture.* 293, 1998: p. 463-470.
129. Stephan, S., W.E. Johnson, and S. Roberts, *The influence of nutrient supply and cell density on the growth and survival of intervertebral disc cell sin 3D culture.* European Cells and Materials, 2011. **22**: p. 97-108.
130. Morrison, B., D.K. Cullen, and M. LaPlaca, *In vitro models for biomechanical studies of neural tissues.* Studies in mechanobiology, tissue engineering and biomaterials, 2011. **3**: p. 247-285.
131. East, E., J.P. Golding, and J.B. Phillips, *Engineering an integrates cellular interface in three-dimensional hydrogel cultures permits monitoring of reciprocal astrocyte and neuronal responses.* Tissue Engineering, 2012. **18**(7).
132. Pelvig, D.P., et al., *Neocortical glial cell numbers in human brains.* Neurobiology of Aging, 2008. **29**: p. 1754-1762.
133. East, E., J.P. Golding, and J.B. Phillips, *A versatile 3D culture model facilitates monitoring of astrocytes undergoing reactive gliosis.* Journal of Tissue Engineering and Regenerative Medicine, 2009. **3**: p. 634-646.
134. Br*ännvall,* K., et al., *Enhanced neuronal differentiation in a three-dimensional collagen-hyaluronana matrix.* Journal of Neuroscience Research, 2007. **85**: p. 2138-2146.
135. Butt, A.M., et al., *Three-dimensional morphology of astrocytes and oligodendrocytes in the intact mouse optic nerve.* Journal of Neurocytology, 1994. **23**: p. 469-485.
136. Young, B., et al., *Wheater's Functional Histology: A Text and Colour Atlas*. Fifth Edition ed. 2006, Glasgow, Nottingham: Elsevier.
137. Guzman, R.C.d., et al., *Alginate-matrigel microencapsulated schwann cells for inducible secretion of glial cell line derived neurotrophic factor.* Journal of Microencapsulation, 2008. **25**(7): p. 487-498.
138. Mironi-Harpaz, I., et al., *Photopolymerization of cell-encapsulation hydrogels: Crosslinking efficiency versus cytotoxicity.* Acta Biomaterialia, 2012. **8**: p. 1838-1848.
139. Wang, X., et al., *Hyaluronic acid-based scaffold for central neural tissue engineering.* Interface Focus, 2012. **2**: p. 278-291.
140. Engler, A.J., et al., *Matrix elasticity directs stem cell lineage specification.* Cell, 2011. **126**: p. 677-689.
141. Eng, D., et al., *Hyaluronan scaffolds: a balance between backbone functionalization and bioactivity.* Acta Biomaterialia, 2010. **6**: p. 2401-2414.
142. Pettikiriarachchi, J.T.S., et al., *Biomaterials for brain tissue engineering.* Austrailian Journal of Chemistry, 2010. **63**: p. 1143-1154.
143. Yenari, M.A., T.M. Kauppinen, and R.A. Swanson, *Microglia activation in stroke: Therapeutic targets.* The American Society for Expeirmental NeuroTherapeutics, 2010. **7**: p. 378-391.

144. Garden, G.A. and T. Möller, *Microglia biology in health and disease.* Journal of NeuroImmune Pharmocology, 2006. **1**: p. 127-137.
145. Sitterley, G. *Poly-lysine*. BioFiles 2008 [cited 2013 November 28]; Available from: http://www.sigmaaldrich.com/technical-documents/articles/biofiles/poly-lysine.html.
146. Sigma-Aldrich. *Product Information: 3-(Trimethoxysily)propyl methacrylate*. 2013 [cited 2013 November 28]; Available from: http://www.sigmaaldrich.com/etc/medialib/docs/Sigma/Product_Information_Sheet/1/m6514pis.Par.0001.File.tmp/m6514pis.pdf.
147. Sigma-Aldrich. *Product Information: 3-Aminopropyltriethoxysilane*. 2013 [cited 2013 November 28]; Available from: http://www.sigmaaldrich.com/content/dam/sigma-aldrich/docs/Sigma-Aldrich/Product_Information_Sheet/a3648pis.pdf.
148. Sato, T. and V.N. Murthy, *Light-emitting diodes for biological microscopy.* Cold Spring Harbor Protocols, 2012: p. 1211-1222.
149. Ghorpade, R.V., et al., *Photopolymerization kinetics of 2-phenylethyl (meth) acrylates studied by photo DSC.* Journal of Polymer Research, 2012. **19**.
150. He, H., L. Li, and L.J. Lee, *Photopolymerization and structure formation of methacrylic acid based hydrogels: The effect of light intensity.* Reactive and Functional Polymers, 2008. **68**: p. 103-113.
151. Whittemore, S.R., H.R. Sanon, and P.M. Wood, *Concurrent isolation and characterization of oligodendrocytes, microglia and astrocytes from adult human spinal cord.* International Journal of Developmental Neuroscience, 1993. **11**(6): p. 755-764.
152. Nikodemova, M. and J. Watters, *Efficient isolation of live microglia with preserved phenotypes from adult mouse brain.* Journal of Neuroinflammation, 2012. **9**(147).
153. Sigma-Aldrich. *Product Information: Percoll*. 2013 [cited 2013 November 28]; Available from: http://www.sigmaaldrich.com/content/dam/sigma-aldrich/docs/Sigma/Product_Information_Sheet/1/p1644pis.pdf.
154. Phillips, M.J. and D.C. Otteson, *Differential Expression of Neuronal Genes in Müller Glia in Two- and Three-Dimensional Cultures.* Retinal Cell Biology, 2011. **52**(3).
155. Macaya, D. and M. Spector, *Injectable hydrogel materials for spinal cord regeneration: a review.* Biomedical Materials, 2012. **7**.

APPENDIX A

A.1 CNC Milling Design File and Code

The design file used to create the acrylic holding mold described in section 2.4.1 is presented below.

Mastercam X *Setup Sheet Report*

GENERIC HAAS 3X MILL MM

GENERAL INFORMATION

PROJECT NAME:	Cell Culture Mold (Andrea)	
CUSTOMER NAME:	SMART Team	
PROGRAMMER:	Kian	
DRAWING:	Single Step Build	REVISION: 2013-03-11
DATE:	March-11-13	
TIME:	5:58 PM	

C:\USERS\KIAN\DOCUMENTS\KIAN\MILLING\3D MODELS\ANDREA MOLD - 2013-03-11.MCX-6

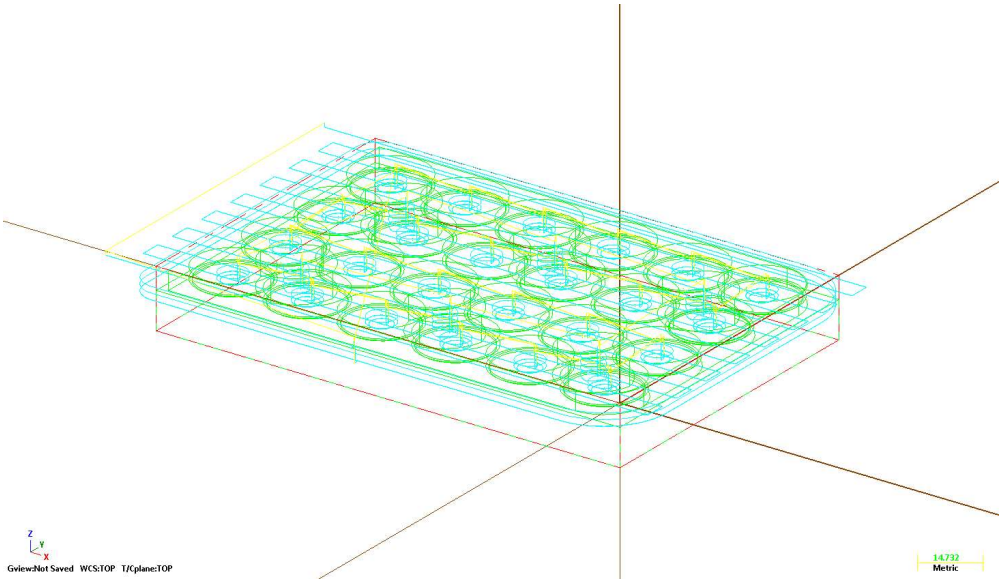

COMMENTS

STOCK / SAFEZONE INFO

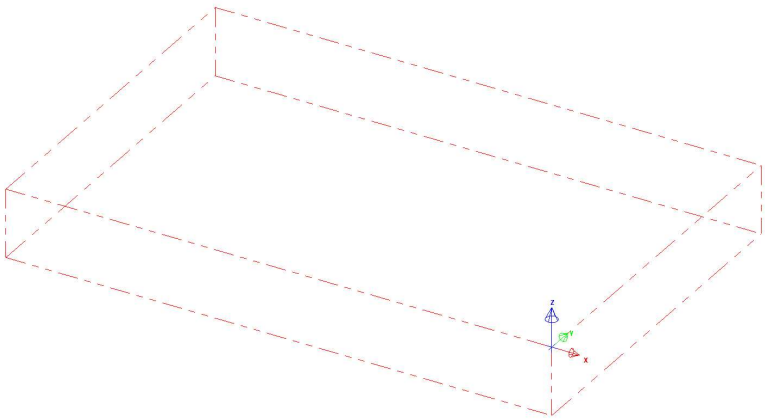

STOCK:	YES	**SAFEZONE:**	NO
SHAPE:	Box	SHAPE:	NA
SIZE:	128.0, 85.0, 16.0	SIZE:	NA
RADIUS:	NA	RADIUS:	NA
LENGTH:	NA	LENGTH:	NA
AXIS:	NA	AXIS:	NA
FILE:	NA		
IDN:	NA		

C:\USERS\KIAN\DOCUMENTS\MY MCAMX6\MILL\NC\ANDREA

CYCLE TIME:	10 HOURS, 40 MINUTES, 39 SECONDS

OPERATION LIST

OPERATION INFO ***Facing***

CYCLE TIME:	3 HOURS, 59 MINUTES, 23 SECONDS
COMMENT:	_

PROGRAM NUMBER:	0
SPINDLE SPEED:	25000 RPM
FEEDRATE:	20.0 inch/min
CLEARANCE PLANE:	50.0
RETRACT PLANE:	25.0
FEED PLANE:	0.1
DEPTH:	-1.0
STOCK TO LEAVE:	0.0
COMP TO TIP:	YES
WORK OFFSET:	0

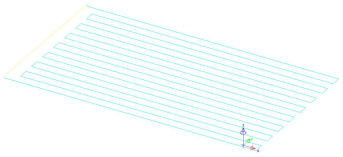

TOOL INFO ***#1 - M12.70 ENDMILL1 FLAT - 1/2 ENDMILL PLASTIC 2FL***

TYPE:	Endmill1 Flat
NUMBER:	1
DIAMETER:	12.7
CORNER RADIUS:	0.0
LENGTH OFFSET:	1
DIAMETER OFFSET:	1
MATERIAL:	Carbide
NUMBER OF FLUTES:	2
FPT:	0.0
SFM:	997.487
MFG CODE:	_
HOLDER:	
TIME:	03:59:23

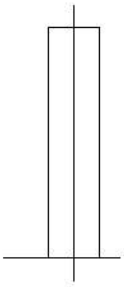

OPERATION INFO ***Contour (2D)***

CYCLE TIME:	1 HOURS, 29 MINUTES, 27 SECONDS
COMMENT:	_

PROGRAM NUMBER:	0
SPINDLE SPEED:	25000 RPM
FEEDRATE:	20.0 inch/min
CLEARANCE PLANE:	50.0
RETRACT PLANE:	0.0
FEED PLANE:	0.0
DEPTH:	-6.0
STOCK TO LEAVE:	0.0
COMP TO TIP:	YES
WORK OFFSET:	0

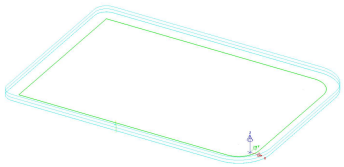

TOOL INFO ***#1 - M12.70 ENDMILL1 FLAT - 1/2 ENDMILL PLASTIC 2FL***

TYPE:	Endmill1 Flat
NUMBER:	1
DIAMETER:	12.7
CORNER RADIUS:	0.0
LENGTH OFFSET:	1
DIAMETER OFFSET:	1
MATERIAL:	Carbide
NUMBER OF FLUTES:	2
FPT:	0.0
SFM:	997.487
MFG CODE:	_
HOLDER:	
TIME:	01:29:27

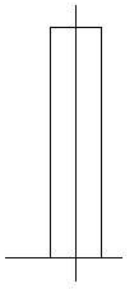

OPERATION INFO ***Pocket (Standard)***

CYCLE TIME:	2 HOURS, 28 MINUTES, 55 SECONDS
COMMENT:	_

PROGRAM NUMBER:	0
SPINDLE SPEED:	25000 RPM
FEEDRATE:	20.0 inch/min
CLEARANCE PLANE:	50.0
RETRACT PLANE:	0.0
FEED PLANE:	0.0
DEPTH:	-4.0
STOCK TO LEAVE:	0.0
COMP TO TIP:	YES
WORK OFFSET:	0

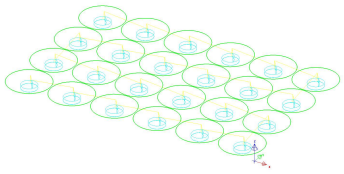

TOOL INFO ***#1 - M12.70 ENDMILL1 FLAT - 1/2 ENDMILL PLASTIC 2FL***

TYPE:	Endmill1 Flat
NUMBER:	1
DIAMETER:	12.7
CORNER RADIUS:	0.0
LENGTH OFFSET:	1
DIAMETER OFFSET:	1
MATERIAL:	Carbide
NUMBER OF FLUTES:	2
FPT:	0.0
SFM:	997.487
MFG CODE:	_
HOLDER:	
TIME:	02:28:55

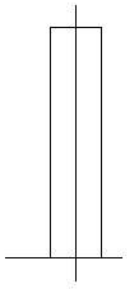

OPERATION INFO ***Pocket (Standard)***

CYCLE TIME:	1 HOURS, 34 MINUTES, 47 SECONDS
COMMENT:	_

PROGRAM NUMBER:	0
SPINDLE SPEED:	25000 RPM
FEEDRATE:	20.0 inch/min
CLEARANCE PLANE:	50.0
RETRACT PLANE:	0.0
FEED PLANE:	0.0
DEPTH:	-4.5
STOCK TO LEAVE:	0.0
COMP TO TIP:	YES
WORK OFFSET:	0

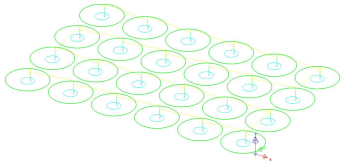

TOOL INFO ***#1 - M12.70 ENDMILL1 FLAT - 1/2 ENDMILL PLASTIC 2FL***

TYPE:	Endmill1 Flat
NUMBER:	1
DIAMETER:	12.7
CORNER RADIUS:	0.0
LENGTH OFFSET:	1
DIAMETER OFFSET:	1
MATERIAL:	Carbide
NUMBER OF FLUTES:	2
FPT:	0.0
SFM:	997.487
MFG CODE:	_
HOLDER:	
TIME:	01:34:47

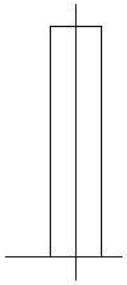

OPERATION INFO ***Pocket (Standard)***

CYCLE TIME:	1 HOURS, 8 MINUTES, 5 SECONDS
COMMENT:	_

PROGRAM NUMBER:	0
SPINDLE SPEED:	25000 RPM
FEEDRATE:	20.0 inch/min
CLEARANCE PLANE:	50.0
RETRACT PLANE:	0.0
FEED PLANE:	0.0
DEPTH:	-7.5
STOCK TO LEAVE:	0.0
COMP TO TIP:	YES
WORK OFFSET:	0

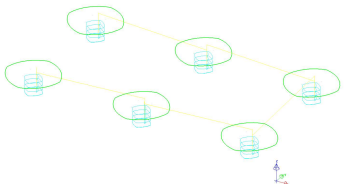

TOOL INFO ***#1 - M12.70 ENDMILL1 FLAT - 1/2 ENDMILL PLASTIC 2FL***

TYPE:	Endmill1 Flat
NUMBER:	1
DIAMETER:	12.7
CORNER RADIUS:	0.0
LENGTH OFFSET:	1
DIAMETER OFFSET:	1
MATERIAL:	Carbide
NUMBER OF FLUTES:	2
FPT:	0.0
SFM:	997.487
MFG CODE:	_
HOLDER:	
TIME:	01:08:05

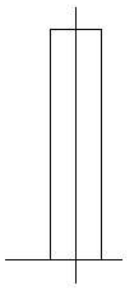

TOOL LIST Sorted: NO

TOOL INFO ***#1 - M12.70 ENDMILL1 FLAT - 1/2 ENDMILL PLASTIC 2FL***

TYPE:	Endmill1 Flat
NUMBER:	1
DIAMETER:	12.7
CORNER RADIUS:	0.0
LENGTH OFFSET:	1
DIAMETER OFFSET:	1
MATERIAL:	Carbide
NUMBER OF FLUTES:	2
FPT:	0.0
SFM:	997.487
MFG CODE:	_
HOLDER:	
TIME:	10:40:39

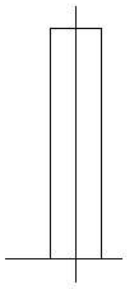

USED BY OPERATION:	# 1	Facing
USED BY OPERATION:	# 2	Contour (2D)
USED BY OPERATION:	# 3	Pocket (Standard)
USED BY OPERATION:	# 4	Pocket (Standard)
USED BY OPERATION:	# 5	Pocket (Standard)

WORK OFFSETS

OFFSET INFO

NUMBER:	0	VNUM:	1	ORIGIN: 0.0, 0.0, 0.0

USED BY OPERATION:	# 1	Facing
USED BY OPERATION:	# 2	Contour (2D)
USED BY OPERATION:	# 3	Pocket (Standard)
USED BY OPERATION:	# 4	Pocket (Standard)
USED BY OPERATION:	# 5	Pocket (Standard)

A.2 Buffer Solutions

The recipes used to produce buffer solution made in house are described below.

A.2.1Phosphate Buffer Saline (PBS)

PBS is a buffer solution designed to create an isotonic solution matching the osmolarity and ion concentrations of the human body. It was prepared in ddH_2O with 13.69 M NaCl, 0.27 M KCl, 0.10 M Na_2HPO_4 and 0.018 M KH_2PO_4 (dibasic). The pH of this solution was then adjusted to 7.4.

A.2.2 Brain Buffer Solution (BBS)

BBS is a buffer solution intended to maintain the osmolarity and ion concentrations of the CNS. It was prepared in ddH2O with 134.90 mM NaCl, 5.40 mM KCl, 16.64 mM CaCl2 and 5.00 mM HEPES-Na. The pH was then adjusted to 7.4 and the solution was filtered through a 0.02 micron vacuum filter.